A Detailed Study of the Supernova Remnant RCW 86 in TeV γ-Rays

Detaillierte Analyse
der TeV-Gammastrahlung
des Supernovaüberrests
RCW 86

Der Naturwissenschaftlichen Fakultät
der Friedrich-Alexander-Universität Erlangen-Nürnberg
zur Erlangung des Doktorgrades Dr. rer. nat.

vorgelegt von
Sebastian Heinz
aus Nürnberg

Als Dissertation genehmigt von der Naturwissenschaftlichen Fakultät
der Friedrich-Alexander-Universität Erlangen-Nürnberg

Tag der mündlichen Prüfung: 29.3.2012

Vorsitzender der Promotionkommission:	Prof. Dr. Rainer Fink
Erstberichterstatter:	Prof. Dr. Christian Stegmann
Zweitberichterstatterin:	Prof. Dr. Gisela Anton

Kurzfassung

In dieser Dissertation wird eine detaillierte Studie des Supernovaüberrestes RCW 86 präsentiert. RCW 86 weist eine Schalenstruktur im Radio-, Röntgen- und im optischen Wellenlängenbreich auf. In der Gammastrahlungsastronomie allerdings konnte dies noch nicht bewiesen werden. In dieser Dissertation wurde zum ersten Mal die Schalenstruktur in der Gammastrahlungastronomie aufgelöst. Die Breite der Schale wurde zu $0.125° \pm 0.014°$, der Radius zu $0.194° \pm 0.016°$ und das Zentrum zu $-62.433° \pm 0.014°$ in Deklination und $220.734° \pm 0.016°$ in Rektaszension bestimmt. Die spektrale Analyse wurde für den süd-östlichen Teil und auch die Gesamtheit des Supernovaüberrests durchgeführt. Innerhalb der Fehler waren beide Ergebnisse konsistent. Es stellte sich heraus, dass das Potenzgesetz mit exponentieller Abschwächung die Daten am Besten beschreibt. Die Parameter sind hierbei: ein spektraler Index von 1.50 ± 0.28, eine Abknickenergie von $(2.69 \pm 0.99$ TeV) und ein integraler Fluss oberhalb von 1 TeV von $(6.51 \pm 2.69) \cdot 10^{-12}$ cm^{-2} s^{-1}.

Die Korrelationsuntersuchungen zwischen Röntgen- und Gammastrahlung von RCW 86 wurde durch die schlechte Winkelauflösung der Gammastrahlungsdaten behindert. Aus diesem Grund wurde eine detaillierte Studie des Richardson-Lucy Algorithmus durchgeführt. Das Ergebnis zeigte, dass die Entfaltung auf starke Gammastrahlungsquellen angewendet werden kann und deutlich kleinere Strukturdetails als durch die Auflösung der Gammastrahlung möglich untersucht werden können. Die Anwendung der Entfaltung auf den stärksten Supernovaüberest RX J1713-3946 im Gammastrahlungsbereich zeigte, das die Korrelation zwischen Röntgen- und Gammastrahlung bis zu Strukturgrössen von 0.01° stabil ist. Auf der anderen Zeite zeigte sich, dass die Signifikanz im Fall der Datenlage von RCW 86 nicht ausreichend ist um die Methodik der Entfaltung hier anwenden zu können.

Abstract

A detailed study of the supernova remnant RCW 86 is presented. RCW 86 encountered a shell-like structure in radio, X-rays and optical, whereas in the discovery paper of RCW 86 in the very high energy regime the structure could not be confirmed. In this thesis for the first time the shell was resolved in the very high energy gamma rays. The shell width was determined to be $0.125° \pm 0.014°$, the radius to be $0.194° \pm 0.016°$ and the center to be $-62.433° \pm 0.014°$ in declination and $220.734° \pm 0.016°$ in rectascension. The spectral analysis was performed for the whole SNR and for the south-east part, which is more pronounced in X-rays separately. But the results were comparable within errors. Additionally a power-law with an exponential cut off described the spectra best with the parameters: an spectral index of 1.50 ± 0.28, a cut-off energy of $(2.69 \pm 0.99$ TeV) and an integral flux above 1 TeV of $(6.51 \pm 2.69) \cdot 10^{-12}$ cm^{-2} s^{-1}.

The study of the correlation of the X-ray and VHE γ-ray data of RCW 86 was hampered by the poor angular resolution of the VHE data. Therefore detailed studies of the Richardson-Lucy deconvolution algorithm have been performed. The outcome is, that deconvolution techniques are applicable to strong VHE γ-ray sources and that fine structure well below the angular resolution can be studied. The application to RX J1713-3946, the brightest SNR in the VHE regime, has shown, that the correlation coefficient of the X-ray data and the VHE data of is stable down to 0.01° and has a value of 0.85 . On the other side the significance of the data set is not sufficient in the case of RCW 86 to apply the deconvolution technique.

Contents

1 Introduction

The balloon experiments conducted by the Austrian physicist Victor Hess during the years 1911 – 1913 can be regarded to mark the founding of a new field of physics: cosmic-ray astrophysics. At the time the common consensus was that the radioactivity of ground material is responsible for the ionization effects seen in physics experiments. To test this hypothesis V. Hess started his balloon experiments to check the predicted fading of this effect in the higher atmosphere (Hess 1912). Up to an altitude of 1 km he indeed measured a decay of the effect but then the ionization strongly increased again and was even higher than on his starting point (see Fig. 1.1(b)). His conclusion was that

a radiation of very high penetrating power enters our atmosphere from above.

In appreciation of his discovery, he was awarded the Nobel prize in physics in 1936.

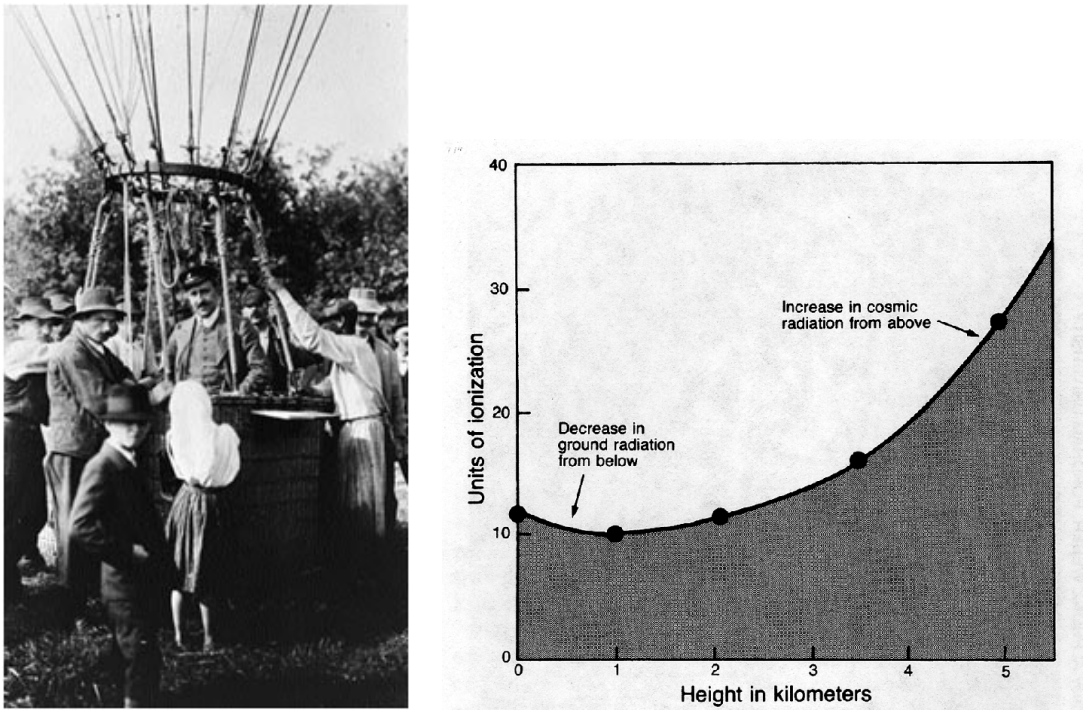

(a) (b)

Figure 1.1: First indication for cosmic rays seen by Victor Hess:
(a) Victor Hess after one of his successful flights (Figure from Fermilab (2011))
(b) Plot of the measured data taken by Victor Hess (Figure from Kraus (2011))

During the years of 1930 – 1950, before the era of man-made particle accelerators, the cosmic rays were used as a source of high energy particles. In the performed experiments subatomic particles like the positron e^+ and the muon μ were discovered. In the 1960s our knowledge of cosmic rays was extended by the use of satellite experiments. Their main achievements were the first studies of the composition and the spectrum of the cosmic rays. Starting in the 1990s our knowledge was

mainly enlarged regarding energy range and accuracy by a new detection technique, the so-called air shower measurements. Ground-based detector arrays measure the energy and the chemical composition of the cosmic rays. The air shower technique is explained in Sec. 3.1.
After this short historical overview our current knowledge of cosmic rays is presented in the condensed form by the use of the differential energy spectrum of all particles (see Fig. 1.2): The cosmic rays are subatomic particles from outer space and the composition consists of 99% nuclei (89% protons (hydrogen nuclei), 10% α particles (helium nuclei) and 1% nuclei of more massive elements) and the remaining 1% mainly of electrons. To better visualize the different parts or features of the cosmic-ray spectrum it was multiplied by $E^{2.7}$ (see Fig. 1.2).

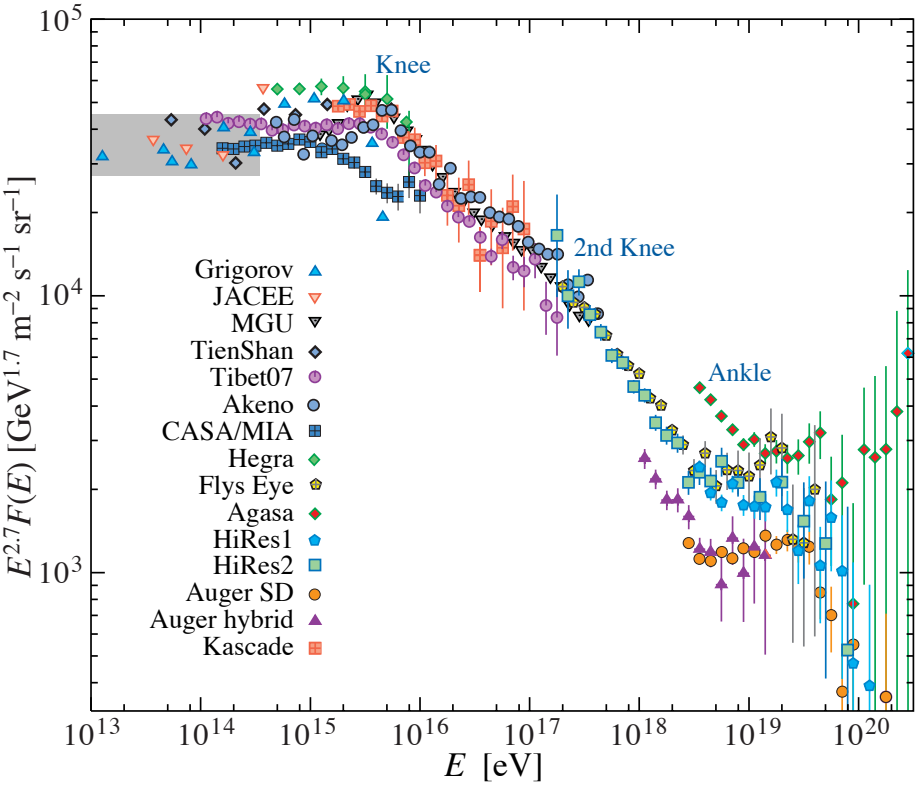

Figure 1.2: The all-particle spectrum of cosmic rays obtained from air shower measurements. The shaded area shows the energy range in which cosmic rays are directly detectable, e.g. by balloon experiments. Credit: Nakamura (2010)

The shaded area indicates the energy range in which cosmic rays are directly detectable, e.g. by balloon experiments. Since above this energy range the flux of cosmic rays is too low, they are measured indirectly by air shower experiments. The different parts of the cosmic-ray spectrum can be classified by means of the two knees and the ankle (Nakamura 2010): Galactic sources (accelerators) are believed to accelerate cosmic rays up to energies of 10^{18} eV. Furthermore different source types have different maximum energies which explain the knees. Moreover a limit of the acceleration is the propagation and confinement in the Galaxy (Ptuskin et al. 1993).
Above energies of about 10^{18} eV cosmic rays are thought to have their origin in Extragalactic sources and the separation between Galactic and Extragalactic sources is supposed to result in the ankle.

If this hypothesis is correct there should be a dip after the ankle around an energy of 10^{19} eV because of the energy loss of Extragalactic protons ($\gamma p \rightarrow p + \pi^0$ or $\gamma p \rightarrow n + \pi^+$) on the 2.7 K

cosmic microwave background (CMB). This feature is also called Greisen–Zatsepin–Kuzmin (GZK) cut-off (Greisen 1966), (Zatsepin & Kuz'min 1966). For the time being the collected data do not yield compelling evidence for the GZK cut-off and the clarification is one issue of current research. The data of the AGASA experiment are compatible with a continued power law flux which is in contrast to the support of the GZK cut-off by the HiRes and Auger experiments.

The prime candidate for the sources of the Galactic cosmic-rays are supernova remnants (SNR). For the acceleration mechanism of particles up to energies of 10^{15} eV the diffuse shock acceleration is suggested (see Section 2.2). If SNRs are the sources of cosmic rays the dominant particle population has to be hadronic to be able to explain the measured cosmic-ray composition since the acceleration of leptons plays only a minor role. Up to now the question whether SNRs accelerate mainly leptons or hadrons is not finally settled. The accelerated particles can then interact with the surrounding medium and generate highly energetic photons which may travel towards Earth without any deflection by the interstellar magnetic field in contrast to electrically charged particles. Therefore the photons detected on earth point back to the source. This is the basic idea behind the observations in very high energy (VHE) γ-ray astronomy. A brief overview of the development of VHE γ-ray astronomy is given at the end of Sec. 3.2.

One of the experiments which observe VHE γ-rays in the energy range between 100 GeV and 100 TeV is the H.E.S.S. experiment[1], located on the southern hemisphere in Namibia. It is introduced in Sec. 3.3 and belongs to the group of VHE γ-ray experiments using the imaging atmospheric Cherenkov technique (IACT) (see Sec. 3.2). Besides H.E.S.S., another VHE γ-ray experiment CANGAROO III[2] (Australia) also on the southern hemisphere and MAGIC[3] (La Palma, Spain) and VERITAS[4] (Arizona, U.S.) on the northern hemisphere are operating.
In the last years more than 120 VHE γ-ray sources have been detected, which is a quite impressive increase. In Fig. 1.3 the big impact of the H.E.S.S. experiment in this field is clearly visible.

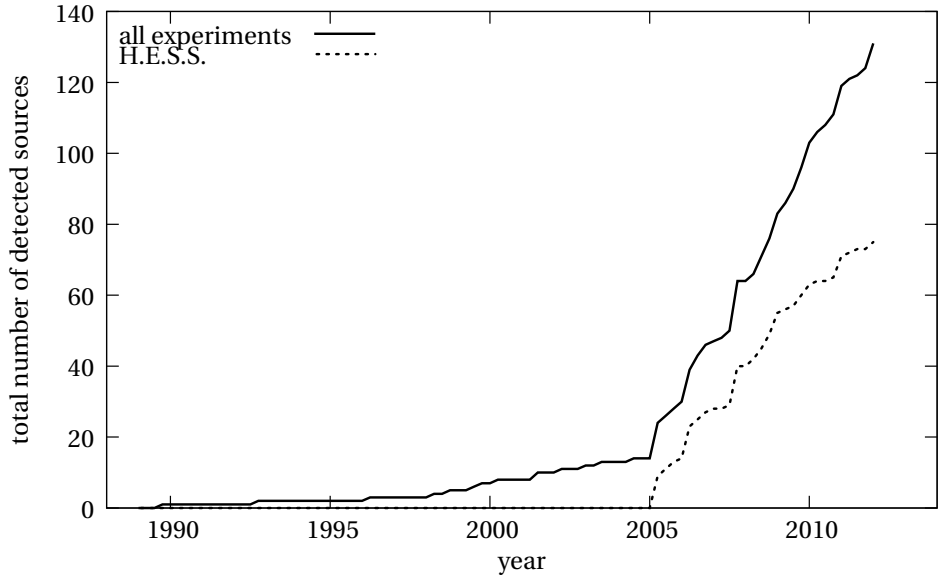

Figure 1.3: Time line of the discovery of VHE γ-ray sources. The solid line indicates the development for all experiments (CANGAROO, HEGRA, H.E.S.S., MAGIC, Milagro, VERITAS, Whipple) and the dashed line for the H.E.S.S. experiment. (data according to TeVCat (Nov. 2011)

[1] http://www.mpi-hd.mpg.de/hfm/HESS/
[2] http://www.physics.adelaide.edu.au/astrophysics/cangaroo/
[3] http://magic.mppmu.mpg.de/
[4] http://veritas.sao.arizona.edu/

The view of the sky in VHE γ-rays reveals, that the Galactic VHE γ-ray sources are lined up like pearls on a string along the Galactic plane, which can be nicely seen in Fig. 1.4.

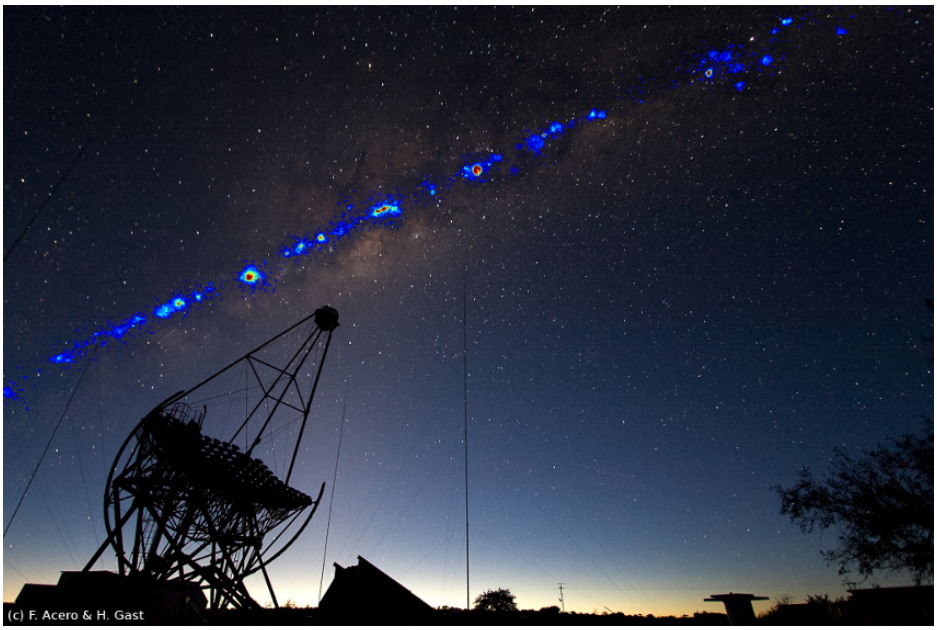

Figure 1.4: Montage of an image of the southern night sky with a current map of the H.E.S.S. Galactic Plane Survey. One of the H.E.S.S. telescopes is seen in the foreground. Credit: F. Acero & H. Gast 2011.

Nearly all Galactic VHE γ-ray sources are extended and a detailed study of their morphology would be preferable. A drawback is the poor angular resolution of IACT experiments in comparison to the X-ray experiments which makes the study of the morphology rather difficult. In the context of this thesis, the deconvolution technique to improve the angular resolution is studied in detail and applied to VHE γ-ray data.

The focus of this dissertation is a detailed study of the SNR RCW 86. At first the general characteristics of SNRs and the particular details of the SNR RCW 86 are presented in Chapter 2. The large size of RCW 86 and the observation of non-thermal X-ray, which is a trace for the acceleration of particles to the VHE, made it a promising target for VHE γ-ray observations. Furthermore RCW 86 is still a very good candidate for a supernova remnant where the shell-like structure can be resolved in VHE γ-rays even though it was not possible to clarify this in the first H.E.S.S. publication (Aharonian et al. 2009). The next Chapter 3 is focused on the Imaging Atmospheric Cherenkov Technique, the H.E.S.S. Experiment in particular and the analysis methods used by the H.E.S.S. collaboration. In Chapter 4 the analysis results of the enlarged H.E.S.S. data set of RCW 86 is presented. The focus of the analysis is based on the question whether RCW 86 belongs to the group of shell-type supernova remnants or not. The advantage of this group is that the acceleration of VHE γ-rays can be studied spatially resolved and compared to detailed theories. Subsequently the deconvolution technique is explained which is newly introduced into the VHE γ-ray astronomy to improve the angular resolution of the observations (see Chapter 5). The goal of applying deconvolution techniques is to be able to perform detailed morphology studies of extended VHE γ-ray sources and finally to clarify with correlation studies between different wavebands whether VHE γ-ray sources are really cosmic-ray accelerators or not. Finally a brief summary in Chapter 6 concludes this dissertation.

2 Supernova Remnants and the Case of RCW 86

In this chapter the focus is on supernova remnants (SNR) as Galactic VHE γ-ray accelerators in general and on the case of the SNR RCW 86 in particular. As a start the evolution and the morphology of SNRs are presented. In a next step the acceleration mechanism for cosmic rays and the generation of VHE γ-ray in SNRs are explained. The production of VHE γ-ray radiation can be divided into two radiation scenarios: γ-ray radiation from hadronic- or leptonic particles. In the following the H.E.S.S. detections of SNRs are listed to show the current status of the observations and the analyses of SNRs by H.E.S.S.. At the end of this chapter the observations of RCW 86 at different wavebands (radio, optical, X-rays, VHE) are presented to collect the currently available knowledge on this particular VHE γ-ray source.

2.1 Evolution and Morphology

The current understanding of the evolution of SNRs is the following. After a supernova explosion gas is ejected with high velocity into the cold interstellar medium (ISM) which has a particle density of about $\rho \approx 1\,\mathrm{cm}^{-3}$. Interacting with the ISM the gas is slowed down and the formation of a shell will start. In the beginning the shell is hot and dominated by pressure forces, but in the further evolution of the SNR the influence of radiative cooling becomes more and more dominant. The final state of the evolution will be reached when the velocity of the shell is in the order of the velocity of the surrounding ISM and the shell disappears into the ISM.

In a rather simple model the mass of the gas M_0 with a velocity V_0 and a total energy (thermal and kinetic) E_0 is injected into a rather cold medium with the density ρ at the time $t = 0$. The thin border between the expanding matter and the surrounding matter defines the outer border of the shell, with a radius R. The radiative energy loss per time is defined as $\left(\frac{\mathrm{d}E}{\mathrm{d}t}\right)_{\mathrm{rad}}$ with the energy E. The effects of relativistic particles and magnetic fields are not taken into account. However even with such a simple model it is possible to identify four different stages of the evolution of a SNR.

Phase I (Free Expansion Phase):

In phase I, also called the free expansion phase, a shock front is formed by the interaction of the gas with the ISM. The gas moves with a constant velocity until the swept-up mass from the ISM $M_{\mathrm{swept-up}}$ is equal to M_0:

$$M_{\mathrm{swept-up}} = \left(\frac{4\pi}{3}\right)\rho R^3 \stackrel{!}{=} M_0 \tag{2.1}$$

with the density ρ of the rather cold surrounding medium. In this phase the radius R of the SNR is directly proportional to the age of the remnant:

$$R \propto t. \tag{2.2}$$

The end of this phase is reached at an age of $t \approx 200$ yrs, when the condition in Eq. 2.1 is fulfilled and the temperature of the gas is $\approx 10^8$ K and the velocity $\approx 10^4$ km s^{-1}.

Phase II (Sedov Phase):

During the phase II, the so-called Sedov phase, the swept-up matter $M_{\mathrm{swept-up}}$ dominates the evolution of the SNR:

$$M_{\mathrm{swept-up}} = \left(\frac{4\pi}{3}\right) \rho_0 R^3 \gg M_0. \tag{2.3}$$

Additionally the radiation losses $\left(\frac{\mathrm{d}E}{\mathrm{d}t}\right)_{\mathrm{rad}}$ are negligible compared to the SN explosion energy E_0 and the total energy stays nearly constant:

$$\int \left(\frac{\mathrm{d}E}{\mathrm{d}t}\right)_{\mathrm{rad}} \mathrm{d}t \ll E_0. \tag{2.4}$$

Following Sedov (1959) the radius R of the shell of the SNR for a gas with the ratio of specific heats $\gamma = \frac{5}{3}$ depends on the time as follows:

$$R = 1.17 \left(\frac{{E_0}^{\frac{1}{5}}}{\rho}\right) t^{\frac{2}{5}}, \tag{2.5}$$

Therefore the velocity is obtained to be

$$V = \frac{2}{5}\frac{R}{t}. \tag{2.6}$$

With the combination of Eq. 2.5 and Eq. 2.6 one gets the following adiabatic equation:

$$R^3 V^2 = \text{constant}. \tag{2.7}$$

Hence, this phase is also called the adiabatic phase. The end of phase II can be defined as the time t_{rad} at which the energy drops to half of its initial value due to radiative energy losses:

$$t_{\mathrm{rad}} = 1.1 E_0^{\frac{4}{17}} \rho^{-\frac{9}{17}}. \tag{2.8}$$

This age is reached after $10^2 - 10^6$ yrs and at this point the temperature of the gas is $T \approx 10^6$ K and the velocity is $V \approx 200$ km s^{-1}.

Phase III (Snowplough Phase):

In phase III, also called Snowplough phase, the evolution time t is significantly higher than the radiation cooling time t_{rad}, the matter behind the shock cools quickly and the shell radiates energy more efficiently. The size of the shell shrinks and the material in the shell becomes denser and

so the shell cools even faster. The pressure forces are not important any more and the shell has a constant radial momentum:

$$\left(\frac{4\pi}{3}\right) R^3 \rho_0 V = \text{constant}. \tag{2.9}$$

This leads to a dependency of the radius R on the age t of

$$R \propto t^{\frac{1}{4}}. \tag{2.10}$$

The typical values at the end of this phase are: an age of $\approx 3 \times 10^5$ yrs, a temperature of the gas of $T \approx 10^4$ K and a velocity of $V \approx 10$ km s^{-1}.

Phase IV (Dispersal Phase):

During the phase IV, the so-called dispersal phase, the shell velocity is of the order of the velocity of the surrounding ISM ($V \approx 10\,\text{kms}^{-1}$) and the shell dissipates into the ISM.

In Fig. 2.1 the radius (outer border) R of the shell of a SNR is plotted against the age t. The four different phases are shown in the plot and the temperature T and velocity V of the respective phases are also included.

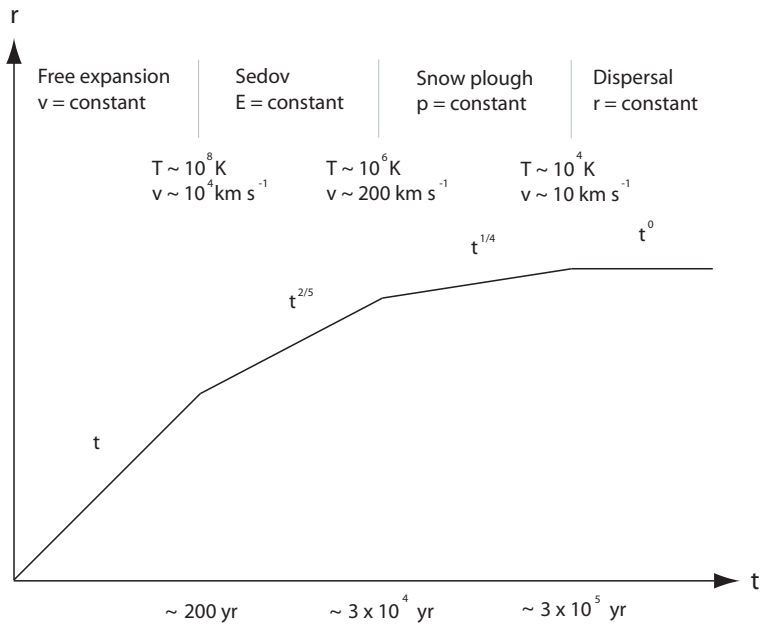

Figure 2.1: The radius r of the supernova shell as a function of the age t of the SNR. The four different phases of the SNR evolution are marked. (Figure adapted from Padmanabhan (2001)).

Morphology

SNRs are divided into three different types of morphologies (Bhattacharya 1990). This classification is not strict since it is possible that a SNR changes its type from one to another during their evolution (Sakhibov & Smirnov 1982), (Lazendic et al. 2000).
The three types of morphologies are:

- Shell-type remnants:
  The evolution presented above leads to a shell-like structure when the shock wave interacts with the ISM. The majority of SNRs are of this type and have a ring-like morphology with a certain thickness in their observations.
- Crab-like remnants:
  Another type are "plerions" which are similar to the Crab Nebula. In addition to the shock wave they contain a pulsar in the middle which blows out fast moving material through jets. These centrally-filled SNRs look more like a *sphere* than a *ring* in their observations.
- Composite Remnants:
  The SNR changes appearances when observed at different wavebands. It is possible that it looks shell-like or crab-like or has both features (hybrid) at a certain wavebands. Thermal composite SNRs have a shell-like structure in radio and a crab-like structure in X-ray with indications for hot gas. Plerionic composites appear crab-like in both energy ranges but the shell is also visible.

The information in this section is mainly based on Woltjer (1972) and Padmanabhan (2001).

2.2 Diffusive Shock Acceleration

SNRs are the prime candidates as sources of the galactic cosmic rays, i. e. an acceleration mechanism that can accelerate particles up to energies of $\sim 10^{15}$ eV has to exist. The following section introduces the historical view and the mechanism commonly regarded as the most promising concept, the so-called *first-order Fermi acceleration*.

For historical reasons the so-called *second-order Fermi acceleration*[1] introduced by Fermi (1949) is discussed first. This mechanism was the first try to explain the acceleration of cosmic ray particles. If a particle with energy E, velocity v and momentum p collides with dense clouds in the interstellar medium which move with the velocity $V \ll c$, the clouds will behave like “magnetic mirrors” for the particle. The angle between the direction of the particle and the “surface” of the mirror is θ. In the center of momentum frame (CMF) the particle has the following energy E':

$$E' = \gamma_{\mathrm{L}} \left(E + V p \cos\theta \right), \tag{2.11}$$

and a x-component of the momentum p'_x:

$$p'_x = p' \cos\theta' = \gamma_{\mathrm{L}} \left(p \cos\theta + \frac{VE}{c^2} \right) \tag{2.12}$$

before the collision. In this section γ_{L} is the Lorentz factor: $\gamma_{\mathrm{L}} = \left(1 - \frac{V^2}{c^2}\right)^{-\frac{1}{2}}$.

[1] This notation is usually used today for the acceleration which was introduced by Fermi.

The energy is conserved, $E'_{\text{before}} = E'_{\text{after}}$, and the momentum p'_x is reversed to $-p'_x$. Overall the energy E'' of the particle in the observer frame changes after the collision to:

$$E'' = \gamma_{\text{L}} \left(E' + V p'_x \right) \tag{2.13}$$

or, with $\frac{p_x}{E} = v \frac{\cos\theta}{c^2}$:

$$E'' = \gamma_{\text{L}}\, E \left[1 + \frac{2 V v \cos\theta}{c^2} + \left(\frac{V}{c} \right)^2 \right]. \tag{2.14}$$

After expanding equation 2.14 to the second order in $\frac{V}{c}$ and averaging over all angles in the range between 0 and π one gets an energy gain of:

$$\left\langle \frac{\Delta E}{E} \right\rangle = \frac{8}{3} \left(\frac{V}{c} \right)^2. \tag{2.15}$$

i.e. that the average increase in energy of a particle per collision is only of *second order* in $\frac{V}{c}$. It should be noted that this acceleration mechanism is too inefficient to explain the cosmic ray energies. The main problem is, that the velocity of interstellar clouds is rather small, namely in the range of $\frac{V}{c} \leq 10^{-4}$, and the mean free path is of the order of 0.1 pc. This would lead to only a few collisions per year and cannot explain the observed flux of cosmic rays.

The concept of the acceleration of particles can also be discussed in the context of a strong shock wave which is realized for example in a supernova shell. The following model of diffusive shock acceleration also called *first-order Fermi acceleration* is based on Bell (1978) and also presented in Longair (2011). A strong shock propagates through a diffusive medium with a gas of high-energy particles in front of and beyond the shock front and with particle velocities near the speed of light. The gas ahead is at rest and has a density ρ_1, pressure p_1 and temperature T_1 whereas the gas behind the shock front moves with a velocity v_2 and has a density ρ_2, pressure p_2 and temperature T_2. Additionally the particles are barely deflected by the shock front because its thickness is much smaller than their gyro radius. Finally turbulent motion of the particles on both sides of the shock wave are responsible for the fact that the particles have an isotropic velocity distribution in the frame of the moving gas on both sides of the shock.

A strong shock wave is characterized by a highly supersonic velocity $U \gg c_s$ (c_s is the sound speed of the ambient medium, see Fig. 2.2(a)). The mass is conserved in a strong shock wave and therefore the equation of continuity is valid:

$$\rho_1 v_1 = \rho_2 v_2 \tag{2.16}$$

with the density ρ_1 and the velocity v_1 of the upstream gas (or the interstellar gas) and the density ρ_2 and the velocity v_2 of the downstream gas. In the frame of reference in which the shock front is at rest the gas flows into the shock front with a upstream velocity $v_1 = U$ and leaves it with a downstream velocity v_2 (see Fig. 2.2(b)). For a strong shock the ratio of the down- and upstream densities can be derived as:

$$\frac{\rho_2}{\rho_1} = \frac{\gamma_{\text{s}} + 1}{\gamma_{\text{s}} - 1}. \tag{2.17}$$

In particular, for a fully ionized gas with a specific heat capacity $\gamma_s = \frac{5}{3}$ this leads to $\frac{\rho_2}{\rho_1} = 4$ and $v_2 = \frac{1}{4} v_1$ (see Fig. 2.2(b)).

Looking at the particle which are ahead of the shock, the velocity of the particles is isotropic due to scattering in the frame of reference in which the upstream gas is stationary (see Fig. 2.2(c)).

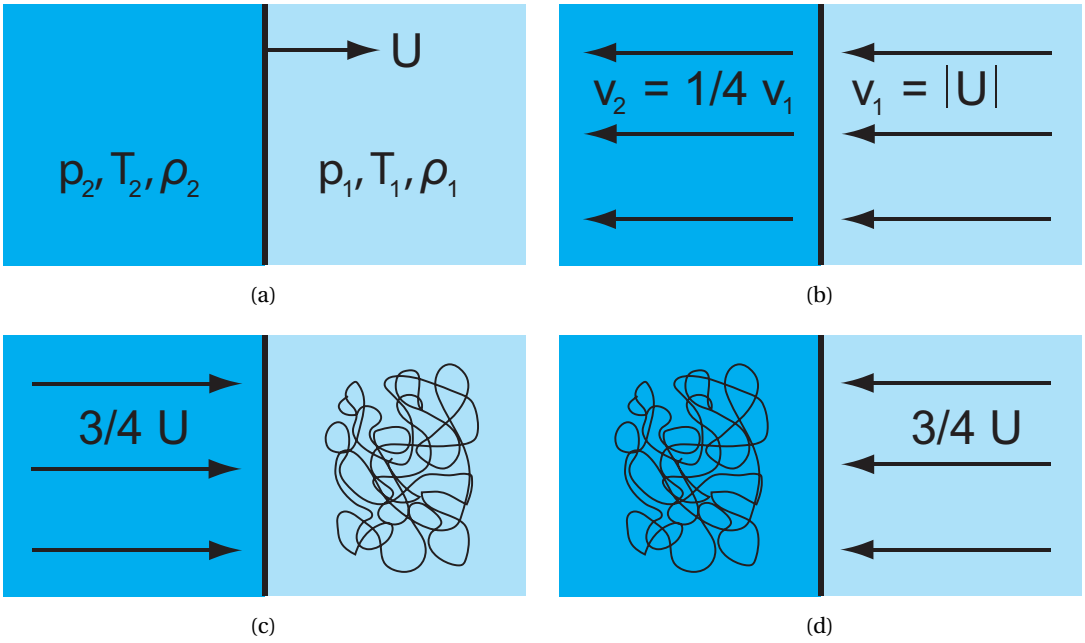

Figure 2.2: (a) Shock wave with a supersonic velocity U propagates through the interstellar gas with density ρ_1, pressure p_1 and temperature T_1. Behind the shock the parameters are ρ_2, p_2 and T_2. (b) The flow of interstellar gas in the rest frame of the shock front. (c) The flow of gas in the frame of reference with a stationary upstream gas. The velocity distribution of the particle is isotropic. (d) The flow of gas in the frame of reference with a stationary downstream gas. The velocity distribution of the particle is isotropic. (Figures adapted from Longair (2011)).

In this frame of reference the gas behind the shock has a velocity $V = \frac{3}{4} U$ relative to the upstream gas (see Fig. 2.2(c)). If a particle passes the shock front it will get an increase in energy and the velocity distribution becomes isotropic again due to scattering. In the rest frame of the downstream gas, a particle passing the shock front encounters exactly the same situation as the particle passing the shock front from the upstream to the downstream area (see Fig. 2.2(d)). Therefore it gets an additional energy increase of the same amount. The increase in energy in both directions is the main characteristic of the particle acceleration in strong shock waves.

In the following, the quantitative derivation of the energy increase is described. A particle increases its energy E' by passing from upstream to downstream:

$$E' = \gamma_L \left(E + p_x V \right). \tag{2.18}$$

The x-coordinate is parallel to the motion of the shock front. Since the shock is non-relativistic ($V \ll c$) and the particles are relativistic ($\gamma_L \approx 1$) with the energy $E = pc$ and the x-component of the momentum $p_x = \left(\frac{E}{c}\right) \cos\theta$, the increase of energy for the relativistic particle is

$$\Delta E = p V \cos\theta \tag{2.19}$$

or relative to its energy E:

$$\frac{\Delta E}{E} = \frac{V}{c}\cos\theta. \tag{2.20}$$

Therefore the gain of energy averaged over the angle θ in the range 0 to $\frac{\pi}{2}$ is:

$$\left\langle \frac{\Delta E}{E} \right\rangle = \frac{2}{3}\frac{V}{c}, \tag{2.21}$$

and for one round trip:

$$\left\langle \frac{\Delta E}{E} \right\rangle = \frac{4}{3}\frac{V}{c}. \tag{2.22}$$

In contrast to the *second order Fermi acceleration* the energy gain $\frac{\Delta E}{E}$ is of first order in $\frac{V}{c}$ and hence, the effect is often called *first-order Fermi acceleration*.
Taking the probability that a particle can escape the acceleration into account one obtains with some assumptions the following differential energy spectrum for this process:

$$N(E)\,\mathrm{d}E \approx E^{-2}\,\mathrm{d}E. \tag{2.23}$$

The derivation is explained in Longair (2011). The index of 2 differs somewhat from the 2.5 we expected from the observed cosmic-ray spectrum. Still, it provides a physical motivation for power-law spectra of astrophysical objects with strong shocks, e.g. supernova remnants. The measured indices can be explained by taking also the energy-dependent diffusion of the particles into account.

2.3 γ-radiation

In the previous section the acceleration mechanism of cosmic rays in SNRs was introduced. This section discusses the production of VHE γ-rays by high energetic protons or electrons. In all VHE γ-ray sources it is assumed, that leptons and hadrons are accelerated, i.e. the VHE γ-ray radiation is produced by both types. The still open question is the amount of leptons and hadrons and which is the dominant underlying process for the VHE γ-ray production.

2.3.1 γ-radiation from hadronic particles

In the interaction of protons or nuclei with the ISM mainly pions are created:

$$p + p \rightarrow \pi^0 + \pi^+ + \pi^- + X. \tag{2.24}$$

The cross-section σ_{pp} for the reaction 2.24 is nearly constant for proton in the energy range of $E_p = 0.1 - 100\,\mathrm{TeV}$:

$$\sigma_{pp} \approx 50\,\mathrm{mb}. \tag{2.25}$$

Because of the isospin symmetry all three types of pions are produced in about equal abundance. Subsequently the neutral pions decay nearly instantly into two photons:

$$\pi^0 \rightarrow \gamma\gamma. \tag{2.26}$$

At each interaction 50% of the proton energy is transferred to the pions and consequently only about $\frac{1}{6}$ to the neutral pions:

$$E_{\pi_0} \approx \frac{1}{6} E_p. \tag{2.27}$$

The simulations of Dermer (1986) and Mori (1997) have shown, that the mean energy transfer to one single photon produced through the π^0 decay is in the order of

$$\left\langle E_\gamma \right\rangle \approx \frac{1}{10} E_p. \tag{2.28}$$

Furthermore, the cooling time for the protons for the neutral pion decay is defined by their mean energy losses:

$$\left\langle \frac{\mathrm{d}E_p}{\mathrm{d}t} \right\rangle = \frac{E_p(t=0)}{\tau_{\pi^0}}. \tag{2.29}$$

Therefore the interaction time τ_{π^0} is the mean free path λ_{π^0} of the proton at which it loses this energy to the pions divided by its velocity c:

$$\tau_{\pi^0} = \frac{\lambda_{\pi^0}}{c} = \frac{1}{n_p \sigma_{pp} \frac{1}{6} c} \approx \frac{4 \cdot 10^{15}}{n_p \cdot \mathrm{cm}^3}\,\mathrm{s}. \tag{2.30}$$

For the ISM with a density of protons of $n_p = (10-100)\,\mathrm{m}^{-3}$ this results in

$$\tau_{\pi^0} \approx 4 \cdot 10^{19-20}\,\mathrm{s}, \qquad \lambda_{\pi^0} \approx 10^{11}\,\mathrm{pc}. \tag{2.31}$$

Under the assumption, that the proton energy distribution follows a power law, the spectral index of the photon spectrum stays the same and can be directly used to estimate the proton spectrum:

$$E_\gamma = (0.5-10)\,\mathrm{TeV} \Leftrightarrow E_p = (5-100)\,\mathrm{TeV}. \tag{2.32}$$

The information in this section is based on Hinton & Hofmann (2009) and Kowalski (2011).

2.3.2 γ-radiation from Electrons

Electrons and positrons can lose their energy through three different processes: bremsstrahlung in the interstellar material, synchrotron radiation in a magnetic field and inverse Compton scattering on interstellar photon fields. The three processes are presented in the following and the description is based on Blumenthal & Gould (1970), Kowalski (2011) and Longair (2011).

Bremsstrahlung

An electron scatters in the Coulomb field of a nucleus and radiates a photon. This process is called bremsstrahlung. The energy loss by bremsstrahlung can be characterized by the radiation length X_0, which is the mean distance after which an electron still has $\frac{1}{e}$ of its initial energy E_0:

$$\left\langle -\frac{1}{\rho}\frac{\mathrm{d}E}{\mathrm{d}x}\right\rangle_{\mathrm{br}} = \frac{E}{X_0}. \tag{2.33}$$

One can transform this into an energy loss over time:

$$\left\langle -\frac{\mathrm{d}E}{\mathrm{d}t}\right\rangle_{\mathrm{br}} = \frac{c\rho}{X_0}E = \frac{E}{\tau_{\mathrm{br}}}. \tag{2.34}$$

The ISM mainly consists of hydrogen ($X_0 = 63\,\mathrm{g}\cdot\mathrm{cm}^{-2}$) and its mass density is $\rho = n_p \cdot m_p$, where n_p is the mass density and m_p is the mass of the proton. Thus, the cooling time τ_{br} for an electron traveling with a velocity close to c due to bremsstrahlung is:

$$\tau_{\mathrm{br}} = \frac{X_0}{c \cdot m_p \cdot n_p} \approx \frac{1}{n_p \cdot \mathrm{cm}^3} \cdot 10^{15}\,\mathrm{s}. \tag{2.35}$$

In this process, the cooling time is independent of the electron energy, and hence the shape of the electron spectrum and the γ-ray spectrum is the same.

Synchrotron Radiation

An electron can also be deflected in a magnetic field $\vec{B}$ by the Lorentz force

$$\frac{\mathrm{d}\vec{p}}{\mathrm{d}t} = \frac{e}{m}\left(\vec{p}\times\vec{B}\right). \tag{2.36}$$

and emits photons due to the resulting acceleration. This process is called synchrotron radiation and it is the main contribution to the non-thermal emission in the radio and X-ray regime.

In an homogeneous magnetic field the solution of the differential equation is a helix trajectory with the following gyro radius in the plane perpendicular to $\vec{B}$:

$$r_B = \frac{p}{eB} \tag{2.37}$$

Because of the deflection, the electron emits synchrotron radiation. In the center of momentum frame of the electron the radiation follows the characteristic of a dipole. In the frame of the observer the radiation is collimated in the direction of the movement of the electron which has the velocity v.

The energy loss due to synchrotron radiation is

$$\left\langle -\frac{\mathrm{d}E}{\mathrm{d}t}\right\rangle_{\mathrm{syn}} = \frac{4}{3}\sigma_T c U_{\mathrm{mag}}\beta^2\gamma^2, \tag{2.38}$$

where $\beta = \frac{v}{c}$ and σ_T is the Thomson cross-section:

$$\sigma_T = \frac{8\pi r_e^2}{3} = \frac{8\pi}{3}\left(\frac{e^2}{4\pi\epsilon_0 m_e c^2}\right)^2 = 0.665\,\mathrm{barn}. \tag{2.39}$$

The energy density U_{mag} of the magnetic field is given by:

$$U_{\mathrm{mag}} = \frac{B^2}{2\mu_0} = 250 \left(\frac{B}{100\,\mu\mathrm{G}} \right)^2 \mathrm{eV\,cm^{-3}}. \tag{2.40}$$

The cooling time due to synchrotron radiation τ_{syn} is defined as follows:

$$\tau_{\mathrm{syn}} = \frac{E}{\left\langle -\frac{\mathrm{d}E}{\mathrm{d}t} \right\rangle_{\mathrm{syn}}} \approx 4 \cdot 10^{10} \left(\frac{B}{100\,\mu\mathrm{G}} \right)^{-2} \left(\frac{E}{1\,\mathrm{TeV}} \right)^{-1} \mathrm{s}. \tag{2.41}$$

The energy loss depends on the magnetic field strength and it is more efficient for higher energies. Therefore the γ-ray spectrum produced by the electrons is steeper than the underlying electron spectrum.

Inverse Compton scattering

The inverse Compton scattering (IC) is the scattering of an energetic electron with a low energetic photon. The process is called inverse Compton scattering since the electron loses energy and the photon gains energy, in contrast to the Compton scattering where it is vice versa. This process can produce photons with energies up to the TeV energy range.
The Klein-Nishina formula represents the total cross section σ_C for the Compton scattering with $\epsilon = \frac{E_\gamma}{m_e c^2}$ (see Longair (2011)):

$$\sigma_C = 2\pi r_e^2 \left[\frac{1+\epsilon}{\epsilon^2} \left(\frac{2(1+\epsilon)}{1+2\epsilon} - \frac{1}{\epsilon} \ln(1+2\epsilon) \right) + \frac{1}{2\epsilon} \ln(1+2\epsilon) - \frac{1+3\epsilon}{(1+2\epsilon)^2} \right]. \tag{2.42}$$

In the following two limits are given. The first one is the Thomson regime ($\epsilon \ll 1$) and the second one is for ultra relativistic electrons ($\epsilon \gg 1$):

$$\sigma_C \approx \begin{cases} \sigma_T (1-2\epsilon) \approx \sigma_T & \text{for} \quad \epsilon \ll 1 \quad \text{(Thomson regime)} \\ \frac{3}{8}\sigma \frac{1}{\epsilon} \left(\ln(2\epsilon) + \frac{1}{2} \right) & \text{for} \quad \epsilon \gg 1 \quad \text{(ultra relativistic)} \end{cases}.$$

The Thomson regime is applicable for electron energies of $E_e \ll 250\,\mathrm{TeV}$ which is the case for the whole observable range of the VHE γ-ray experiments.

In this regime the energy loss due to IC scattering is

$$\left\langle -\frac{\mathrm{d}E}{\mathrm{d}t} \right\rangle_{IC} = \frac{4}{3} \sigma_T c U_{\mathrm{rad}} \beta^2 \gamma^2. \tag{2.43}$$

Under the assumption that the photon is part of the Cosmic microwave background which has an energy density of $U_{\mathrm{rad}} = 0.26\,\frac{\mathrm{MeV}}{\mathrm{m}^3}$ the cooling time is

$$\tau = \frac{E}{\left\langle -\frac{\mathrm{d}E}{\mathrm{d}t} \right\rangle_{\mathrm{rad}}} \approx 4 \cdot 10^{13} \left(\frac{E}{1\,\mathrm{TeV}} \right)^{-1} \mathrm{s}. \tag{2.44}$$

2.4 Observations of Supernova Remnants by H.E.S.S.

After the explanation of the evolution and the morphology of SNRs and the processes responsible for the production of VHE γ-rays the focus is now on the observations of supernova remnants by the H.E.S.S. experiment (see Section 3.3). Up to now H.E.S.S. has detected 14 SNRs which fall into two groups: SNRs interacting with molecular clouds and shell-type SNRs.
The first group consists of eight SNRs. For the interpretation of the VHE γ-ray observations the interaction of hadrons accelerated in SNRs with molecular clouds is preferred (Hinton 2004). For completeness a list of the sources in this group is given with the source names and a corresponding reference but they are not of further interest in this dissertation:

- HESS J1745 − 203 (Aharonian et al. 2008a)
- CTB 37A (Aharonian et al. 2008b)
- W 28 (Aharonian et al. 2008d)
- HESS J1800 − 240A, HESS J1800 − 240B, HESS J1800 − 240C (three nearby sources) (Aharonian et al. 2008d)
- W 49B (Brun et al. 2011)
- HESS J1457 − 593 (Hofverberg et al. 2011)

The second group consists of six potential shell-type SNRs. This group is of special interest since it allows spatially resolved studies of the acceleration of particles in a SNR shell and a comparison to the theories of their acceleration. These SNRs are younger and it should be mentioned that hadron-dominated scenarios are also preferred for this group, but lepton-dominated scenarios cannot be excluded.
Due to the low angular resolution of the VHE experiments the unveiling of these shells is quite challenging in contrast to other wavebands. So far H.E.S.S. was able to reveal the shell-like structure of four SNRs in this group:

- RX J1713.9 − 3946 (2004) (Aharonian et al. 2006b)
- RX J0852 − 4622 (2005) (Aharonian et al. 2007)
- SN 1006 (2009) (H.E.S.S. Collaboration et al. 2010)
- HESS J1731 − 347 (2011) (H.E.S.S. Collaboration et al. 2011)

The date of the detection by H.E.S.S. is given in brackets and VHE γ-ray images of the different SNRs are shown in Fig. 2.3.

Another SNR in this group is CTB 37B (Aharonian et al. 2008c) and the uncovering of its shell is still under investigation.

For RCW 86, the sixth remnant of the group, the situation is special. Up to now the H.E.S.S. Collaboration was able to publish the detection of RCW 86. The final proof, if RCW 86 belongs to the group of shell-type SNRs (Aharonian et al. 2009) is still missing. Hence, in the next section a detailed introduction to RCW 86 is presented. Furthermore a new detailed analysis of the shell-type morphology of RCW 86 is the subject of this thesis and presented in Chapter 4.

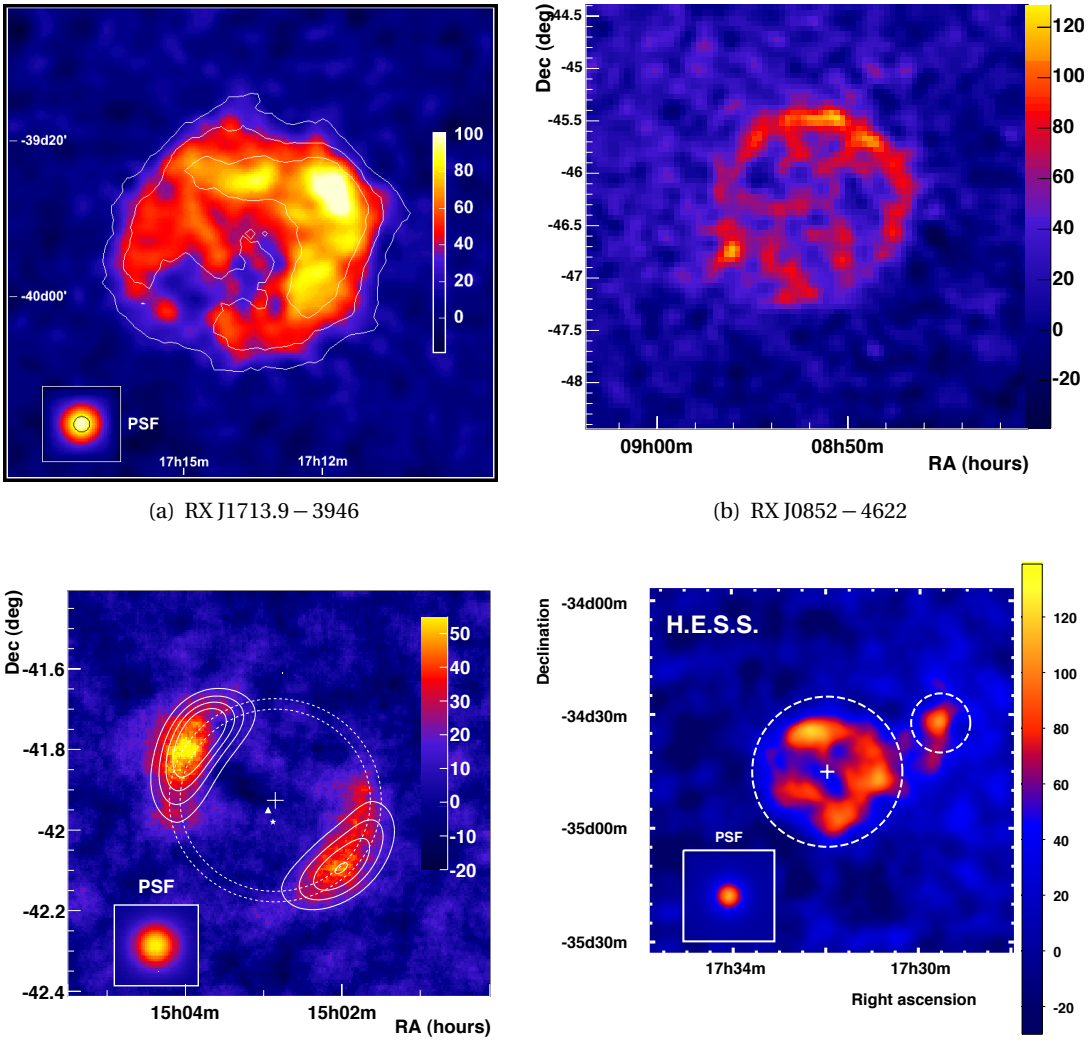

(a) RX J1713.9 − 3946

(b) RX J0852 − 4622

(c) SN 1006

(d) HESS J1731 − 347

Figure 2.3: The shell-type supernova remnants seen by H.E.S.S. in chronological order of their detections. (Images are taken from the H.E.S.S. publications with the most detailed morphology of the source. Ref. see text.)

2.5 The Case of RCW 86

RCW 86 (also known as G315.4 − 2.3 and MSH14 − 63) is possibly associated with the historical supernova SN 185 (Green 2002). First discovered in 1961 as the radio source MSH 14 − 63 during a radio survey observation (Mills et al. 1961), it was identified in 1967 as a supernova remnant with a shell-like structure with a diameter of 40', radio polarization and a non-thermal spectrum (Hill 1967). The spectral index in the radio band was determined to be $\alpha = -0.47$ (Caswell et al. 1975). More recent radio data of the *Australia Telescope Compact Array* (ATCA) observed at a frequency of 1.34 GHz (Dickel et al. 2001) showed that the South-West (SW) rim is colliding with dense gas. In Figure 2.4 the 1.34 GHz radio contours (Dickel et al. 2001) are overlaid over a Hα data set (from Smith (1997)). A general agreement of the morphologies is visible.
From optical observations (Rosado et al. 1996) the distance and the age of RCW 86 was estimated to be (2.8±0.4) kpc and 9500 years, respectively.

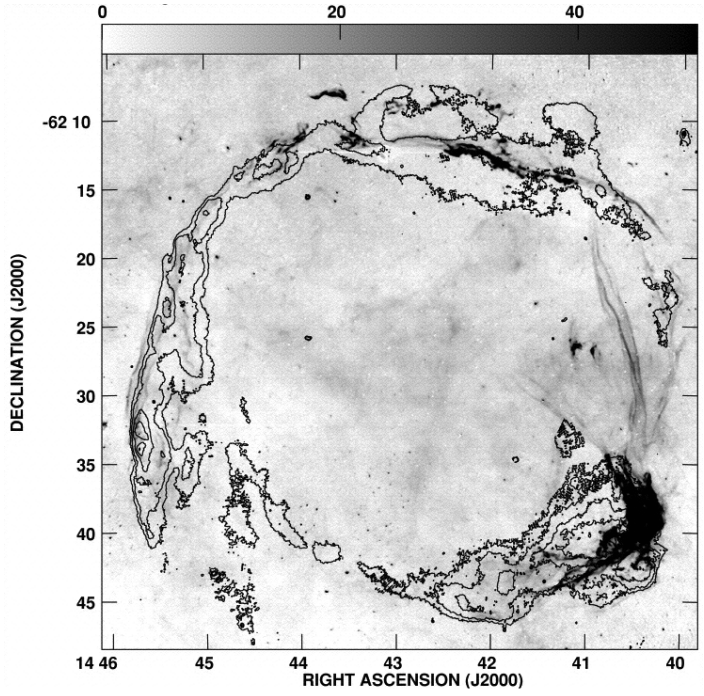

Figure 2.4: Hα data in gray scale (Smith 1997)) overlaid with the 1.34 GHz radio contours of the supernova remnant RCW86. (Figure taken from Dickel et al. (2001)).

In X-rays, RCW 86 was discovered during the *Apollo-Soyuz* mission of the *Apollo* spacecraft (Naranan et al. 1977). In 1984 the first spatially resolved X-ray image obtained by the *Einstein Observatory* confirmed the shell-like structure in X-rays and the extent of RCW 86 was in agreement between the X-rays and the radio data (Pisarski et al. 1984).

The data from the *Advanced Satellite for Cosmology and Astrophysics* (ASCA) indicated that RCW 86 is in the Sedov evolutionary phase and the SNR is spatially consistent with SN 185 A.D. (Bamba et al. (2000), Borkowski et al. (2001)). For the SW and North-East (NE) parts of RCW 86 X-rays produced by synchrotron radiation were observed which has a photon index of 3.1 ± 0.1.

In 2006 observations of the NE part of the remnant by the *Chandra* and *X-ray Multi-Mirror Mission - Newton* (XMM-Newton) satellites strengthened the case that RCW 86 is the remnant of SN 185

(Vink et al. 2006). The data agreed with the scenario of a SNR expanding into a windblown bubble from a progenitor star (Dickel et al. (2001),Vink et al. (1997)) and is presented in Fig. 2.5. Following this scenario large parts of the SNR shell interact with the surrounding shell of the bubble. Hence, the large density contrast in the remnant and the large variety of shock velocities can be explained (Helder et al. 2009). Furthermore this scenario can emphasize, that the NE part is completely dominated by X-ray synchrotron radiation, similar to SNRs RX J1713 − 394 and Vela Junior. This part of the shock seems to plow through a low-density medium. In contrast, the SW part consists of high-density material providing an ideal target for accelerated ions. Therefore it is a potential source of γ-rays emitted through π° decay (Bocchino et al. 2000). These morphology differences are making RCW 86 an ideal candidate for the study of acceleration of cosmic rays in SNRs under different conditions. The distance and age was estimated to be 2.5 kpc (Sollerman et al. (2003) and References therein) and 2250 yrs (Vink et al. 2006), respectively.

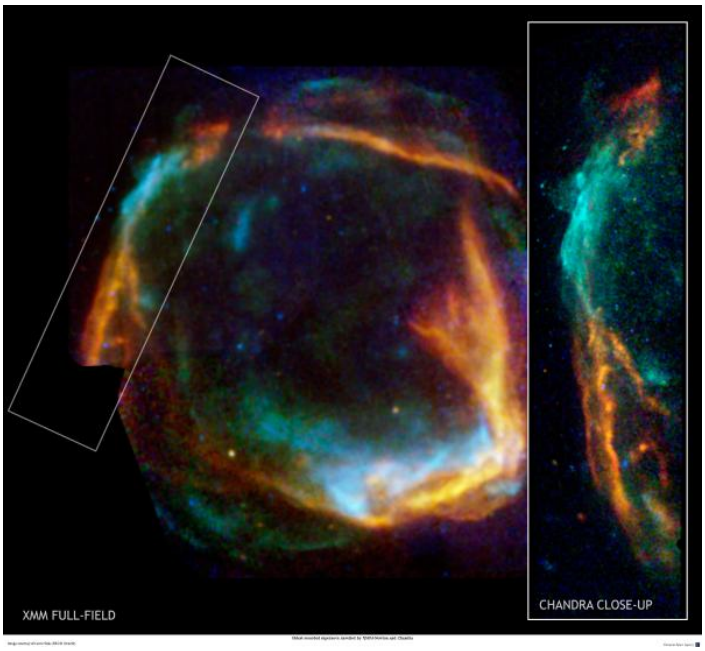

Figure 2.5: The left panel shows the XMM-Newton image of RCW 86; The right panel includes the Chandra image of the Northeast rim as a close-up. The color code is the same for both images and indicates the energies as followed: Red: 0.5-1 keV, Green: 1-1.95 keV, Blue: 1.95-6.6 keV. Credit: XMM-Newton: ESA/Univ. of Utrecht/J.Vink et al. (left), Chandra: NASA/CXC/Univ. of Utrecht/J.Vink et al. (right).

The multi-wavelength analysis with new infrared observations (see Fig. 2.6) by *Spitzer Space Telescope* and the *Wide-Field Infrared Survey Explorer* and X-ray data agreed with the scenario of a SNR expanding into a windblown bubble (Williams et al. 2011). By the use of a 2D hydrodynamic model for the supernova the different densities and velocities in the supernova can be explained by the fact that the explosion was not located in the middle of the windblown bubble but slightly offset. Therefore the shock front has reached the surrounding shell in the SW but not yet in the NE. The fact that RCW 86 is the remnant of SN 185 is also supported by these observations. In most of the previous publications the supernova was related to a Type II[2] origin (core collapse) (Dickel et al. (2001),Vink et al. (1997)). In contrast to these publications Williams et al. (2011) showed that, while

[2]A Type II supernova takes place when the pressure of the nuclear fusion processes inside a high-mass (more than 1.1 solar masses) star is no longer capable of compensating the pressure of the gravitational force of its entire mass

not all of the different scenarios for a type II origin can be ruled out, a supernova with a Type Ia[3] origin is favored.

Figure 2.6: *Spitzer* and *WISE* mosaic of the entire remnant, with *Spitzer* 24 μm emission in red, *WISE* 12 μm emission in green, and *WISE* 4.6 μm emission in blue. Only the brightest sections of the NW and SW are visible at 12 μm

In the GeV regime *Fermi* was not able to detected RCW 86 so far with its published 24 months of data taking (The Fermi-LAT Collaboration 2011).

In the VHE regime RCW 86 was observed by H.E.S.S. between 2004 and 2007 and its detection was published in 2009 (Aharonian et al. 2009). The VHE γ-ray image is given in Fig. 2.7. In contrast to the other wavelength the shell-like structure of RCW 86 is not yet confirmed.

Figure 2.8(a) shows the radial profile together with the fit results of a sphere- and a shell-like morphology to the data. Both morphology models are not excluded by the data.
The differential energy spectrum of RCW 86 is shown in Figure 2.8(b). Based on the published data, a distinction between a pure power law and a exponential cut-off power law is not possible, as both presented equally good fits to the measured spectrum. The spectral index of the pure power-law fit is $2.54 \pm 0.12_{\mathrm{stat}} \pm 0.20_{\mathrm{sys}}$. A more detailed discussion can be found in the H.E.S.S publication (Aharonian et al. 2009).

[3] A Type Ia supernova occurs in a binary system which is made up of a white dwarf and a companion star

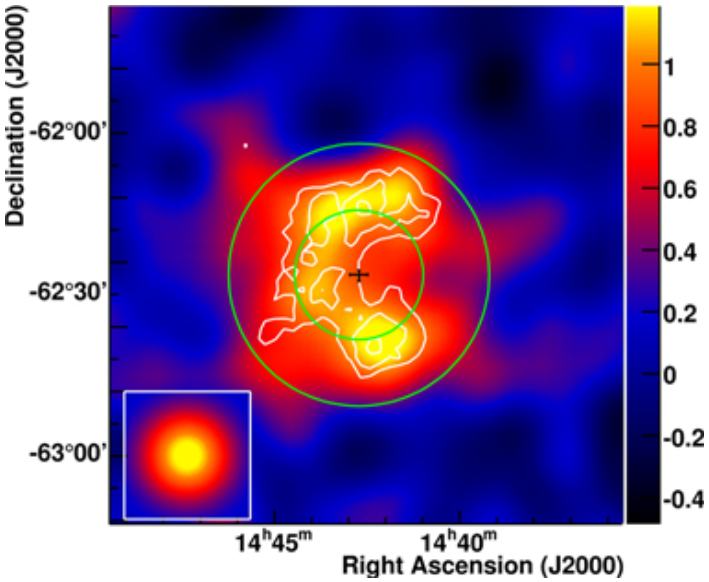

Figure 2.7: The VHE γ-ray image from Aharonian et al. (2009).The map is based on the Hillas momentum analysis. The point-spread function is shown as an inlet in the lower left-hand corner. The black cross marks the center of the fitted shell. The green circles correspond to the inner and outer radii of this shell.

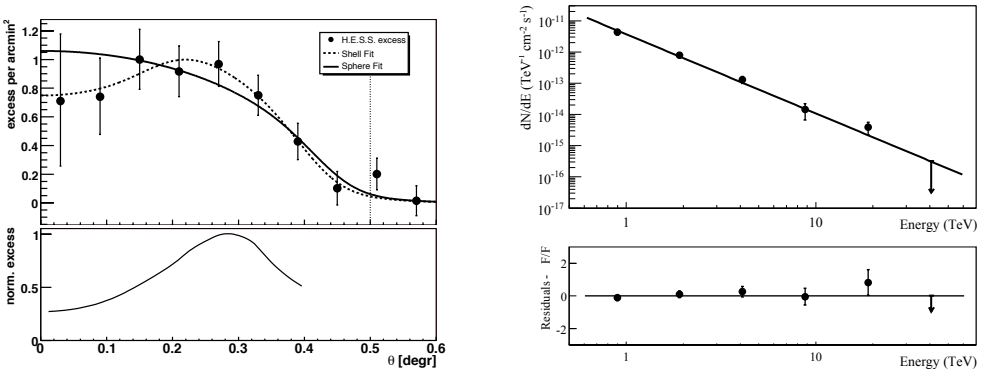

(a) radial profile

(b) Differential γ-ray energy spectrum

Figure 2.8: (a) The radial profile plot around the fitted SNR center is presented. The H.E.S.S. excess is marked by black dots. Two models fitted to the data are shown, a thick and spherically symmetric shell (dashed line) and a uniformly-emitting sphere (solid line).
(b) Differential γ-ray energy spectrum of RCW 86 measured by H.E.S.S.. A pure power law is fitted to the data and yields a spectral index of $2.54 \pm 0.12_{\mathrm{stat}} \pm 0.20_{\mathrm{sys}}$.

3 H.E.S.S. and the Imaging Atmospheric Cherenkov Technique

In the end of the previous chapter, the current view of RCW 86 was presented. The large size and the non-thermal X-ray emission made the remnant a promising target for VHE γ-ray observations.

For the detection of VHE γ-rays the ground-based Imaging Atmospheric Cherenkov Technique (IACT) is the most successful. At energies below 10 GeV the direct detection with satellite experiments is possible, while at higher energies, the γ-ray flux steeply declines and the small detection area of a few square meter makes the detection more and more complicated. Therefore at higher energies the indirect measurements of VHE γ-rays with the IACT is the technique of choice. The Earth's atmosphere is used as detector material. A VHE γ-ray enters the atmosphere interacts and a so-called air shower develops which can be detected by the Cherenkov radiation which is emitted by the charged particles of the shower.

In this chapter, the generation of air showers and their properties are discussed as well as the differences between air showers initiated by hadrons or γ-rays. Afterward emission of Cherenkov radiation and the absorption in the atmosphere is briefly summarized. In Section 3.2 the IACT is explained and the High Energy Stereoscopic System (H.E.S.S.), one of the currently working Cherenkov telescope experiments, is presented.

3.1 Air Showers

A VHE particle interacts with atom nuclei in the upper layers of the atmosphere and secondary particles are released. These secondary particles interact again with the atmosphere and initiate an air shower. The shower is growing until absorption effects of the atmosphere dominate over the production. Depending on the type of primary particle one distinguishes between electromagnetic and hadronic air showers. An electromagnetic air shower is initiated by photons, electrons or positrons. Hadronic air showers are produced by hadrons. The type of air showers can be identified mainly by their differences in the longitudinal and lateral expansion.

3.1.1 Electromagnetic Air Showers

An electromagnetic air shower develops through the alternation of pair production and Bremsstrahlung processes. When an electron hits the atmosphere a photon is emitted, which afterward decays in an electron-positron pair, the electrons/positrons in turn emit photons and so on. These processes continue as long as the electron energy reaches the critical energy $E_{\text{crit.}}$. Afterward ionization losses dominate. A simple model introduced by Heitler (Heitler 1954), which is shown in Fig. 3.1, can explain the main characteristics of the shower development. This model does not include fluctuations, ionization losses and the energy dependence of the cross-section in the air shower. For simplicity the radiation length X_0 is set to be the same for pair production and Bremsstrahlung and it is assumed, that the energy is equally distributed among the secondary particles.

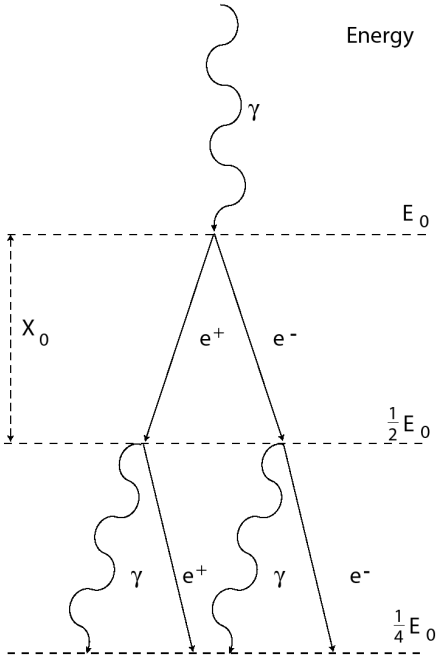

Figure 3.1: Heitler model of an electromagnetic air shower (Heitler 1954) (Figure adopted from Jung (2003))

A primary γ-ray with the energy E_0 generates an electron-positron pair after traversing the radiation length X_0. After an additional radiation length X_0 each particle emits one γ-ray through Bremsstrahlung. Subsequently the process reiterates. After each radiation length X_0 the energy of the particles E is divided in half and the number of particles is doubled. Therefore after n radiation lengths this results in an energy E_n of the particles of

$$E_n = E_0 \cdot 2^{-n} \tag{3.1}$$

and a total number of particles N_n:

$$N_n = 2^n. \tag{3.2}$$

The shower development breaks down when the energy of the particle falls below the critical energy $E_{\text{crit.}}$. In our atmosphere $E_{\text{crit.}}$ is 81 MeV and the maximal number of secondary particles $N_{\max}$ is reached. If the energy falls below the critical energy ionization losses dominate.

$$N_{\max} = \frac{E_0}{E_{\text{crit.}}} \tag{3.3}$$

The corresponding maximal shower depth is:

$$X_{\max} = X_0 \frac{\ln(E_0/E_{\text{crit.}})}{\ln 2} \tag{3.4}$$

Afterward the number of particles starts to decline until, after many scattering processes, all particles are completely absorbed.

The model of Heitler describes the main characteristics of an electromagnetic air showers:
the particle number increases exponentially until the maximum is reached, the maximal shower

depth $X_{\max}$ increases logarithmically with the primary energy E_0 and the maximal number of particles $N_{\max}$ is proportional to the primary energy E_0. A more detailed description of the shower development is presented in Longair (2011).

3.1.2 Hadronic Air Showers

In contrast to an electromagnetic air shower, an hadronic air shower is initiated by protons, neutrons or atomic nuclei. The interaction with the nucleons of the Earth's atmosphere through inelastic scattering is responsible for the creation of the shower. A huge number of secondary particles is produced which subsequently interact with nucleons of the Earth's atmosphere. This leads to an hadronic air shower.

Under the assumption of a primary proton, it interacts with a nucleon of the Earth's atmosphere and produces mainly pions ($\pi^0, \pi^\pm$) and a few kaons and hyperon states (e.g. Λ, Σ, Ξ). In this interaction the proton loses the main part of its energy and remains close to the shower axis. The secondary particles receive a transverse momentum and are scattered away from the shower axis. The neutral pions π^0 decay almost instantly ($\tau_{\pi^0} = 8.3 \times 10^{-17}$ s) into two γ-rays and initiate an electromagnetic air showers:

$$\pi^0 \rightarrow \gamma + \gamma. \tag{3.5}$$

The charged pions $\pi^\pm$ either interact inelastically or decay. Which process is dominant depends on the energy of the pion and the density of the surrounding medium. A pion with an energy of 1 GeV has a 100 times higher probability to decay then to interact in the upper atmosphere. At energies above ~ 100 GeV the probability of decay and inelastic interactions is almost the same.

The interaction of charged pions $\pi^\pm$ with nucleons of the Earth's atmosphere initiates hadronic sub-showers. The pions decay into muons:

$$\pi^+ \rightarrow \mu^+ + \nu_\mu$$
$$\pi^- \rightarrow \mu^- + \overline{\nu_\mu}$$

Due to their low interaction rate and their long enough life time a large amount of muons reach the Earth's surface. Only some of the low energetic muons decay into electrons:

$$\mu^+ \rightarrow e^+ + \nu_e + \overline{\nu_\mu}$$
$$\mu^- \rightarrow e^- + \overline{\nu_e} + \nu_\mu.$$

In Fig. 3.2 a schematic of an hadronic air shower is shown.

A hadronic air shower is composed of an hadronic component which is focused along the shower axis, an electromagnetic component and a muon component which are spread widely away from the shower axis. The electromagnetic component is mainly responsible for the atmospheric Cherenkov light . For comparison Fig. 3.3 shows a simulation of the development of an air shower initiated by a photon with an energy of 300 GeV or a proton with an energy of 1 TeV.

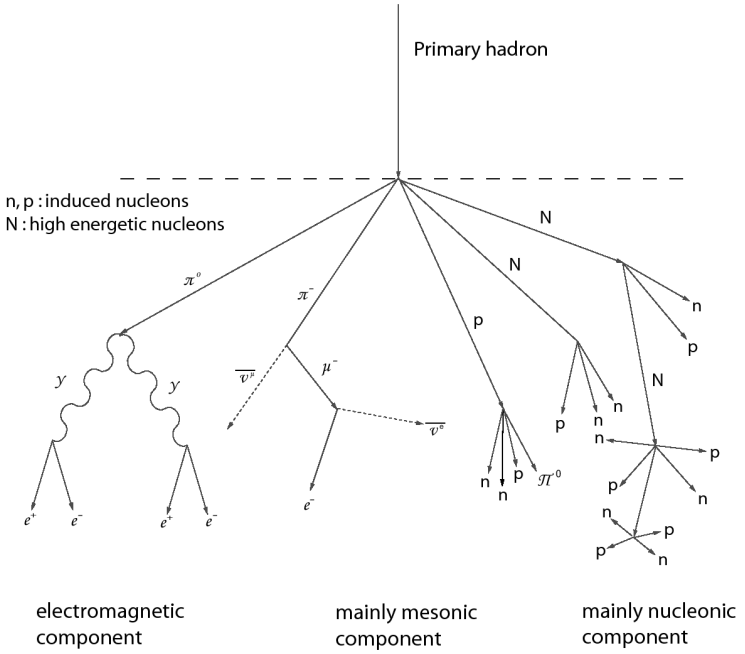

Figure 3.2: Schematic of an hadronic air shower.

3.1.3 Cherenkov Radiation

If a charged particle moves through a dielectric medium with a speed v exceeding the speed of light in this medium the molecules of the medium are polarized. The subsequently depolarization induces a coherent emission of electromagnetic radiation. The superposition of the coherent waves (according to Huygens's principle) leads to the formation of a wave front with a linear propagation (see Fig. 3.4). This radiation is called Cherenkov radiation. The opening angle (Cherenkov angle) θ_C of the wave front is determined by the velocity v of the particle the speed of light c in vacuum and the refractive index of the medium n:

$$\theta_C = \arccos\left(\frac{c}{n \cdot v}\right) \tag{3.6}$$

Cherenkov radiation is emitted if $v \geq \frac{c}{n}$. This corresponds to an energy threshold of $E_{\min}$ which can be expressed in terms of the rest mass of the particle m_0:

$$E_{\min} = \frac{m_0 c^2}{\sqrt{1 - \frac{1}{n^2}}} \tag{3.7}$$

The charged secondary particles of an air shower with an energy greater than the threshold energy emit Cherenkov radiation. An electromagnetic air shower with an incident electron with an energy of 1 TeV has a typical shower maximum of ≈ 8 km and a Cherenkov angle of $\approx 1°$. This results in an illuminated circular area on the ground with a radius of about 120 m and about 100 Cherenkov photons per m^2. The Cherenkov photons have a wavelength between 350 nm and 550 nm. While

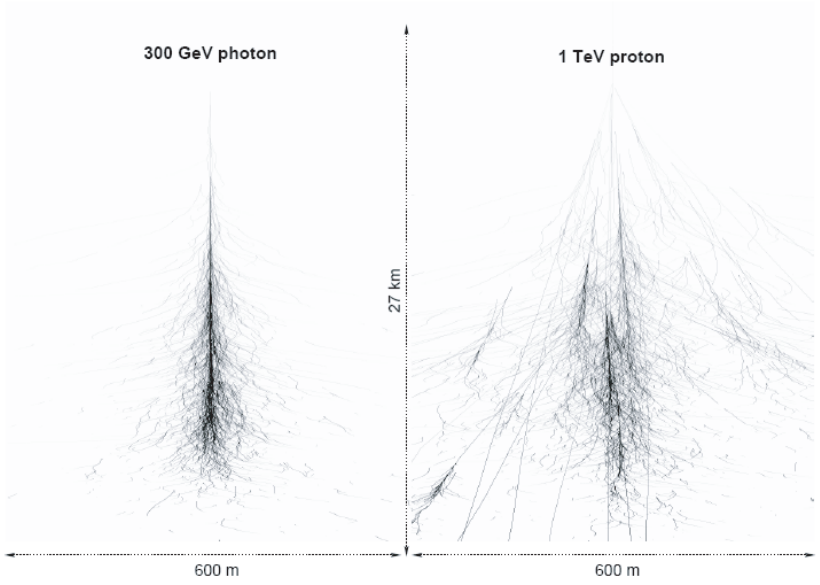

Figure 3.3: Simulation of the development of an air shower initiated by a photon with an energy of 300 GeV (left side) and of an air shower initiated by a proton with an energy of 1 TeV (right side) . The image is produced by Monte Carlo simulations and shows the projected tracks of particles in an air shower. (Bernlöhr 2010).

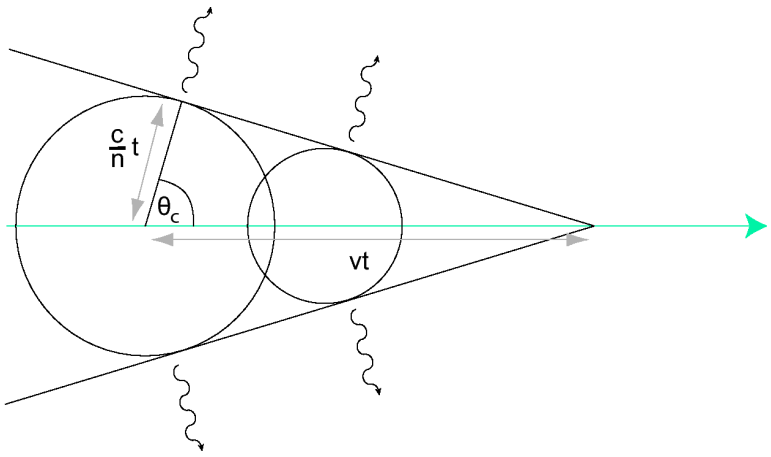

Figure 3.4: Emission of the Cherenkov radiation. The radiation is emitted at an angle θ with respect to the velocity of the charged particle.

passing through the atmosphere the Cherenkov photons are absorbed or scattered. Mainly three processes take place:

- Rayleigh scattering: Elastic scattering of electromagnetic radiation on particles of a size much smaller than the wavelength of light. The total cross section is $\approx \frac{1}{\lambda^4}$, i.e. short wavelength are preferred.
- Mie scattering: Scattering on particles with approximately the same diameter as the wavelength of the photons. Therefore a strong dependency on the particle size distribution exists. Under a realistic assumption of the distribution the cross-section depends on λ as $\approx \frac{1}{\lambda^{1...1,5}}$.
- Absorption by Ozone by photon dissociation: Cherenkov photons with an wavelength of $200-300\,\mathrm{nm}$ are almost completely absorbed by the process of breaking up ozone $O_3 + h\nu \rightarrow O_2 + O$.

3.2 The Imaging Atmospheric Cherenkov Technique

The previous sections discussed the generation of air showers and their Cherenkov radiation. This Section summarizes briefly the detection of these showers.

Imaging Atmospheric Cherenkov Telescopes are used for the detection of Cherenkov radiation of VHE γ-rays inducing air showers in the energy range between 0.05 and 100 TeV. The Earth's atmosphere serves as detector material. A primary γ-ray initiates an air shower which illuminates at ground an area of about 100 m radius, the so-called Cherenkov light pool. A telescope situated inside this light pool can detect the shower. Therefore the detection area is large about $10^5\,\mathrm{m}^2$, which is important due to the low γ-ray flux. The air showers last only about 10 ns. Hence fast detectors are needed, which is mostly realized by the use of Photomultiplier tubes as light sensors and fast read out electronics.

Imaging Atmospheric Cherenkov Telescopes possess large optical reflectors which isogonally project the Cherenkov light of an air shower into a camera. The camera is mounted in the focus of the reflector (see Figure 3.6). Parallel light beams are mapped onto a single spot. Thereby the properties of the primary particles can be reconstructed from the taken pictures. The signal height is a measure for the energy, the direction can be reconstructed because of the isogonal projection. The shower images of γ-ray air showers are elliptical while the one of hadronic air showers are broader and more diffuse. Therefore a separation between γ-ray induced air showers and hadronic ones is possible. Details about the reconstruction methods are given in Section 3.4.2.

History of the IACT

The VHE γ-ray astronomy started in 1989 with the detection of the Crab Nebula by the Whipple collaboration with a single Imaging Atmospheric Cherenkov telescope (Weekes et al. 1989). The next generation of IACT telescopes started with the HEGRA experiment which pioneered the stereoscopic approach, i.e. the use of several telescope. With this approach the reconstruction was improved significantly because of the different viewing angles of the showers and the better background suppression. A detailed description is given, e.g, in Longair (2011) and Jung (2003). The main player of the current generation of IACT telescope arrays are MAGIC[1] and VERITAS[2]

[1] http://magic.mppmu.mpg.de/
[2] http://veritas.sao.arizona.edu/

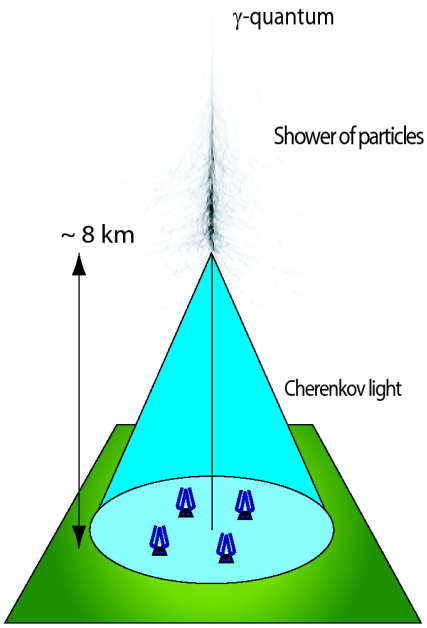

Figure 3.5: Detection of Cherenkov radiation from an air shower by the use of an IACT telescope array

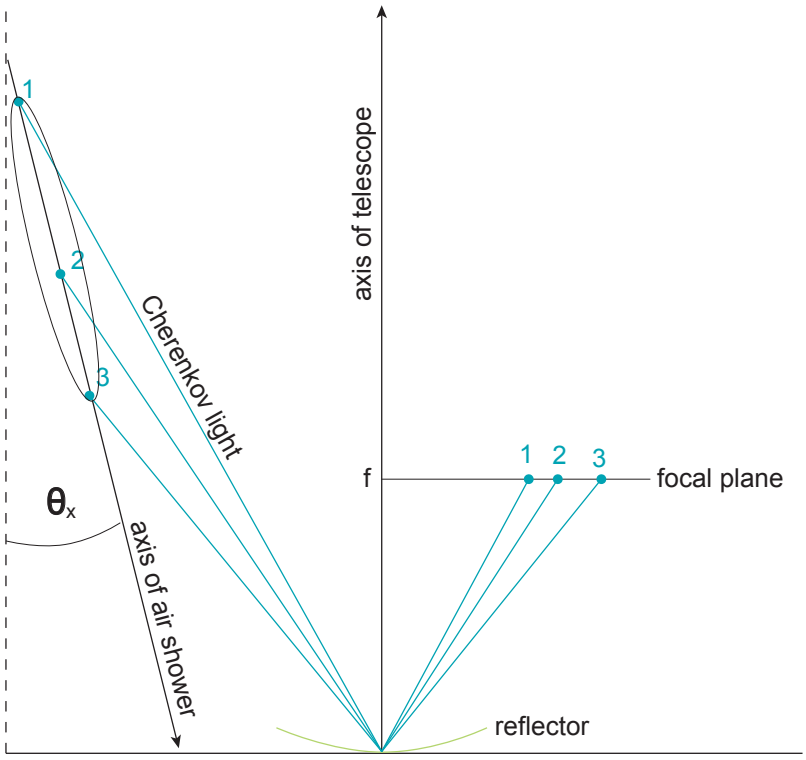

Figure 3.6: Isogonal projection of an elliptical air shower in the camera.

on the northern hemisphere and CANGAROO III[3] and H.E.S.S.[4] on the southern hemisphere. With these four experiments more than 120 sources have been detected in the last decade. At the moment the MAGIC, VERITAS and H.E.S.S. experiments are upgrading their systems. The H.E.S.S. collaboration is constructing a fifth large H.E.S.S. II telescope with a mirror area of about 600 m^2 to reduce the energy threshold. The future is CTA[5] which will consist of up to 100 telescopes. CTA is designed to yield an improvement in sensitivity by a factor of $5-10$.

3.3 H.E.S.S. Experimental Layout

In the previous section a brief summary of the development in the field of IACTs and the experiments for ground-based detection of VHE γ-rays were given. The subject of the thesis presented here, is the analyses of the SNR RCW 86 observed by H.E.S.S. Therefore in the following, the focus will be on the "High Energy Stereoscopic System" (H.E.S.S.). In this section a short overview of the experimental layout followed by a more detailed description of the analysis technique is given.

The H.E.S.S. experiment is located at the Farm Göllschau in the Khomas highland of Namibia (see Fig. 3.7) at an altitude of 1800 m. The geographic position is: latitude of 23° 16′ 18″ and eastern longitude of 16° 30′ 00″. The site is situated at the southern hemisphere, which guarantees a perfect view of the galactic center and -plane. Additionally the observation conditions are excellent, among others the site has very good atmospheric conditions, many nights without clouds, clear sky, minor humidity and no additional resident light emission.

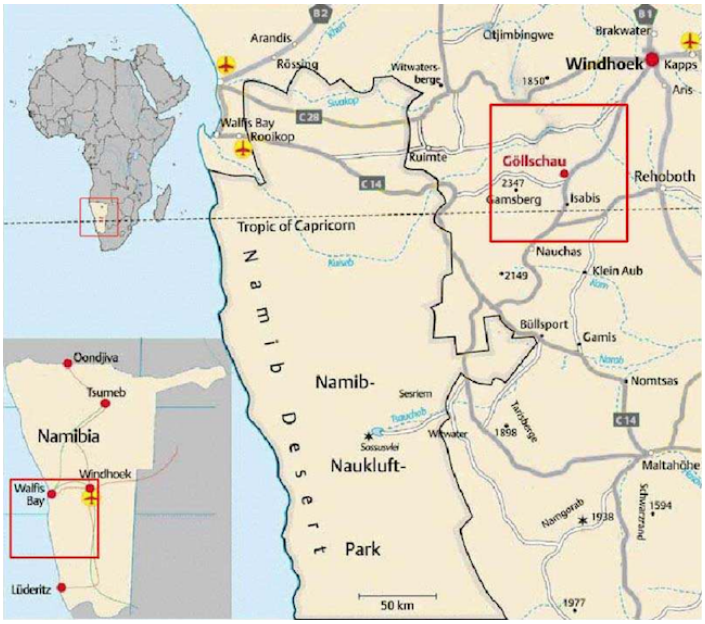

Figure 3.7: Location of the H. E. S. S. experiment on the Farm Göllschau in the Khomas highland of Namibia

In its first phase the experiment consists of four IACTs which are arranged in a square with a side length of 120 m. This configuration was determined by Monte-Carlo simulations (Konopelko & Plyasheshnikov 2000) to obtain the best sensitivity. The aerial photography in Fig. 3.8 shows the experiment with its four telescopes. The H.E.S.S. array (phase I) has been taking data since

[3] http://www.physics.adelaide.edu.au/astrophysics/cangaroo/
[4] http://www.mpi-hd.mpg.de/hfm/HESS/
[5] http://www.cta-observatory.org/

Figure 3.8: The H.E.S.S. Experiment (phase I) with its four IACT telescopes.

December 2003.

Each telescope has an altitude-azimuth mount and a reflector with a diameter of 13 m (see Fig. 3.9(a)). Due to the robust steel structure with a weight of ≈60 t the telescope can be pointed to a specific target position with an accuracy of $\approx 30''$.

The optical system uses the Davies-Cotton design. The total mirror area is 107 m^2 but only $\approx 95\,m^2$ are usable due to shadowing effects of the camera and the steel structure. The mirror consists of 380 round facets with a diameter of 30 cm which are mounted in a hexagonal order and can be aligned individually. This allows to obtain a focal spot with a radius of ≈ 0.4 mrad, which is well below the size of a single photo sensor in the camera. At the time of the mounting, each mirror had reflectivity of 80% in the wavelength range between 300 and 600 nm. Due to aging effects the reflectivity dropped over the years. With a refurbishment campaign from spring 2010 to autumn 2011 all telescopes have gained back their initial reflectivity. A detailed description of the optical system can be found in Bernlöhr et al. (2003).

The camera has a field of view of 5° and is composed of 960 pixels which are also mounted in a hexagonal order (see Fig. 3.9(b)). Each single pixel consists of a photomultiplier (PMT) with a light collector in front of the PMT and a readout electronics. The light collectors are installed to collect the light which falls between the PMTs. Further information can be found in Aharonian et al. (2004).

To reduce the amount of data and the background a two-level trigger system is installed. The camera is divided into 38 overlapping trigger-sectors consisting of 64 PMTs each and is triggered if more than four pixels have a signal above four photo electrons (p.e.) in one sector. This reduces events triggered by night sky background (NSB) only.

Subsequently, a coincidence trigger is used to store only events with at least two triggered telescopes within a time window of 60 ns. This second trigger reduces the background induced by muons nearly completely. Muons are local events and therefore trigger mostly one telescope. Additional information is provided in Funk et al. (2004).

Usually an observation has a length of 28 min and is performed in the so-called “wobble mode”. In this case the telescopes do not point right on the targeted source but instead use an offset of 0.5° to 1.5° to the source. Because of the isogonal projection the source has the same angular offset in the camera image from the center and it is possible to use the other side to estimate the still remaining background.

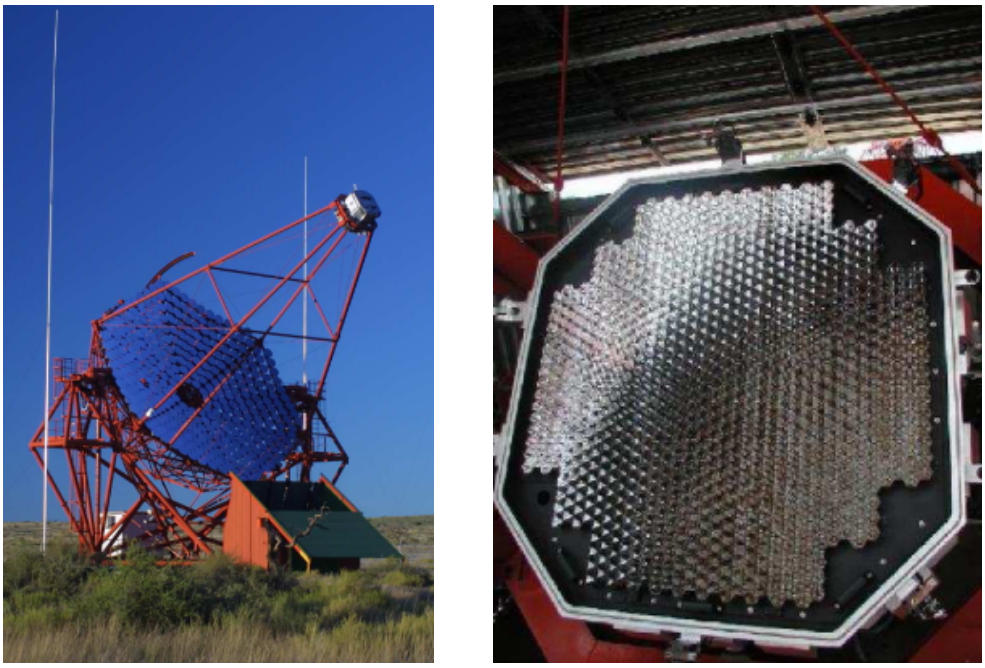

(a) (b)

Figure 3.9: In (a) a H.E.S.S. telescope is presented. It has an altitude-azimuth mount and a reflector with a diameter of 13 m. The H.E.S.S camera in (b) consists of 960 pixel which are mounted in a hexagonal order (Photographs taken from Komin (2006)).

Over the years, a data-taking efficiency of nearly 80% is reached, and each year about 330 h of data are recorded. The losses are mainly traced back to bad weather conditions. In the VHE γ-ray astronomy the sensitivity of an instrument is commonly expressed in units of the flux of the Crab nebula. The sensitivity of H.E.S.S. is given as: A point-like source with a flux of $2 \times 10^{-13}\,\mathrm{cm}^{-2}\,\mathrm{s}^{-1}\,\mathrm{m}$ can be detected with a significance of 5σ in 25 h of observation time. This value corresponds to a flux of 1 % of the Crab nebula flux. More mathematically speaking the value of $\geq 5\sigma$ is equivalent to a probability of 99.99985 % that it is not a statistical fluctuation.

3.4 H.E.S.S. Data Analysis

To ensure a high standard for the analyses and physics results obtained with the H.E.S.S. experiment the H.E.S.S collaboration uses different analysis techniques and two independent calibration chains to cross-check internally the results. Among others, different analyses are the "3D-model analysis" (Lemoine-Goumard, M. for the H.E.S.S. Collaboration 2005), the "Hillas moment analysis" (Benbow, W. for the H.E.S.S. Collaboration 2005) and the two improved analyses: Model++ (de Naurois & Rolland 2009) and the hap tmva analysis (Ohm et al. 2009). In the following the calibration, the "Hillas moment analysis" on which the simulation for the deconvolution in Chapter 5 is based and the Model++ analysis which is used for the analysis in Chapter 4 are presented in more detail.

3.4.1 Calibration

The camera consists of 960 pixels which are subdivided into groups of 16 pixels, so-called drawers. Within one drawer 8 PMTs are read-out by a acquisition cards. The card has two different gains. The first one is the high gain (HG) with an amplification of a factor of 50. This is used for the small signals. The second has an amplification of a factor 3 (low gain) and is used for the strong signals. The analog signals are then stored in the Analog Ring Sampler (ARS) with a time binning of 1 ns. After a trigger signal the ARS is read out. The integrated value over 16 ns are stored as an ADC^{HG} and ADC^{LG} value for the pixel. These values are converted into physical meaningful units, which is in this case the number of p.e. produced in the PMT. The signal in p.e. for the high gain A^{HG} (A^{LG}, respectively) is then given as:

$$A^{HG} = \frac{ADC^{HG} - P^{HG}}{\gamma_e^{ADC}} \times FF$$
$$A^{LG} = \frac{ADC^{LG} - P^{LG}}{\gamma_e^{ADC}} \times (HG/LG) \times FF$$

The parameters represent the following:

- P^{HG} and P^{LG} are the ADC mean of the base-lines (pedestals),
- γ_e^{ADC} is the gain of the HG channel in ADC counts per p.e.,
- HG/LG is the amplification ratio of the HG to the LG,
- and FF is the flat-field coefficient that accounts for differences in efficiencies of the pixels.

The HG value is used alone up to ∼150 p.e., the low gain above ∼200 p.e.. In the intermediate range, in which both gains are linear, a weighted values is used.

$$A = (1-\epsilon) \cdot ADC^{HG} + \epsilon \cdot ADC^{LG}$$

with $\epsilon \approx (ADC^{HG} - 150)/(200 - 150)$.

Determination of γ_e^{ADC}

In dedicated so-called single-photo electron runs the whole camera is illuminated by light pulses with an intensity of about 1 p.e. The obtained ADC count distribution of the high gain is fitted by the response function of the PMT given by:

$$N(x) = N_0 \left(\frac{e^{-\mu}}{\sqrt{2\pi}\sigma_{P^{HG}}} \cdot \exp\left[-\frac{1}{2} \left(\frac{x - P^{HG}}{\sigma_{P^{HG}}} \right)^2 \right] + \sum_{n=1}^{\infty} \frac{e^{-\mu}}{\sqrt{2\pi}\sigma_{\gamma_e^{ADC}}} \frac{\mu^n}{n!} \exp\left[-\frac{1}{2} \left(\frac{x - (P^{HG} + n\gamma_e^{ADC})}{\sqrt{n}\sigma_e^{ADC}} \right)^2 \right] \right)$$

with

- N_0 the normalization
- $\sigma_{P^{HG}}$, the width of the electronic pedestal
- $\sigma_{\gamma_e^{ADC}}$, the width of the single photo electron peak
- μ the mean light intensity of the illumination
- n the number of p.e.

As result one obtains among others the value of γ_e^{ADC}. In Fig. 3.10 the HG distribution of one pixel is shown. Two well distinguished peaks which correspond to the electronic pedestal and the 1 p.e. signal, are clearly visible. The fit of the response function to the data is overlaid in blue.

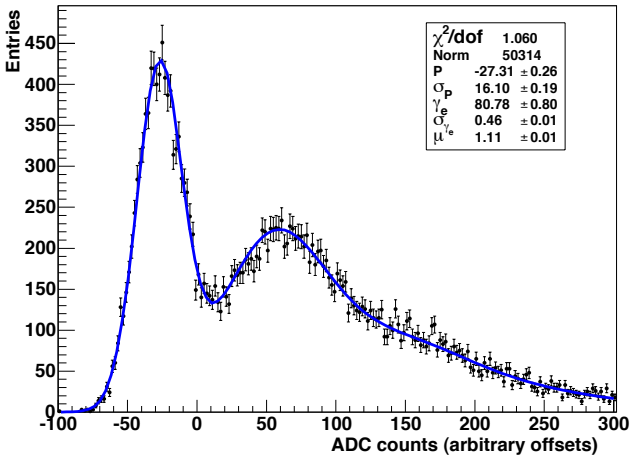

Figure 3.10: ADC count distribution for one pixel of a single-photo electron run with the fit of the PMT response function to the data overlaid in blue (Fig. from Aharonian et al. (2004))

Determination of the Ratio of the two Amplifications

For the determination of the ratio of the two amplifications (the so-called HG/LG-ratio) the linear range valid for both amplifications is used. To ensure clean signals, i.e. signals which are well above the noise level, only pixels with an amplitude between 30 - 150 p.e. are taken for the calculation of the ratio. For the calibration the mean value is used.

Determination of the Flat-Field Coefficients

Inhomogeneities are produced in the camera due to differences in the photo cathode- and light collection efficiencies. The flat-field coefficient takes this into account. A LED flasher is mounted

on the telescope dish and provides a uniform illumination of the whole camera. For the determination of the flat-field coefficient for each event the mean signal over the camera is determined and the deviation of each pixel to this value is calculated and stored. The inverse of the mean value of each pixel – the so-called flat-field coefficient (FF) – is then used for the correction of the pixel efficiency.

Typical calibration values and their stability, as well as further information are presented in Aharonian et al. (2004). An image of the camera with the raw high gain ADC counts is shown in Fig. 3.11(a).

3.4.2 Hillas Moment Analysis

The advantage of the Hillas moment analysis is its robustness. It was developed by Hillas in 1985 (Hillas 1985). The images of VHE γ-ray air showers are approximated by an ellipse and parametrized by the momenta of the light intensity distribution (LID). In the following the different steps of the analysis are presented.

Image Cleaning and Parametrization

The camera images of an air shower consists of pixels which either contain NSB noise or Cherenkov light signals from the air shower. In a first step the image is cleaned to get rid of pixels with noise signals. The so-called "tail-cuts" are applied: Pixels with an intensity above a threshold of 5 p.e. and a neighbor pixel with an intensity above 10 p.e. or the other way round are kept for further use, all others are set to zero. An example is given in Fig. 3.11(c).

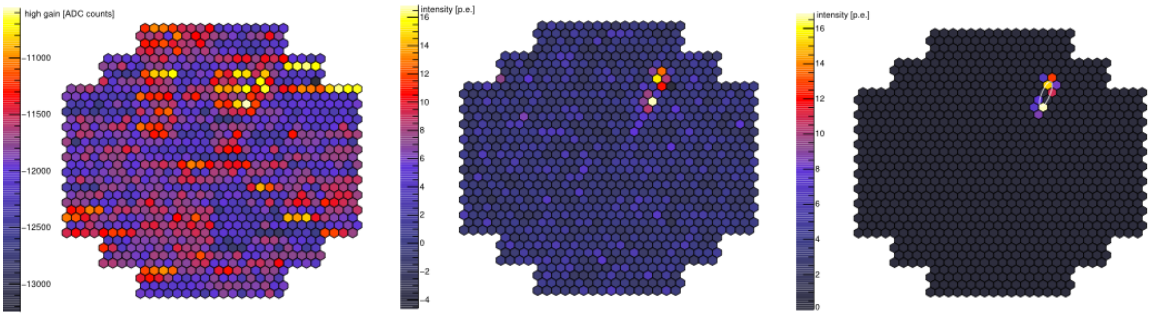

(a) (b) (c)

Figure 3.11: In (a) a camera image with high gain ADC counts is shown, followed by the calibrated image with p.e. counts in (b). Finally the same camera image after applying the "tail-cuts" is presented in (c) (Figures taken from Komin (2006).).

By using the "tail-cuts" the shape of the showers becomes more pronounced. For VHE γ-ray showers the shape is almost elliptical (see Fig. 3.11(c)) and can be characterized by the Hillas parameters (HP) Hillas (1985) (see Fig. 3.12). These parameters are derived as the momenta of the detected light intensity distribution (LID).

In the following a summary of the different HPs is listed. The *size* corresponds to the detected light intensity after applying the "tail-cuts" and the position of the ellipse is defined by the center of gravity of the LID(x, y). The second momenta of the LID describe the major axis and the minor axis and are identified as *length* and *width*. The *distance* d marks the offset between the center of gravity and the camera center. Finally the angle between the major axis and the line defined by the

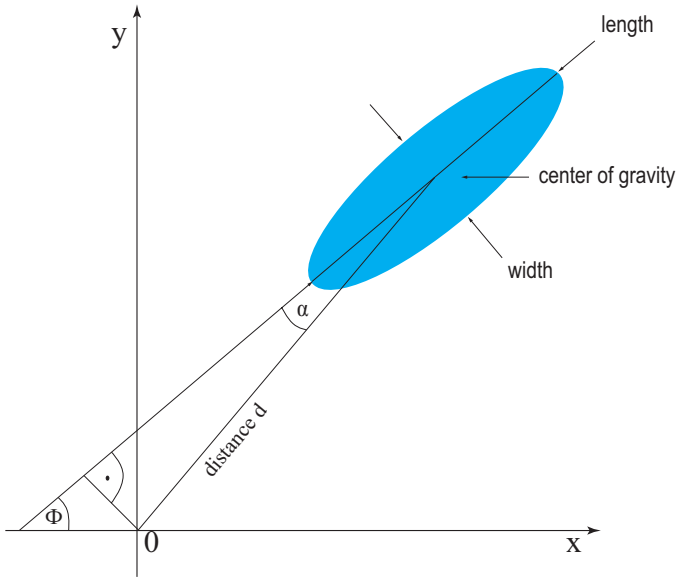

Figure 3.12: Schema of the shower parametrization in the camera.

camera center and the center of gravity is calculated in order to specify the orientation α of the ellipse in the camera image.

Shower Reconstruction

The shower direction reconstruction is performed in the so-called camera coordination system, with the x- and y-axes defining the image plane and the z-axis has the same direction as the optical axis of the telescopes (see Fig. 3.13(a)). In this system, the major axis of the shower image corresponds to the projection of the shower axis. By superimposing the camera images of the different telescopes, the intersection point of the major axes gives the direction of the air shower. If more than two telescopes have detected a signal, the intersections of every combination of the major axes are calculated and the results are averaged. A weighting factor takes into account, that the reconstruction is more accurate for brighter images and a higher length-to-width ratio.

The impact point, i.e. the position where the shower axis hits the ground, is determined in the so-called reference coordinate system. In this case, the x-axis points to the North, the y-axis to the west and the z-axis to the zenith. In this system the intersection of the major axis yields the impact point. The same procedure for averaging is used as for the direction (see Fig. 3.13(b)).

For more details see Aharonian et al. (1997).

Event Selection

Cherenkov telescopes detect γ-ray - and hadronic showers. Hadronic showers are background events which have to be suppressed. By applying cuts on the HPs, the background is reduced and the signal-to-background ratio (SBR) is maximized. Since there is no calibration source available in the VHE range the optimal cuts are determined by MC-simulations. The following cuts are used

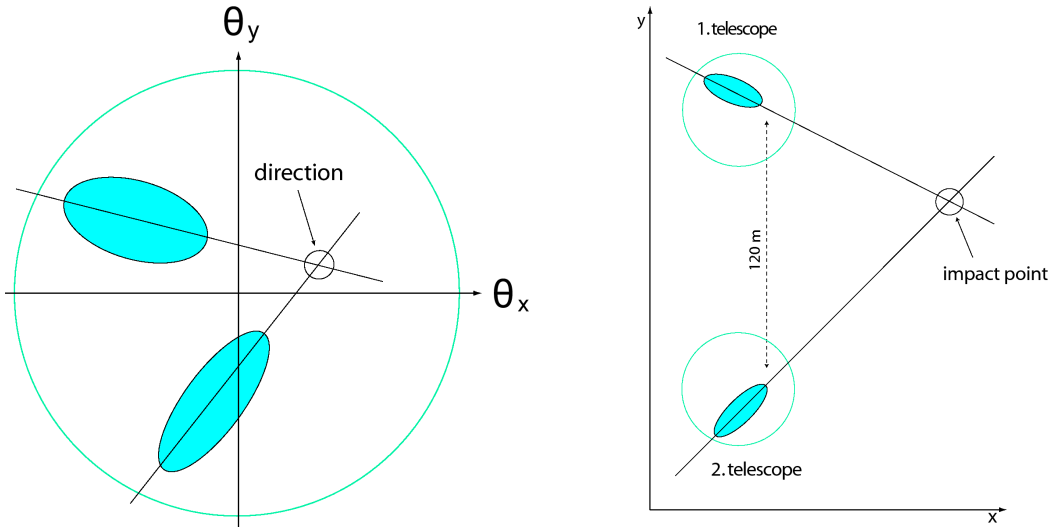

Figure 3.13: In (a) and (b) the principle of reconstructing the shower direction and the shower impact point is illustrated on the basis of two telescopes.

in a standard hillas-analysis.

- Local distance cut
  The local distance is the distance between the camera center and the center of gravity of the image. To avoid truncated images on the border of the camera a maximal cut on the allowed local distance is applied.
- Size cut
  A minimal size cut is applied, to sort out faint images which are not accurate for the reconstruction. This cut also effects the energy threshold – the higher the cut value, the higher the energy threshold of the analysis.
- "mean reduced scaled width" (MRSW) and the "mean reduced scaled length" (MRSL) cut
  These parameters are mainly responsible for the background suppression. The MRSW is computed from the measured *width* and the expected *width* $\langle width$ which was derived from MC simulations. The measured *width* is subtracted from the expected *width* and then normalized to the mean square deviation. This procedure is performed for each individual telescope and the total result is the average over all telescopes. The expected *width* depends on the zenith angle θ_z, the image intensity I and the impact point b. For the MRSL the same routine is applied.

$$MRSW = \frac{1}{N_{\text{Tel.}}} \sum_{i=0}^{N_{\text{Tel.}}} \frac{width_i - \langle width \rangle (I_i, b_i, \theta_z)}{\sigma (I_i, b_i, \theta_z)} \tag{3.8}$$

$$MRSL = \frac{1}{N_{\text{Tel.}}} \sum_{i=0}^{N_{\text{Tel.}}} \frac{length_i - \langle length \rangle (I_i, b_i, \theta_z)}{\sigma (I_i, b_i, \theta_z)} \tag{3.9}$$

The "Hillas moment analysis" uses three different cut configurations which are suited for different conditions: "standard", "hard" and "loose" cuts. For sources with a flux of ≈10 % of the Crab nebula and a photon index of the order of $\Gamma = 2.6$ the standard cuts are used. They are also applied in blind searches for new VHE γ-ray sources. Hard cuts are optimized for sources with a flux of ≈1 %

of the Crab nebula and a photon index of $\Gamma = 2.0$. They cause a higher energy threshold and are also used for morphology studies. Finally the "loose" cuts allow a lower energy threshold and are used for bright sources. In table (3.1) the values of the different cut configurations are listed.

Table 3.1: Cut configurations for the Hillas analysis

Configuration	MRSL		MRSW		θ^2_{cut}	$size$	d
	Min.	Max.	Min.	Max.	Max. (deg.^{2})	Min. (p.e.)	Max. (')
Standard	-2.0	2.0	-2.0	0.9	0.0124	80	2.0
Hard	-2.0	2.0	-2.0	0.7	0.01	200	2.0
Loose	-2.0	2.0	-2.0	1.2	0.04	40	2.0

3.4.3 Model++ Analysis

In the previous Subsection 3.4.2 the Hillas moment analysis was presented. Now the focus is on the Model++ analysis. This analysis is based on the comparison of camera images to a semi-analytical model. It needs more computer power than the Hillas moment parametrization but it provides better results concerning the angular- and energy resolution.

The models for the shower images are computed by the use of Monte-Carlo simulations for different zenith angles, energies and primary interactions t_0. The parameter t_0 describes the point of first interaction of a γ-ray in the atmosphere and is measured in units of the radiation length X_0. Additionally the NSB noise is added to the models for the shower images which makes the image cleaning before the analysis obsolete. The analysis itself reconstructs the shower parameters like energy, direction and first interaction height by fitting the shower model to the shower images. The fit is sensitive to its starting values. Therefore, these values are set to the ones obtained by the Hillas moment analysis.

In Figure 3.14 the model of a VHE γ-ray shower with an energy of 1 TeV is shown for different impact points. The first interaction took place at one radiation length. The sequence illustrates that showers get broader with increasing distance. In Fig. 3.14(d) the same impact point is chosen as in (b) but the shower starting point is at $3\,X_0$. The difference between (b) and (c) is not so pronounced. A detailed description of the model is presented in de Naurois & Rolland (2009).

Event Selection

In the analysis procedure the pixel are classified as belonging either to the shower or to the background. The derived parameters are then the shower goodness (SG) and background goodness (BG). The discrimination between VHE γ-ray showers and hadronic showers is mainly based on the SG. The determination of SG and respectively BG is performed with the goodness-of-fit which is defined as follows:

$$G = \frac{\sum_{\text{pixel } i} \left[\ln L\left(s_i|\mu_i\right) - \langle \ln L \rangle |_{\mu_i} \right]}{\sqrt{2 \times \text{NdF}}} \tag{3.10}$$

It compares the model prediction and the actual shower images and checks if the recorded events are compatible with a pure γ-ray hypothesis. Therefore the actually observed Loglike-

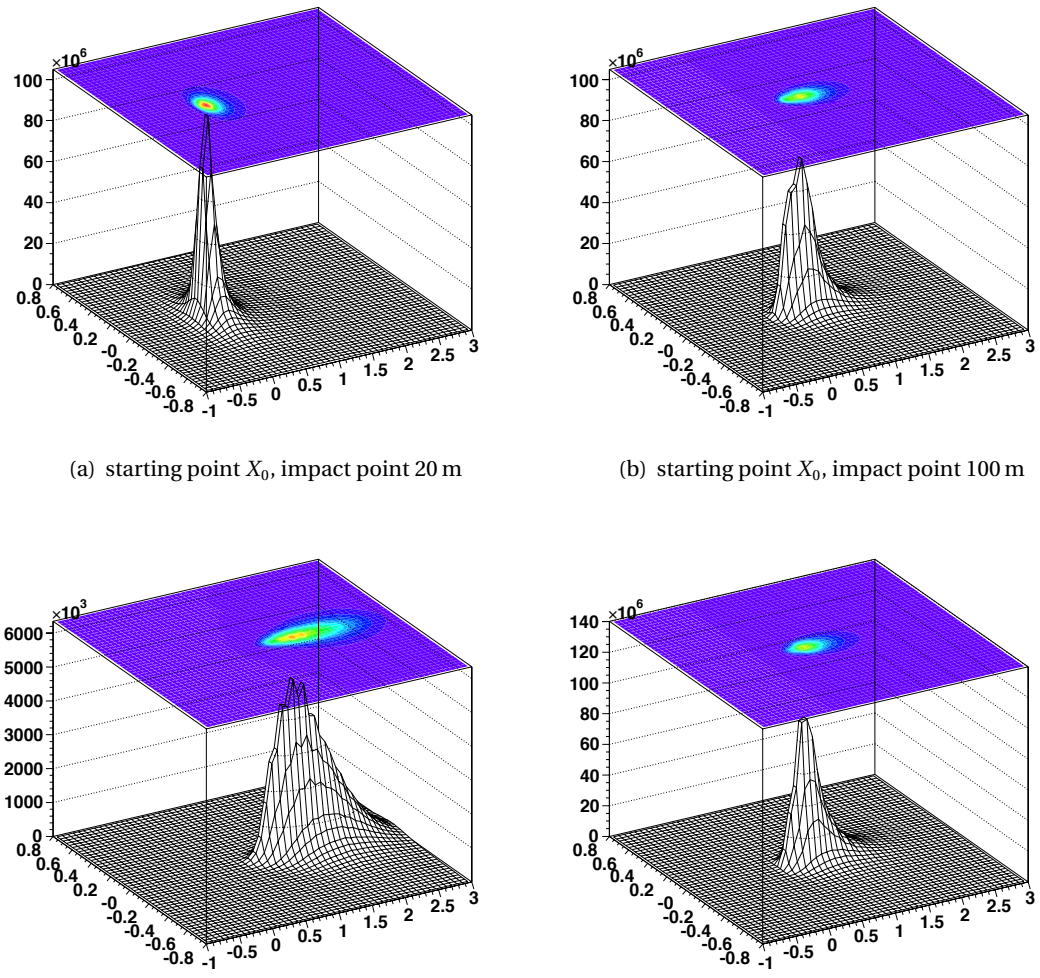

(a) starting point X_0, impact point 20 m

(b) starting point X_0, impact point 100 m

(c) starting point X_0, impact point 250 m

(d) starting point $3\,X_0$, impact point 100 m

Figure 3.14: Model of a 1 TeV shower for different parameters (Figures taken from de Naurois & Rolland (2009)).

lyhood $\ln L\left(s_i|\mu_i\right)$ is compared to the expected value $\langle \ln L\rangle|_{\mu_i}$ for each single pixel. The Likelihood-method quantifies the probability of observing a certain value under the assumption of an expected value. In Equation 3.10 the degrees of freedom Ndf are direction and impact point each with 2 parameters, energy and X_0. Similar to the Hillas analysis a mean reduced scaled value in this case the mean scaled shower goodness (MSSG) is used.

$$MSSG = \frac{1}{N_{\text{Tel.}}} \sum_{i=0}^{N_{\text{Tel.}}} \frac{\text{SG}_i - \langle \text{SG}\rangle_i}{\sigma_i} \tag{3.11}$$

The Model++ analysis has four predefined cut configurations which are used for different purposes: standard, faint, loose and HiRes cuts. The cuts are applied for the same cases as in the Hillas moment analysis (see. Subsection 3.4.2). The HiRes configuration is a new configuration similar to the standard cuts but with an additional cut on the error of the reconstructed direction. This ensures, that only well reconstructed events pass the cuts and the angular resolution of the analysis is enhanced. This is of special interest for the study of the morphology of γ-ray sources. For all configurations the nominal distance is required to be smaller than 2°, at least two telescopes must have triggered and the BG has to be smaller than 2. These values are chosen to avoid badly reconstructed showers. The *size*, *MSSG*, t_0, L_{NSB} are adapted for the different analyses. L_{NSB} is the likelihood value for the comparison of the camera image to pure NSB fluctuations. If L_{NSB} is too high the determination of the correct shower model is not possible anymore. The values of the parameters for the different analyses are listed in Table. 3.2.

Table 3.2: Cut configurations for the Model++ analysis

Configuration	*size* Min. [p.e.]	Nom. Dist. Max. [°]	Tels Min.	MSSG	BG Max.	t_0 [X_0]	L_{NSB} Max.	θ^2_{cut} Max. (deg.^{2})	Dir. Err. Max. [°]
Standard	60	2	2	[-3,0.6]	2	[-1,4]	-1	0.01	—
Faint Source	120	2	2	[-3,0.4]	2	[-1,4]	-1	0.005	—
Loose Cuts	40	2	2	[-2,0.9]	2	—	—	0.0125	—
HiRes Cuts	60	2	2	[-3,0.6]	2	[-1,4]	-1	0.01	0.03

3.4.4 Background Estimation and Spectrum

The subsection starts with the determination of the energy and angular resolution which is then followed by the signal extraction and the spectrum determination.

Energy Reconstruction and Energy Resolution

After the shower reconstruction the energy reconstruction is performed. The energy of a shower depends on the *size*, the zenith angle and the impact point. At this very high energies no calibration sources are available, therefore extended simulations are used. The energy is tabulated dependent on these parameters and stored in so-called “look-up tables”.

The reconstructed energy E_{reco} is determined as follows: The true energy E_{true} for each telescope is taken from the table according to the measured *size*, zenith angle and impact point. Afterward the average over all telescopes is calculated:

$$E_{\mathrm{reco}} = \frac{1}{N_{\mathrm{tel}}} \sum_{i=0}^{N_{\mathrm{tel}}} E_{\mathrm{true}}(I_i, b_i) \tag{3.12}$$

The energy resolution is also tabulated in "look-up tables' and was calculated as the RMS of the differences between the reconstructed E_{reco} and the true energy E_{true} divided by the true energy E_{true} by using MC simulations.

$$\frac{\Delta E}{E} = \frac{E_{\mathrm{reco}} - E_{\mathrm{true}}}{E_{\mathrm{true}}} \tag{3.13}$$

In Fig. 3.15 the energy resolution as a function of the true energy is given for simulated γ-ray showers after the cuts have been applied to the data. The resolution is smaller than ≈15 % for the whole energy range. Furthermore the plot shows that the Model++ Std analysis has a better energy resolution in comparison to the two Hillas moment analysis with *size*-cuts of 60 p.e. and 120 p.e.. The systematic energy bias is better than 10% for energies higher than 500 GeV for both analyses and improved for the Model++ Std analysis.

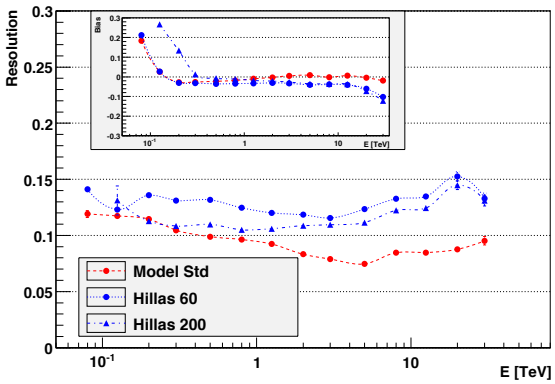

Figure 3.15: Energy resolution and bias (inset) for a fixed zenith angle. Red: Model Std (Model++ Std), Blue: Hillas with *size*-cut of 60 and 120 p.e.. The Model++ Std analysis has a better energy resolution and energy bias in comparison to the Hillas moment analysis (Figure taken from de Naurois & Rolland (2009)).

Point Spread Function

All the detected events in an observed sky region which have passed the cuts are plotted in two-dimensional images, the so-called "sky maps". In astronomy two typical coordinate system are used. The first one uses right ascension *RA* on the x-axis and declination *Deg* on the y-axis and is based on the coordinates of the Earth. The second one uses Galactic coordinates with the Galactic longitude l on the x-axis and the Galactic latitude b on the y-axis. In this system the galactic center is the reference point.
Under the assumption of an ideal experiment a point source in the sky would be pinpointed directly to one point. In reality, broadening effects smooth the signal over more pixels or in other words there exist only a probability that an event detected at a certain position really comes from that direction. The characteristics of these uncertainties are described by the point spread function (PSF). These imperfectness results from the accuracy of the tracking and optical system of the telescopes as well as the reconstruction of the impact point and direction. To sum-up the PSF

defines the angular resolution and therefore the smallest possible separable structure and also the accuracy for the detection of the position of a point source.

The PSF for H.E.S.S. was determined by shower simulations for point sources. In Figure 3.16 the angular resolution (68 % containment radius) is plotted (a) as a function of the energy at a fixed zenith angle and (b) as a function of the zenith angle at a fixed energy. It is clearly visible that the Model++ analysis has a much better resolution than the Hillas moment analysis. The angular resolution decreases for high zenith angle and small energies since the reconstruction of the shower is more inaccurate.

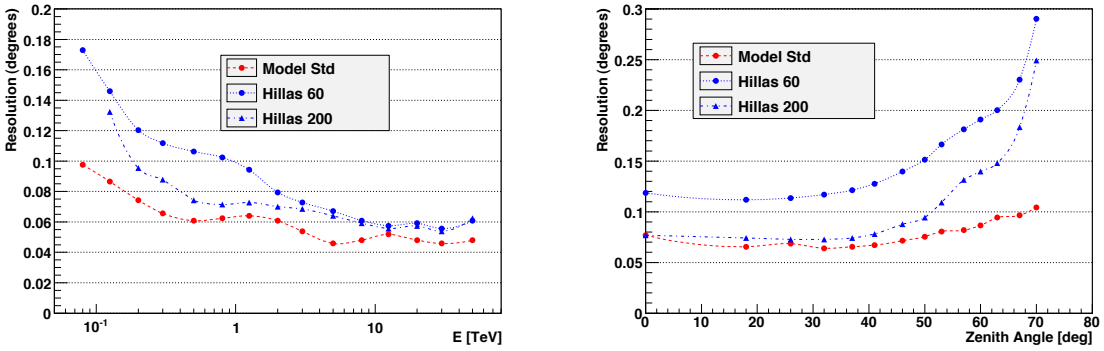

(a) fixed zenith angle

(b) fixed energy

Figure 3.16: (a) Angular resolution (68 % containment radius) as a function of the energy at a fixed zenith angle. (b) Angular resolution (68 % containment radius) as a function of the zenith angle at a fixed energy. The angular resolution decreases for high zenith angle since the reconstruction of the shower is more inaccurate. (Figures taken from de Naurois & Rolland (2009).)

As a cross-check of the simulation the detected events of a strong point source – the blazar PKS 2155 − 304 – are plotted as a function of "θ^2" (see Figure 3.17). θ^2 is the quadratic angular distance between the source position and the reconstructed direction of the source. Because of the radial dependence of the PSF, a double Gaussian function can describe the data very well. The function is given in the following.

$$PSF = A_1 \left(\exp\left(\frac{-\Theta^2}{2\sigma_1^2} \right) + A_2 \exp\left(\frac{-\Theta^2}{2\sigma_2^2} \right) \right) \tag{3.14}$$

σ_1 is mainly responsible for the PSF and σ_2 is only a small correction. σ_1 is in the order of 0.1° for the Hillas analysis and 0.06° for the Model++ analysis. This study also confirms the better angular resolution of the Model++ analysis in comparison to the Hillas moment analysis on real data.

Since the HiRes configuration, which uses an additional cut on the error of the direction, helps to improve the angular resolution even more. In Fig. 3.18 the angular resolution is shown as a function of energy in (a) and the θ^2 plot for the blazar PKS 2155 − 304 in which the 68 % containment radius and the 95 % containment radius are overlaid in blue and red for the HiRes analysis in (b). More information about the PSF is provided in Hofmann et al. (1999) and de Naurois & Rolland (2009).

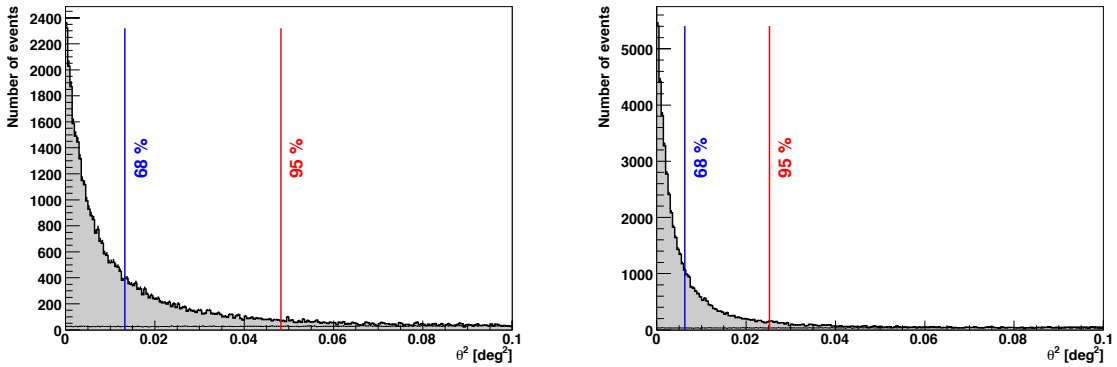

(a) Hillas 60 p.e. cut (b) Model++ Std

Figure 3.17: Histogram of the squared angular distance θ^2 for the blazar PKS 2155 − 304 in which the 68 % containment radius and the 95 % containment radius are included in blue and red. (Figures taken from de Naurois & Rolland (2009))

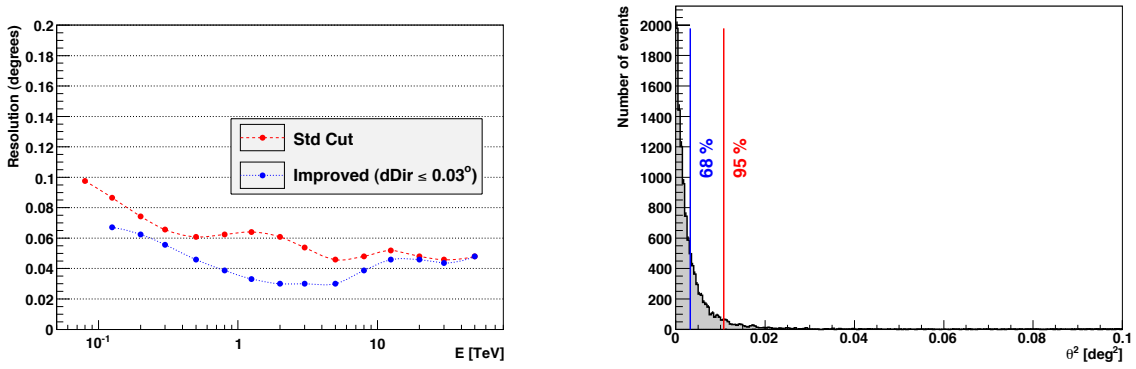

(a) (b)

Figure 3.18: (a) Angular resolution (68 % containment radius) as a function of the energy at a fixed zenith angle. Std cuts are compared with HiRes cuts which involve the error on the reconstruction of the direction as a cut parameter. (b) Histogram of the squared angular distance θ^2 for the blazar PKS 2155 − 304 in which the 68 % containment radius and the 95 % containment radius for the HiRes analysis are overlaid in blue and red. (Figures taken from de Naurois & Rolland (2009).)

Signal Extraction and Background Estimation

The event selection strategies described for the Hillas moment- and the Model++ analysis in Subsection 3.4.2 and Subsection 3.4.3 respectively, reduce the background by a factor of ∼100 , which leads to a SBR of 1:1. The remaining background consists of hadronic events and a randomly distributed component of diffuse VHE γ-rays, which are generated for example in interstellar gas. This background is assessed with different background models. The goal is to determine the events above the background, that belongs only to the γ-ray signal, the so-called γ-excess events N_{excess}. These excess events can be determined by subtracting from the number of events in the predefined source region N_{on} the number of events N_{off} that belong to a background (or off) region:

$$N_{\text{excess}} = N_{\text{on}} - \alpha N_{\text{off}}. \tag{3.15}$$

the normalization factor α describes the differences in the observations and in the used areas of N_{on} and N_{off} in solid angle, lifetime, zenith angle and system acceptance A^{γ}:

$$\alpha = \frac{\int_{\text{on}} A^{\gamma}_{\text{on}}\left(\theta_x, \theta_y, \theta_z, t\right) \mathrm{d}\theta_x \mathrm{d}\theta_y \mathrm{d}\theta_z \mathrm{d}t}{\int_{\text{off}} A^{\gamma}_{\text{off}}\left(\theta_x, \theta_y, \theta_z, t\right) \mathrm{d}\theta_x \mathrm{d}\theta_y \mathrm{d}\theta_z \mathrm{d}t} \tag{3.16}$$

The system acceptance A^{γ} represents the probability to detect a γ-ray-event. Because of the radial symmetry relative to the camera center the acceptance can be plotted in a 1D-histogram. In Figure 3.19 it is given for different zenith angles and Hillas cut configurations.

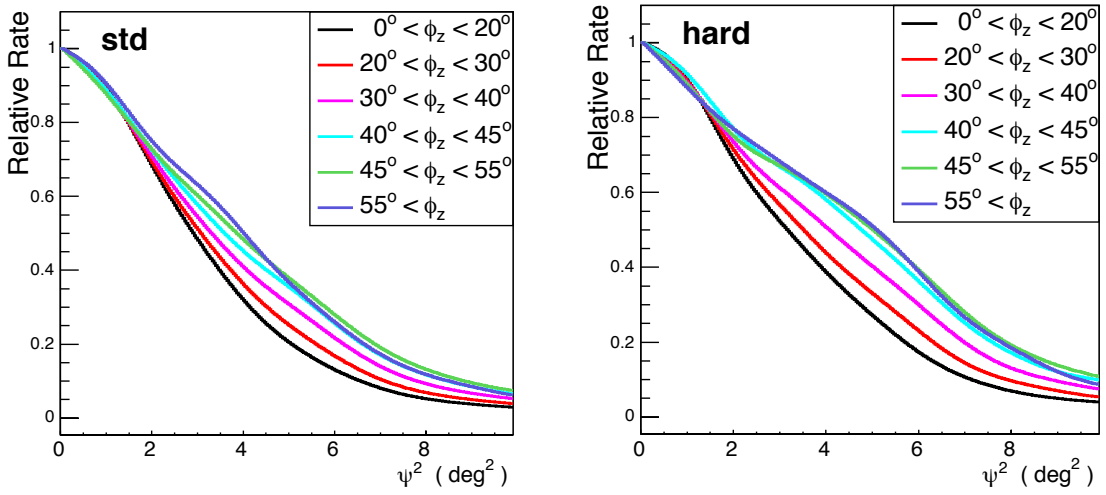

(a) Hillas “std-cuts”

(b) Hillas “hard-cuts”

Figure 3.19: The plot shows the radial acceptance obtained for different zenith angles and Hillas cuts (Figure taken from Berge et al. (2007)).

The statistical significance of the excess is calculated with the maximum likelihood method presented in Li & Ma (1983). With equation 3.17 the null hypothesis is tested, if all event belong to the background. H.E.S.S claims a detection of a source if the significance is $\geq 5\,\sigma$.

$$S = \sqrt{2}\left\{ N_{\text{on}} \ln\left[\frac{1+\alpha}{\alpha}\left(\frac{N_{\text{on}}}{N_{\text{on}}+N_{\text{off}}}\right)\right] + N_{\text{off}} \ln\left[(1+\alpha)\left(\frac{N_{\text{off}}}{N_{\text{on}}+N_{\text{off}}}\right)\right]\right\}^{1/2} \tag{3.17}$$

For the signal extraction an estimate for the background is needed. Therefore different background methods are applicable. One possibility is to take advantage of the "wobble mode" observations normally used by H.E.S.S.. In this case the telescopes do not point to the observed source position but to a position with an offset of 0.5° to 1.5°. This allows to estimate the background from the same field of view. Due to the limited FoV the method can be applied to point sources and moderately extended sources. For highly extended sources the background is estimated with additional "off-runs" which are observation runs pointing to regions without sources but with nearly the same observation conditions. The drawback of the second method is, that the observation time is doubled.

In the following the background models – ring, region and reflected background – used in this thesis are presented. For the morphology studies the ring and the region background models are used. The latter is suited for extended sources, whereas the ring background model is only usable for point or moderate extended sources. The reflected background model is applicable for the spectrum determination. An overview of all background models used by H.E.S.S. is presented in Berge et al. (2007).

Ring Background Model The ring background model calculates the excess event in the whole FoV. Therefore all events passing the cuts and which lie inside a radius of $\theta \approx 0.1°$ around a test position are counted as on events N_{on}. The estimation of the number of off events N_{off} is performed by adding up all events after cuts which lie inside a ring around the same test position with a median radius of 0.5° and an area of ≈ 7 times larger than the on region. To take into account areas with γ-ray sources, exclusion regions are defined. This regions are excluded from the calculation of the N_{off}. The α value for the normalization of the on- to the off-region is determined by adding up the corresponding acceptances. Finally the excess at the test position is calculated according to equation 3.15. A schematic of the ring-background model is shown in Fig. 3.20.

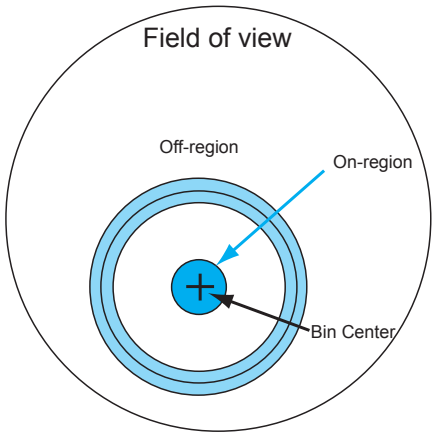

Figure 3.20: Schematic of the ring background model. The on events N_{on} are in the circle around the bin center and the off events N_{off} are from a ring with a median radius of 0.5°.

Region Background Model In contrast to the ring background model the region background model is based on the fact that the background is evenly distributed in the camera FoV and that the background resembles the acceptance of the camera. The maximal acceptance of the camera is normalized to one. The acceptance gives the probability of an off event at a certain position

($N_{\text{Acc.}}(x,y)$). Consequently the acceptance map can be used as an estimation for the background. Therefore the excess in each bin of the excess map is calculated as follows:

$$N_{\text{excess}}(x,y) = N_{\text{event}}(x,y) - \alpha N_{\text{Acc.}}(x,y). \tag{3.18}$$

with α:

$$\alpha = \frac{\sum_{i}^{N} N_{\text{event}}(i)}{\sum_{i}^{N} N_{\text{Acc.}}(i)} \tag{3.19}$$

and the counts in a bin of the event map $N_{\text{event}}(i)$ and the corresponding counts in the acceptance map $N_{\text{Acc.}}(i)$. For the determination of α only the counts are used which are not associated to γ-ray signals and N is the number of bins which are used for the calculation. The region with γ-ray sources, so-called exclusion regions are taken into account in the calculation.

In Fig. 3.21 a slice in the direction of right ascension through the event map of a source with a ring-like structure is shown. The background follows nicely the acceptance map scaled with the factor α (red line). In the source region more events accumulate. The blue line indicate the acceptance map without the scaling.

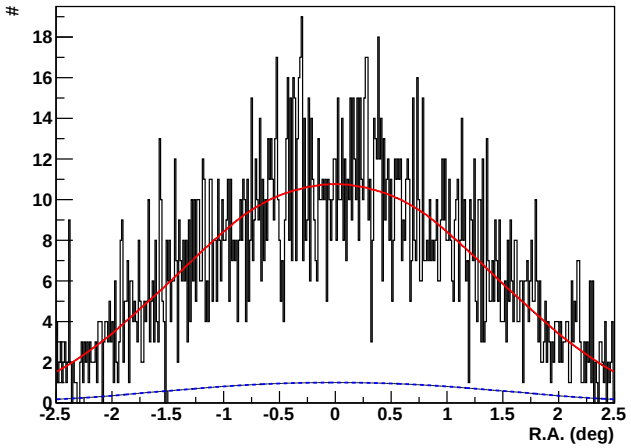

Figure 3.21: Slice in the direction of right ascension through the event map of a source with a ring-like structure. The background follows nicely the acceptance map scaled with the factor α (red line) and in the region of source more events accumulate. The blue line indicate the acceptance map without the scaling.

Reflected Background Model Both the ring background model and the region background model are not suited for the spectrum determination. The acceptance in the off regions varies which leads to uncertainties. To overcome this the reflected background model is used for the estimation since no acceptance correction is needed for the excess calculation (see Fig. 3.22). This is based on the fact that the off regions have the same size, shape and distance to the pointing position as the on region. The multiplicity of the off regions improves the accuracy in the background estimation and the independence of the acceptance correction makes this background model ideal for the spectrum estimation. The excess is calculated with Equation 3.15.

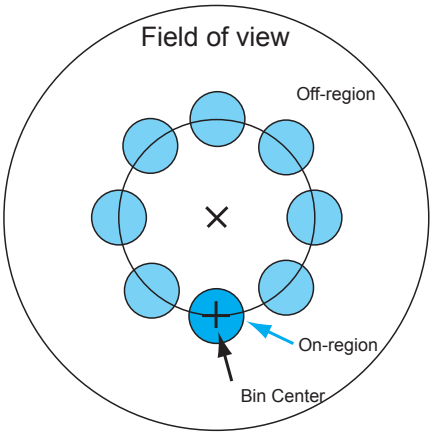

Figure 3.22: Schema of the reflected background model. The on events are in the circle around the bin center and the off events are from the circles with the same distance to the pointing position like the on position.

Effective Areas and Spectrum

To derive a spectrum the effective area A_{eff} of the H.E.S.S. experiment has to be known. The A_{eff} depends on the zenith angle and offset of the source position to the pointing direction, on the energy and on the applied cuts. It represents the detection efficiency of the experiment.

$$A_{\text{eff}} = A_{\text{sim}} \times \frac{N_{\text{sel}}}{N_{\text{sim}}} \tag{3.20}$$

The A_{eff} is determined by Monte Carlo simulations by calculating the fraction of the events passing all cuts (N_{sel}) to all simulated events (N_{sim}) times the area of the impact points of the events. The A_{eff} is tabulated in look-up tables dependent on the source position (northern or southern) and the optical efficiency which takes the aging effects of the system into account. In Figure 3.23 the A_{eff} is given in dependency of the different cut configurations. Their A_{eff} is lower than the value expected for only triggered events and the resulting A_{eff} is nearly the same for all the different analyses. The decline of the A_{eff} at high energies in the Model++ analysis can be explained by the fact that the shower models are only determined up to 20 TeV and at higher energies only an extrapolations of the model is used.

The differential spectrum $\frac{\mathrm{d}N}{\mathrm{d}E}$ of a source is defined as follows:

$$\frac{\mathrm{d}N}{\mathrm{d}E} = \frac{1}{A_{\text{eff}}(E) \times t_{\text{live}}} \frac{\mathrm{d}N_\gamma}{\mathrm{d}E} \tag{3.21}$$

Thereby A_{eff} is the effective area, $\frac{\mathrm{d}N_\gamma}{\mathrm{d}E}$ are the counts per energy interval and t_{live} is the observation time (often called live time). The integrated flux can be calculated as the integral over the energy above a certain energy threshold.

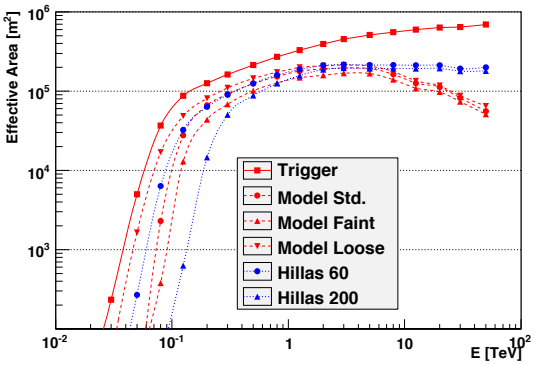

Figure 3.23: Comparison of the effective areas of the different cut configurations. The achieved A_{eff} is lower than the value expected for the triggered events and the resulting A_{eff} is nearly the same for all of the different analyses. (Figure taken from de Naurois & Rolland (2009)).

4 Analysis of the H.E.S.S. data set of RCW 86

In the previous chapter the basic knowledge of the understanding of the VHE γ-ray analysis was discussed and is applied in this chapter to the supernova remnant RCW 86. As already mentioned in Chapter 2 the detection of RCW 86 was confirmed in the first H.E.S.S publication (Aharonian et al. 2009). The unveiling of its potential shell-like structure in the VHE γ-ray data is a still open question.
Since this first publication the data set increased and a more sensitive data analysis technique, the so-called Model++ analysis (see Section 3.4.3), has been developed. This allows to study RCW 86 with higher precision.

In this chapter the H.E.S.S. data set is specified, then the energy spectrum and the morphology are presented. In the end a correlation study between X-ray and the VHE γ-ray data of RCW 86 is performed.

The results of this chapter are parts of a publication which is currently in preparation (H.E.S.S. Collaboration et al. (2012)).

4.1 Data Set and Analysis Configuration

The discovery of RCW 86 was announced by the H.E.S.S. collaboration using 71 observation runs taken between 2004 and 2007 (Aharonian et al. 2009). The observations had been performed in wobble mode with a mean offset of 0.7° to allow background subtraction from the same field of view. The zenith angles lied between 38° and 53° with a mean zenith angle of 41°. This translates directly into an energy threshold of 480 GeV. For the analysis, only runs passing certain selection criteria, e.g. on the number of triggered telescope and on the atmospheric condition, were used comprising a total live time of 31 hours. Further details on the run selection criteria are given in (Aharonian et al. 2006a). In the following this data set is labeled as “published".

The new data set used in the analysis presented here comprised a total of 136 observation runs (live time of 56.2 hours). Between 2007 and 2010 observations on the source HESS J1507 − 622 which is in close vicinity of RCW 86 and the Galactic Plane scan further increased the sample, as well as dedicated runs on RCW 86 in 2011. Unfortunately in the summer of 2011 only ∼5% of the total observation time could be used for analysis due to bad weather. Therefore only 39.6 hours remained after quality selection. The zenith angles coverage of the data set is between 38° and 53° with a mean of 40°. This leads to the same energy threshold of 480 GeV as for the published data. The new data set has a mean offset of 1.1°. The different data sets used in the analysis are summarized in Table 4.1.

For the analysis the following quality selection criteria have been imposed on the data:

- At least three telescopes have to participate in the observation run to ensure a good angular- and energy resolution and γ-hadron separation.

Table 4.1: List of the data sets used in the analysis of the H.E.S.S. data on RCW 86

Data set	Number of runs	Live time [h]	Zenith angle mean	Offset angle mean	Energy threshold [GeV]
Published (2009)	71	31	41°	0.7°	480
New	136	39.6	40.45°	1.1°	480

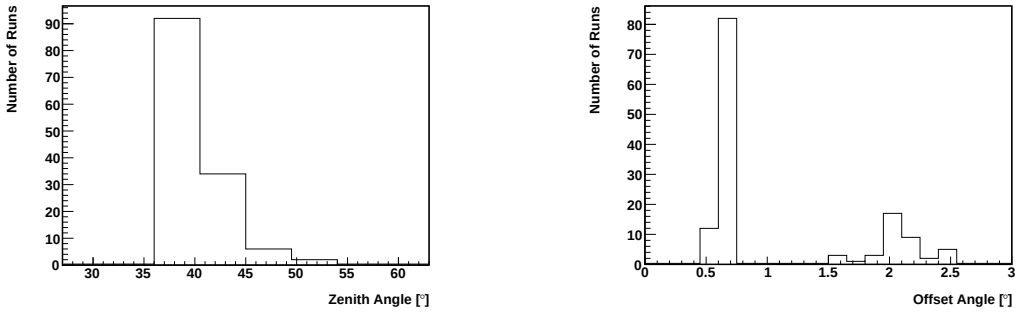

(a) zenith angle distribution

(b) off axis distribution

Figure 4.1: For the new data set of RCW 86 (see Table 4.1) (a) the zenith angle distribution and (b) the offset angle distribution are shown.

- The zenith angle-corrected system trigger rate has to lie between 100 and 500 Hz. Otherwise the atmosphere is characterized as hazy and the observation are excluded from the analysis.
- Fluctuations of the system trigger rate have to be less than 4%. This allows to reject runs where clouds moved into the field of view.
- The run duration has to be longer than 10 minutes, i.e. runs that encounter problems are rejected. These runs are usually stopped either manually by the shift crew or automatically by the data-acquisition system.
- The number of broken pixels is required to be smaller than 10% of the total pixel number of 960. This rejects runs with too high uncertainties in the energy and direction reconstruction due to technical problems.

The criteria are also presented in detail in (Aharonian et al. 2006a):

Analysis Configurations

In the H.E.S.S. publication of RCW 86 the results of a Hillas momentum analysis (see Sec. 3.4.2) with Std cuts (see Tab. 3.1) is presented. The source region was chosen to be circular with a radius of 0.45° corresponding to the size in X-rays of the ROSAT mission (Bocchino et al. 2000) taking the PSF of the VHE γ-ray analysis into account.

The analysis presented here is performed with the Model++ analysis (see Sec. 3.4.3). The source region was chosen accordingly which accounts for 0.41° due to the better angular resolution. In the following a comparison of the published results and the Model++ analysis with different configurations of the analysis cuts is presented: Std, Faint and Enhanced (Faint + HiRes). The Enhanced cuts are the combination of the Faint and the HiRes cuts. The cut on the minimal energy

and on the directional error ensures an improved resolution and therefore excellent reconstructed events. In Table 4.2 the number of excess events and the source significances are collected. The Modell++ analysis has a higher significance of 14.9σ to 17.9σ depending on the cut configuration. As expected the Enhanced configuration shows the highest significance.

Table 4.2: Results of the analysis of RCW 86. Given are the published values as well as the one of the Model++ analyses with different cut configurations. The Enhanced cut configuration is the combination of Faint cuts with the HiRes cuts.

Data set	Analysis	Configuration	θ^2_{cut} / [deg^2]	Excess Events	Significance
Published	Hillas	Std	0.2025	1546	8.5σ
New	Model++	Std	0.1681	1568.3	14.9σ
New	Model++	Faint	0.1681	1433.3	17.6σ
New	Model++	Enhanced	0.1681	1452.9	17.9σ

As proof, that the whole SNR lies within 0.41°, the squared radial distance between the reconstructed and the actual source position is given in Fig. 4.2. The distribution nicely shows, that the chosen source size is a good assumption.

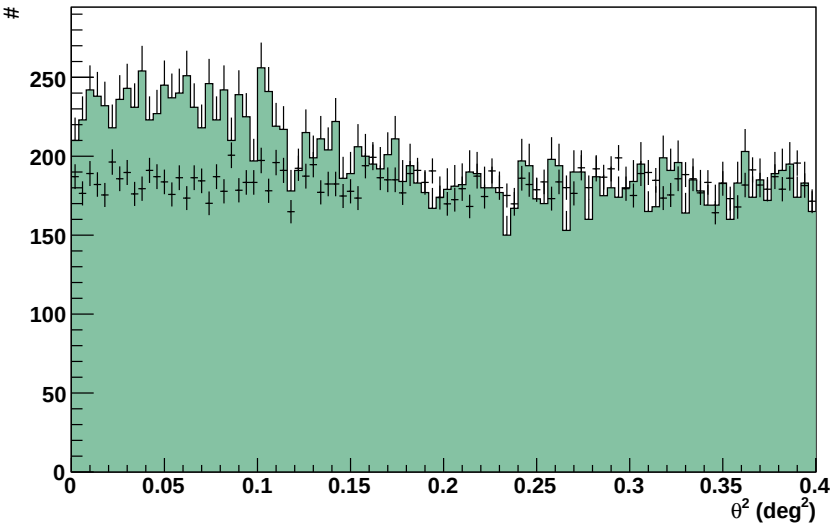

Figure 4.2: Plot of the θ^2 distribution of RCW 86 with the Model++ analysis and Std cuts. The filled area represents the events from the source region and the black data points the background events. It is visible that the events from the source region dominate in the chosen θ^2 of 0.1681 deg^2 over the background events.

The acceptance-corrected excess maps are given in Fig. 4.3(a) and 4.3(b). The Enhanced cut configuration was chosen due to its superior angular resolution. In Fig. 4.3(b) smoothing was done with a Gaussian function of width $\sigma_{\text{smooth}} = 0.05°$ which represents the 68% containment radius of the PSF. The overlaid white contours represent the 3, 4 and 5σ significance levels. The comparison of the morphology between the published excess map and the new one is presented in Sec. 4.3.

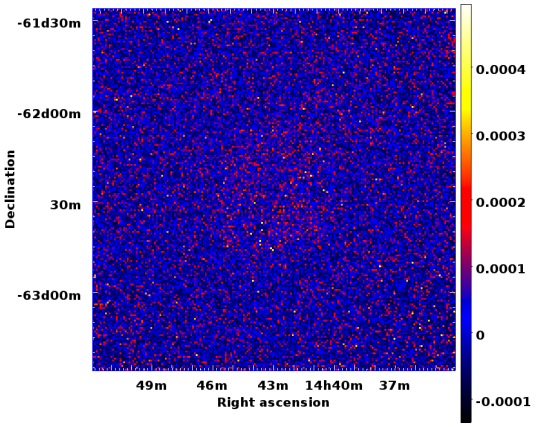

(a) Unsmoothed acceptance-corrected excess map, new data, Model++ Enhanced, this work

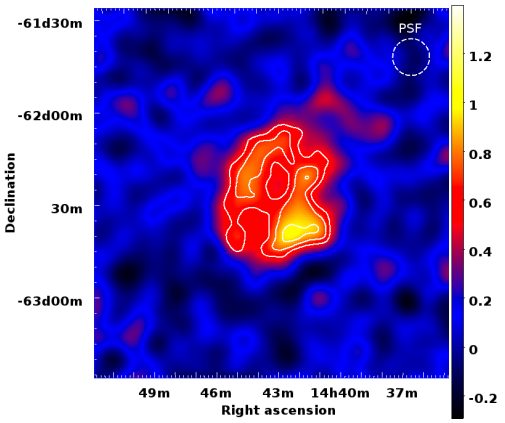

(b) Acceptance-corrected excess map smoothed with a Gaussian function with a width of $\sigma_{\text{smooth}} = 0.05°$, new data, Model++ Enhanced, this work

Figure 4.3: In Fig. (a) and (b) the acceptance-corrected excess map of the new data of RCW 86 is displayed and the data are based on a Model++ Enhanced analysis. In Fig. (a) there is no smoothing applied. In Fig. (b) the data are smoothed with a Gaussian function with a width of $\sigma_{\text{smooth}} = 0.05°$. This width is chosen since it represents the 68% containment radius of the PSF for this analysis. The PSF for this analysis and smoothing is shown in the upper right corner. It is also overlaid with the white contours of the 3,4 and 5σ significance levels.

4.2 Spectral Analysis

After the presentation of the data set the focus lies now on the spectral analysis of RCW 86. For the determination of the spectrum the reflected background model (also called multiple-off background model) is used which is presented in Sec. 3.4.4.

The spectrum is determined with the forward-folding technique. It is based on a binned log-likelihood fit of the spectral shape to the distribution of the reconstructed energies of the events taking the Poisson-distributed nature of the data into account.
The expected number of excess events in a reconstructed energy bin with lower and upper boundaries $\tilde{E}_1$ and $\tilde{E}_2$ and given a true energy E is calculated as follows (de Naurois 2011):

$$n_\gamma = \int_{\tilde{E}_1}^{\tilde{E}_2} d\tilde{E} \int_0^\infty dE \times \Phi(E) \times A_{\text{eff}}(E,\theta,\delta) \times \text{PDF}(E,\tilde{E}) \tag{4.1}$$

The effective area of the system $A_{\text{eff}}(E,\theta,\delta)$ is calculated by simulations depending on the true energy E, the zenith angle θ and the off-axis angle δ. The energy probability density function $\text{PDF}(E,\tilde{E})$ represents the probability of observing a certain reconstructed energy for a given true energy. The dependencies of the PDF on the true energy E, the zenith angle θ and the off-axis angle δ are also taken into account. The source flux $\Phi(E)$ depends on the shape of the spectrum model. With a log-likelihood ($L = \log(P)$) comparison the difference between the observed and the expected number of events in each energy bin is quantified. The probability P of observing N_{on} events and N_{off} events under the assumption of n_γ γ-events and n_{h} hadron-events is calculated with the following formula for Poisson statistics:

$$P(N_{\text{ON}}, N_{\text{OFF}} | n_\gamma, n_{\text{h}}) = \frac{\left(n_\gamma + \beta\, n_{\text{h}}\right)^{N_{\text{ON}}}}{N_{\text{ON}}!} e^{-(n_\gamma + \beta\, n_{\text{h}})} \times \frac{{n_{\text{h}}}^{N_{\text{OFF}}}}{N_{\text{OFF}}!} e^{-n_{\text{h}}} \tag{4.2}$$

In Eq. 4.2 the live-time normalization $\beta = \frac{T_{\mathrm{On}}}{T_{\mathrm{Off}}}$ is the ratio of the live time of the on data-set T_{On} to the off data-set T_{Off}. Since n_h is not a parameter of the spectral shapes it is calculated from the observed n_γ. The best background estimate is given by the value of n_h which maximizes the log-likelihood $L = \log(P)$ for a given n_γ.

The fit procedure is based on the Levenberg-Marquardt algorithm, which is very time efficient for the maximization of the log-likelihood (L = log(P)). The covariance matrix is calculated and it is therewith possible to construct confidence regions for the different spectral parameters.

In the next sections the following spectral shapes are used:

- Power law (PL):

$$\frac{\mathrm{d}N}{\mathrm{d}E} = \Phi_0 \left(\frac{E}{E_0}\right)^{-\Gamma} \tag{4.3}$$

- Curved power law (CPL):

$$\frac{\mathrm{d}N}{\mathrm{d}E} = \Phi_0 \left(\frac{E}{E_0}\right)^{-\Gamma-\beta\log(E/E_0)} \tag{4.4}$$

- Exponential cut-off power law (ECPL):

$$\frac{\mathrm{d}N}{\mathrm{d}E} = \Phi_0 \left(\frac{E}{E_0}\right)^{-\Gamma} \times \exp\left(\frac{-E}{E_C}\right) \tag{4.5}$$

- Broken power law (BPL):

$$\frac{\mathrm{d}N}{\mathrm{d}E} = \Phi_0 \times \begin{cases} \left(\frac{E}{E_0}\right)^{-\Gamma} & \text{for} \quad E \leq E_{\mathrm{B}}, \\ \left(\frac{E_{\mathrm{B}}}{E_0}\right)^{-\Gamma_1+\Gamma_2} \left(\frac{E}{E_0}\right)^{-\Gamma_2} & \text{for} \quad E \geq E_{\mathrm{B}} \end{cases} \tag{4.6}$$

The energy E_0 is the reference energy which is used for the calculation of the spectral parameters. In the following the 1σ confidence interval is given and data points are shown, if the significance in an energy bin is larger than 3σ. The results for the different spectral shapes and regions for the published and new data are listed in Tab. 4.3 and discussed in the following section.

4.2.1 Spectrum of the whole Supernova Remnant

The spectrum extracted from the whole source region is given in Fig. 4.4. A fit of a pure power law was performed within an energy range of 0.48 TeV - 125 TeV. It results in a spectral index of 2.404 ± 0.08. This is in good agreement with the published value of 2.54 ± 0.12 (see Fig. 4.4).

In the publication it was not possible to distinguish if the pure power law or the exponential cut-off power law for the description of the data is preferred. For the new data set the curved-, the exponential cut-off- and the broken power-law are clearly preferred over the pure power law fit. According to the F-Test[1] the exponential cut-off power law is preferred over the pure power law with 4.4σ. This is the spectral shape with the highest significance. The fit parameters are: an index of 1.50 ± 0.28, a cut-off energy of $E_C = (2.69 \pm 0.99)$TeV and an integral flux above 1 TeV of $(6.51 \pm 2.69) \cdot 10^{-12}\mathrm{cm}^{-2}\mathrm{s}^{-1}$. The curved power law and the broken power-law describe the data better as the pure power law with a significance of 3.6σ and 2.7σ. In Fig. 4.5 the results of the spectral fits are given and the resulting parameters are summarized in Table 4.3.

[1] Comparison of statistical models that are fit to a data set, to identify the model that describes the data the best taking the degrees of freedom into account. http://www.graphpad.com/manuals/prism4/RegressionBook.pdf

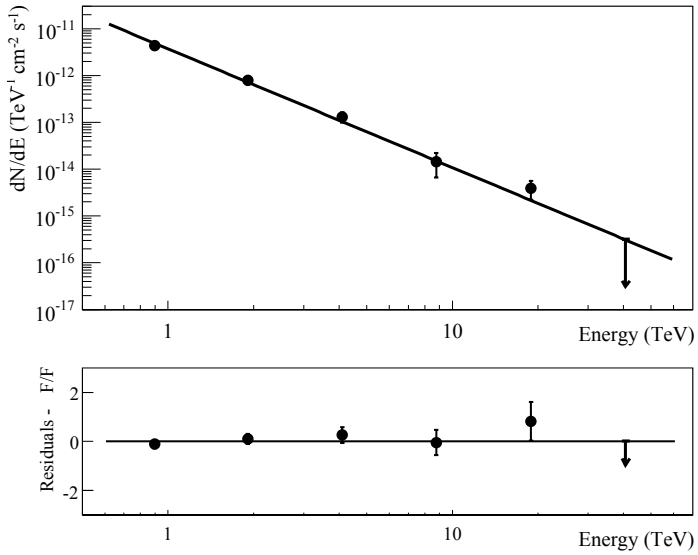

(a) published data: power-law fit

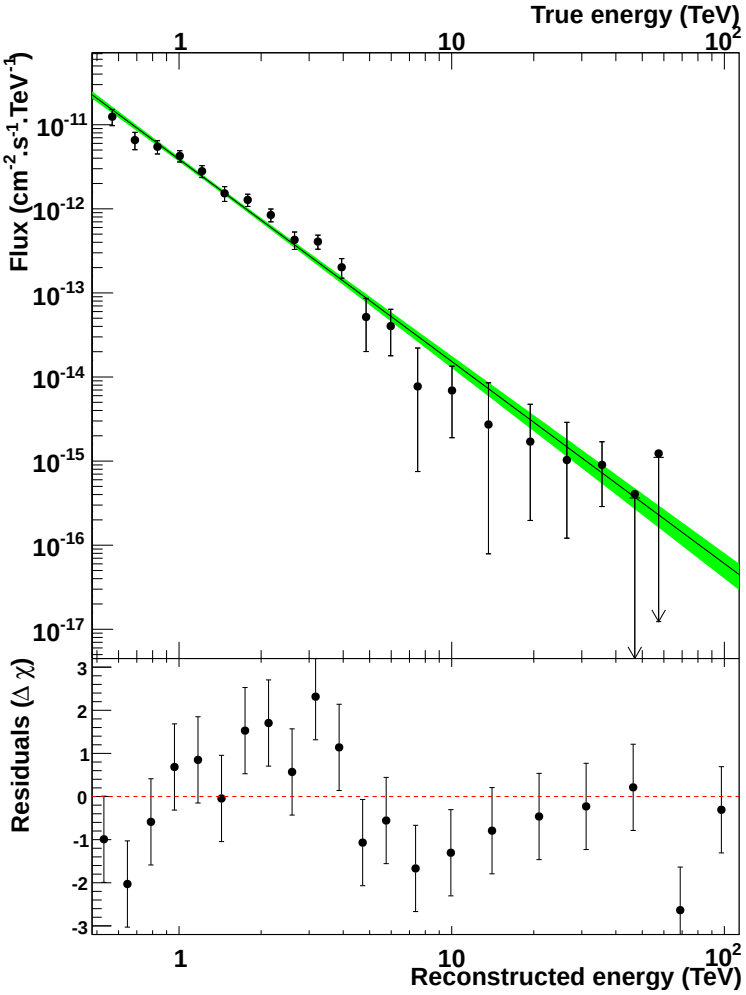

(b) new data: power-law fit

Figure 4.4: The energy spectrum of RCW 86 fitted with a power law for the published (a) and new (b) data set. In (b) the 1σ confidence interval is shown in green and the lower panel displays the residuals of the fit with the power-law.

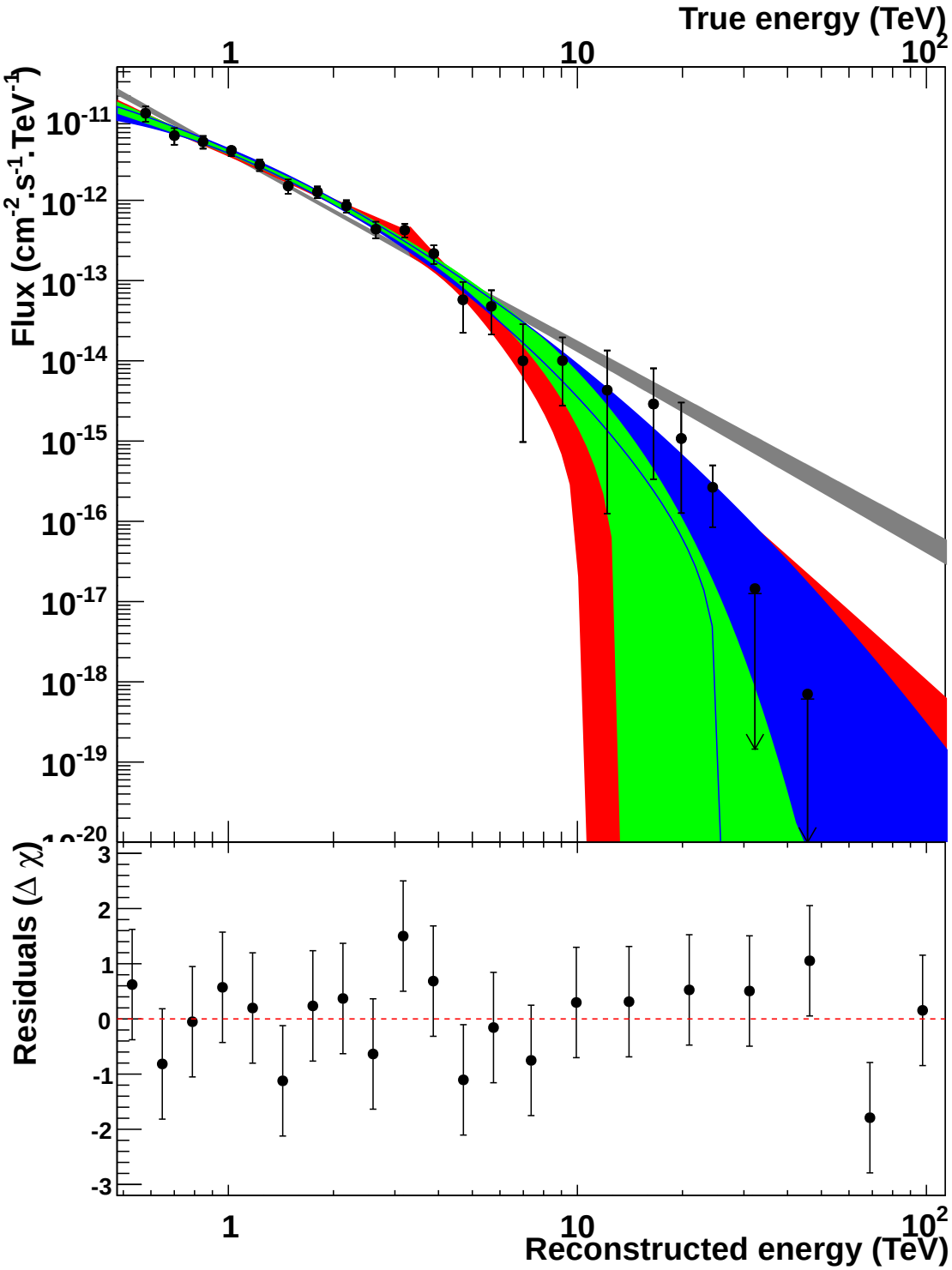

Figure 4.5: The energy spectrum of RCW 86 fitted with an exponential cut-off power-law shape. Overlaid are the 1σ confidence interval for the power-law (gray), the curved power-law (blue) and the broken power-law shape (red). The lower panel displays the residuals of the fit with the exponential cut-off power law.

Table 4.3: Results of the spectral analysis of RCW 86 for different analysis methods and cut configurations. In the F-Test column the significance of the better description of the spectrum with a more detailed spectral shape in contrast to a simple power-law shape is shown.

Analysis	Shape	Energy [TeV]	θ^2_{cut} $[deg^2]$	F(>1TeV) $\left[10^{-12}\mathrm{cm}^{-2}\mathrm{s}^{-1}\right]$	Norm $\left[10^{-12}\mathrm{TeV}^{-1}\mathrm{cm}^{-2}\mathrm{s}^{-1}\right]$	χ^2/dof	Index	Other Parameters [TeV]	F-Test
Published									
Hillas Std	PL	-	0.25		3.72 ± 0.5	6.30/4	2.54 ± 0.12	-	-
Hillas Std	EPL	-	0.25			2.96/3		-	1.8σ
Hillas Std	PL	1-10	0.25	2.34 ± 0.3	3.57 ± 0.5	0.68/2	2.41 ± 0.16	-	-
New Data whole source									
Model++ Std	PL	0.48-125	0.1681	9.61 ± 0.64	3.88 ± 0.25	80.1/70	2.404 ± 0.08	-	-
Model++ Std	ECPL	0.48-125	0.1681	6.51 ± 2.69	3.97 ± 0.27	62.3/69	1.50 ± 0.28	$E_C = (2.69 \pm 0.99)$	4.4σ
Model++ Std	CPL	0.48-125	0.1681	6.58 ± 1.03	4.14 ± 0.29	67.2/69	1.871 ± 0.15	$\beta = (0.44 \pm 0.13)$	3.6σ
Model++ Std	BPL	0.48-125	0.1681	6.325 ± 2.05	3.76 ± 0.25	66.1/73	1.96 ± 0.13	$\Gamma_2 = (4.17 \pm 1.64)$	2.7σ
								$E_{\mathrm{B}} = (3.23 \pm 0.71)$	
South-West part									
Model++ Std	PL	0.48-125	0.1681	2.18 ± 2.60	0.86 ± 0.10	49.7/40	2.39 ± 0.14	-	-
Model++ Std	ECPL	0.48-125	0.1681	1.30 ± 0.96	0.88 ± 0.11	48.3/39	1.834 ± 0.46	$E_C = (4.08 \pm 3.70)$	1.1σ

4.2.2 Spectrum of the South-West Part of the Supernova Remnant

The South-West part of RCW 86 is significantly brighter in other wavebands (see Section 2.5) than the other source regions. In the X-ray regime different spectral indices for the North-East and the South-West regions have been observed. Therefore in this thesis a separate spectral analysis of the South-West part was performed. The results are listed in Tab. 4.3. In Fig. 4.6 the spectrum fitted with a pure and an exponential cut-off power law are given. The spectral indices are 2.39 ± 0.14 and 1.834 ± 0.46 for a pure and an exponential cut-off power law, respectively. The cut-off energy of $E_C = (4.08 \pm 3.70)$ TeV is in good agreement with the results obtained for the whole source. It is not possible to distinguish weather an exponential cut-off power-law shape or a pure power-law one describes the data better. The improvement is quantified by a F-Test with a significance of 1.1σ. The spectral analysis of the South-West part of RCW 86 is compatible within errors with the one of the whole source.

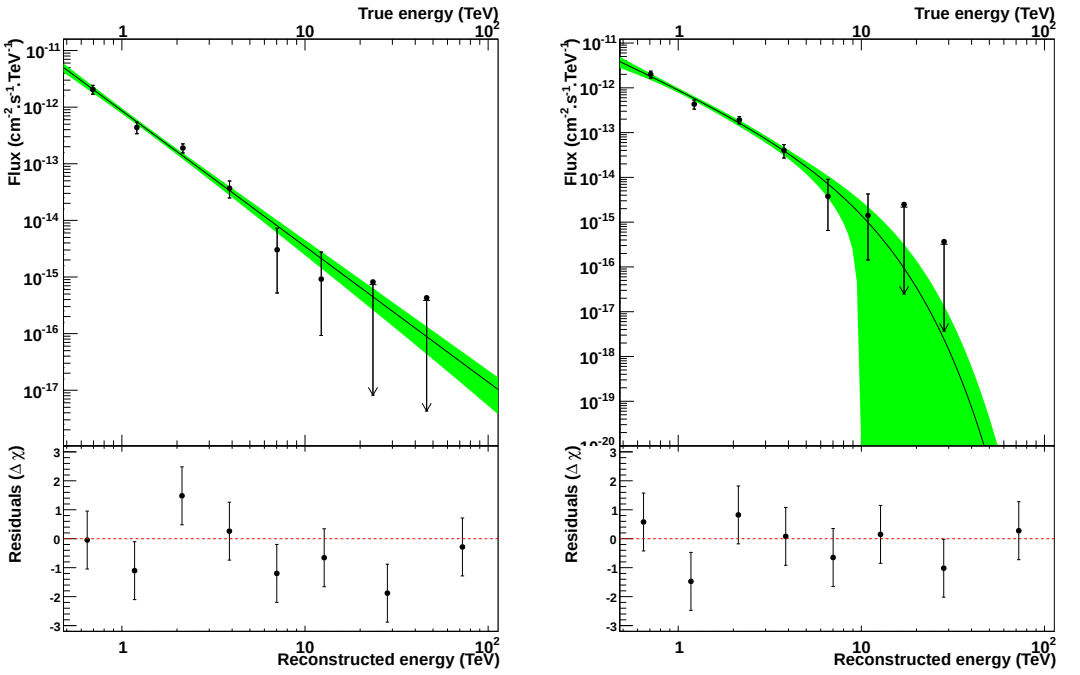

(a) bright South-West part of RCW86: power-law fit

(b) bright South-West part of RCW86: exponential cut-off power-law fit

Figure 4.6: The energy spectrum of the bright s South-West part of RCW 86 fitted with a power-law and a exponential cut-off power-law. The 1σ confidence interval for the fit is shown in green and the lower panel displays the residuals of the fit with the power-law.

4.3 Morphology

RCW 86 encounters a shell-like morphology in radio, optical and X-rays, whereas in the VHE γ-ray regime the shell-like and the sphere-like morphologies can not be distinguished. The Model++ analyses with its increased angular resolution as well as the larger data set allows for detailed studies of the morphology, which are presented in the following.

4.3.1 Study of the Morphology

The study of the morphology is based on a binned log-likelihood fit of a morphological model to the spatial distribution of the reconstructed events taking the Poisson-distributed nature of the data into account. The procedure is very similar to the spectral analysis in that sense that now the difference between the observed and the expected number of events in each sky map bin is quantified with a log-likelihood ($\mathrm{L} = \log(P)$) comparison taking the PSF into account. For the spectral analysis this is performed on the energy bins and with the system acceptance.

Therefore the probability P of observing N_{on} and N_{off} events under the assumption of n_γ γ-events and n_{h} hadron-events is calculated in each sky map bin with the Equation 4.2 taking Poisson statistics into account. Since n_h is not a parameter of the morphology shapes it is calculated from the observed n_γ. The best hadron estimate is given by the value of n_h which maximizes the log-likelihood $L = \log(P)$ for a given n_γ.

The estimated luminosity $\frac{\mathrm{d}^2 N}{\mathrm{d}x'\,\mathrm{d}y'}$ is defined as follows:

$$\frac{\mathrm{d}^2 N}{\mathrm{d}x'\,\mathrm{d}y'} = \int\int \mathrm{d}x\;\mathrm{d}y\;\mathrm{PSF}(r') \times \Phi(x,y). \tag{4.7}$$

$\Phi(x,y)$ is the source luminosity at specific coordinates x and y of the sky map and $\mathrm{PSF}(r')$ is the point spread function which depends only on the distance (and not on the angle, since the PSF is radially symmetric). The PSF is computed for a power-law spectrum taking the dependencies on the zenith angle θ and the off-axis angle δ into account. The influences of the PSF on the results are also studied in the following.
Consequently, the number of n_γ γ-events can be calculated as follows:

$$n_\gamma = \int\int \mathrm{d}x'\;\mathrm{d}y' \frac{\mathrm{d}^2 N}{\mathrm{d}x'\,\mathrm{d}y'} \tag{4.8}$$

The fit procedure is based on the Levenberg-Marquardt algorithm. The covariance matrix is calculated which allows to construct confidence regions for the different parameters.

In the following two source morphology shapes are tested. Their source luminosity functions $\Phi(x,y)$ are defined as follows:

- Sphere-like morphology

$$\Phi(x,y) = \frac{\Phi_0}{2\pi\sigma^2} \times e^{-\frac{(x-x_0)^2\cos^2\beta + (y-y_0)^2}{2\sigma^2}} \tag{4.9}$$

- Shell-like morphology (with a Gaussian profile)

$$\Phi(x,y) = \Phi_0 \times \exp\left[\frac{\left(\sqrt{(x-x_0)^2\cos^2\beta + (y-y_0)^2}\right) - r\right)^2}{2\sigma^2}\right] \tag{4.10}$$

In these functions Φ_0 is the normalization. The center of the source is defined by x_0 and y_0 and β stands for the declination angle of the source. The width of the Gaussian is defined by σ and the mean radius of the shell-like morphology is r.

The agreement of the data with the different source morphology shapes is tested with the likelihood ratio test (Mattox et al. 1996). In this test the probability is calculated weather a more complex model can better describe the data or not. The resulting test statistic (TS) value is defined as follows:

$$\mathrm{TS} = -2\frac{\log(\mathrm{L_{Shell}})}{\log\left(\mathrm{L_{Sphere}}\right)}\,. \tag{4.11}$$

According to Wilk's theorem (Wilks 1938), (Chernoff 1954) the TS values follow the chi-square distribution χ^2 with n degrees of freedom. Thereby n is the number of the additional parameters for the alternative hypothesis. Consequently, one can directly derive from the TS value the probability P for the better description of the data with the more complex model. The significance is calculated from the probability with the error function *Erf* as follows:

$$\sigma = \sqrt{2}\cdot \mathrm{Erf}^{-1}(1-P) \tag{4.12}$$

Results of the Study of the Morphology

In the publication neither the shell-like nor the sphere-like structure is preferred for the description of the morphology of RCW 86. The analysis was performed with the Hillas momentum analysis with standard cuts. The radial profile around the center of the VHE γ-ray emission ($-62.449° \pm 0.018°$ declination and $220.679° \pm 0.004°$ right ascension) was fitted with both a sphere- and a shell-like structure. The published results are given in Fig. 4.7. For a shell-like morphology a outer radius of $0.408° \pm 0.030°$ and a width of $0.207° \pm 0.070°$ was determined. The results are summarized in Tab. 4.4.

For the studies of the morphology the Model++ has the big advantage of a better sensitivity and angular resolution. Together with the larger data set it allows to study the structure of RCW 86. As cut configuration the Enhanced cut is used. Fig. 4.9 shows the excess map of RCW 86 smoothed with a Gaussian function with a width of $\sigma_{\mathrm{smooth}} = 0.05°$ which corresponds to the 68% containment radius of the PSF. Therein the white significance contours for 3, 4 and 5 σ, the radius and the fitted center of the shell-like shape are given in black. The black open circle indicates the fitted position in the publication (Aharonian et al. 2009).

Two different morphological models – shell and sphere – are fitted to the data by applying the binned log-likelihood fit discussed in Section 4.4. Fig. 4.8 gives the sphere- and shell-structure that results from the fit as well as the source center, $-62.446° \pm 0.017°$ declination and $220.709° \pm 0.041°$ right ascension for the sphere-like morphology and $-62.433° \pm 0.014°$ declination and $220.734° \pm 0.016°$ right ascension for the shell-like morphology. These results are in good agreement with the published values. The width and the normalization of the sphere-like morphology are σ of $0.225° \pm 0.070°$ and Φ_0 of $3.478]10^{-3}\mathrm{s}^{-1}\mathrm{deg}^{-2}$, respectively. For the shell the width, the radius and the normalization are σ of $0.125° \pm 0.014°$, r of $0.194° \pm 0.016°$ and Φ_0 of $9.508\,10^{-3}\mathrm{s}^{-1}\mathrm{deg}^{-2}$. The parameters are summarized in Table 4.4.

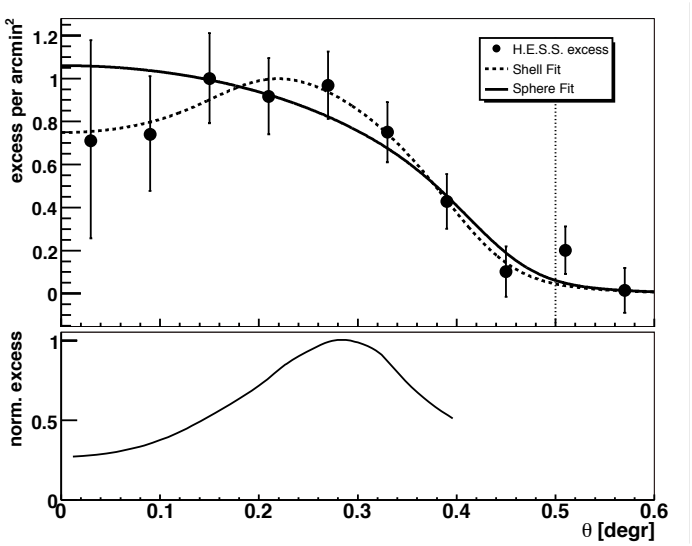

Figure 4.7: The radial profile plot around the fitted center of RCW 86 is presented. The H.E.S.S. excess is marked with black dots and the fits of the sphere-like and a shell-like models are shown. The dotted vertical line illustrates the extent of the region used for the azimuthal profile. Lower panel: Radial profiles of the X-ray data (3-6 keV) from XMM-Newton. These data are smoothed to match the H.E.S.S. angular resolution and normalized. (Image taken from Aharonian et al. (2009)).

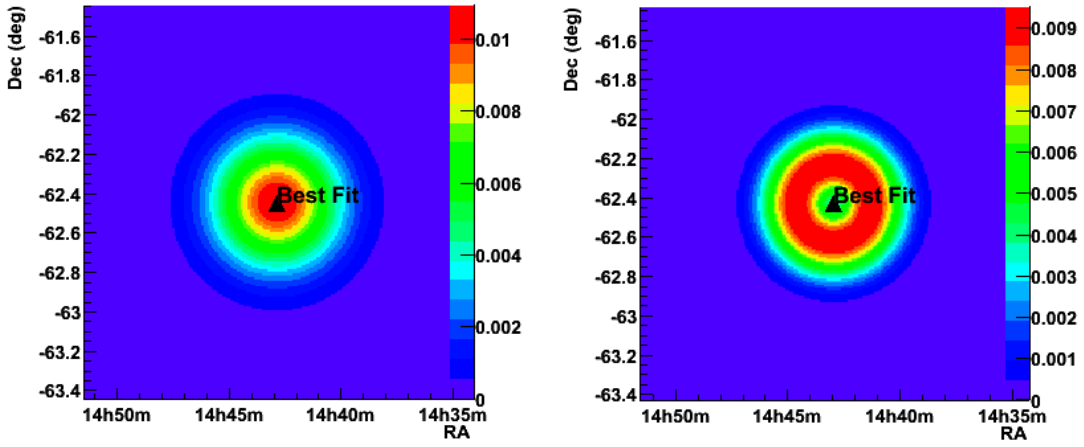

(a) Sphere-like morphology

(b) Shell-like morphology

Figure 4.8: Results of the 2D likelihood fit of the morphology shapes to the RCW 86 data (parameter results see text and Tab. 4.4).

Table 4.4: Results of the spectral analysis of RCW 86 for different analyses and cut configurations. In the test statistic column the significance of the better description of the morphology with a shell-like shape in contrast to a sphere-like shape is shown.

Analysis	Shape	Source center		Width	Radius	Φ_0	Loglikelihood	TS
		Dec. [°]	R.A. [°]	σ [°]	r[°]	$[10^{-3}\mathrm{s}^{-1}\mathrm{deg}^{-2}]$		$[\sigma]$
Published								
Hillas Std	Sphere	-62.449 ± 0.018	220.679 ± 0.004					
Hillas Std	Shell	-62.449 ± 0.018	220.679 ± 0.004	0.207 ± 0.070				
New data								
Model++ Std								3.6
Model++ Enhanced	Sphere	-62.446 ± 0.017	220.709 ± 0.041	0.225 ± 0.070	–	3.478	-17435.2	
Model++ Enhanced	Shell	-62.433 ± 0.014	220.734 ± 0.016	0.125 ± 0.014	0.194 ± 0.016	9.508	-17410.3	**6.7**

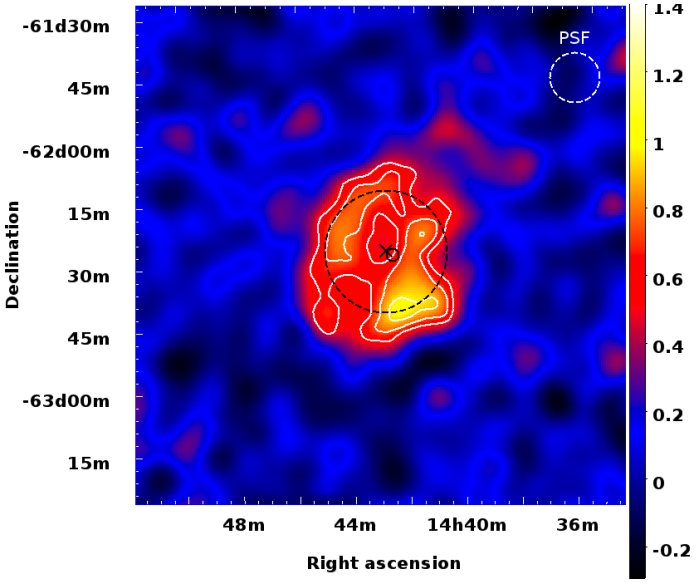

Figure 4.9: The acceptance corrected excess map of RCW 86 for the Model++ Enhanced overlaid with white significance contours for 3,4 and 5σ and the radius (black dashed circle) and the fitted center of the shell-like morphology shape (cross) in black. The data is smoothed with a Gaussian function with a width of $\sigma_{\text{smooth}} = 0.05$. This width is chosen since it represent the 68% containment radius of the PSF for this analysis. The PSF for this analysis and smoothing is shown in the upper right corner. The small black open circle indicates the fitted position in the publication.

Using the Test statistic (see Eq. 4.11) for the new data set and the Model++ Std analysis a probability of 3.6σ is calculated that a shell-like shape better describes the data compared to a sphere-like shape. With the new data set and the Model++ Enhanced analysis a probability of 6.7σ is derived in the analysis of the morphology and a sphere-like shape is ruled out in comparison to the shell-like shape. Fig. 4.10 shows the radial profile of RCW 86. The data are shown in black and the sphere-like and shell-like morphology shape in red and blue, respectively. For the shell-like morphology also the shape without convolution with the PSF is presented.

The result of the study of the morphology strongly depends on the PSF. To study its dependence, the PSF was fitted by a double Gaussian function (see Eq. 3.14) and the analyses was performed again with increased and decreased PSF widths of +10% and -10%, respectively. The probability of a shell like structure compared to a sphere drops for the broader PSF to 6.3σ and for a narrow PSF it increases to 7.6σ.

In X-rays the emission of RCW 86 is dominated by a bright South-West part. Therefore the dependency of the VHE γ-ray azimuthal profile is given in Fig. 4.14. The emission is radially integrated between 0°and 0.5°. As one can see no dependency is present.

The conclusion of the morphology study of RCW 86 is that a shell-like morphology is preferred over a sphere-like morphology by a probability of $6.7^{+0.9}_{-0.4}\sigma$. The upper and lower error indicates the results derived with the 10 % broader and narrower PSF.
Hence, RCW 86 belongs to the group of the shell-like supernova remnants detected in the VHE γ-ray regime.

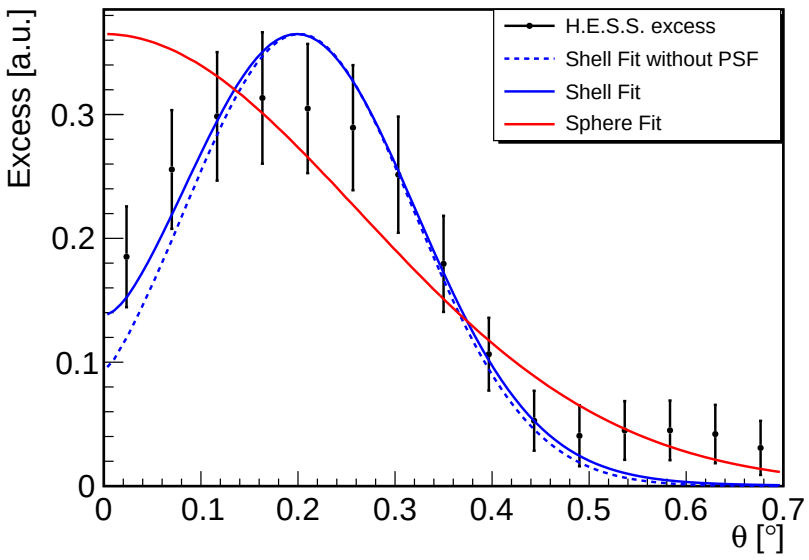

Figure 4.10: Radial distribution of the events of RCW 86 with the Model++ Enhanced data. The data are shown in black and the sphere-like and shell-like shape in red and blue, respectively. For the shell-like morphology also the shape without convolution with the PSF is presented (blue dashed line).

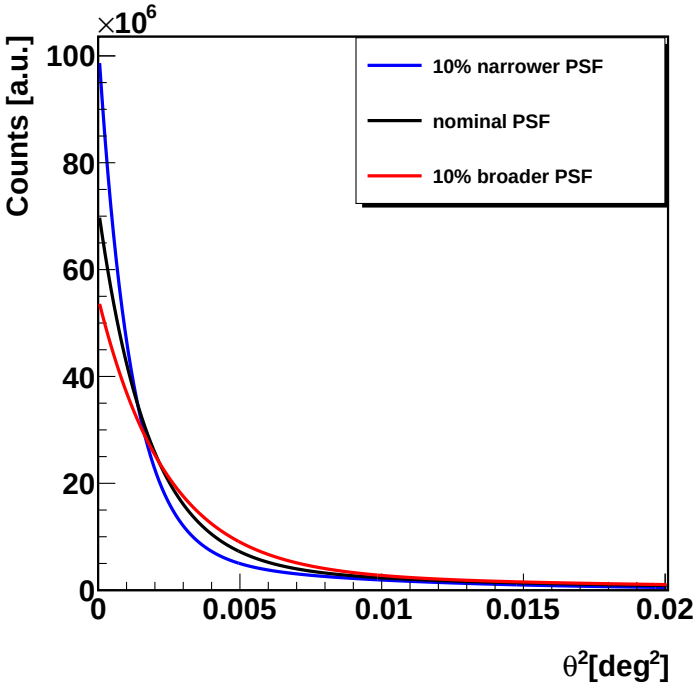

Figure 4.11: The PSF for the Model++ Enhanced analysis in black and the double Gaussian functions for a 10 % broader and narrower PSFs in red and blue, respectively.

4.3.2 Morphological Comparison of X-rays and VHE γ-ray data of RCW 86

In this section the correlation of the X-ray and the newly analyzed VHE γ-ray data is studied. The X-ray observations are performed by the XMM-Newton satellite and the results are kindly provided by Jacco Vink. In Fig. 4.12 the X-ray sky map is presented. The covered energy range is 2 keV to 4 keV. The emission consists of non-thermal X-rays which is caused by highly accelerated electrons. This population can also be the primary one for the VHE γ-ray emission and therefore correlation studies between the different energy ranges is of great interest.

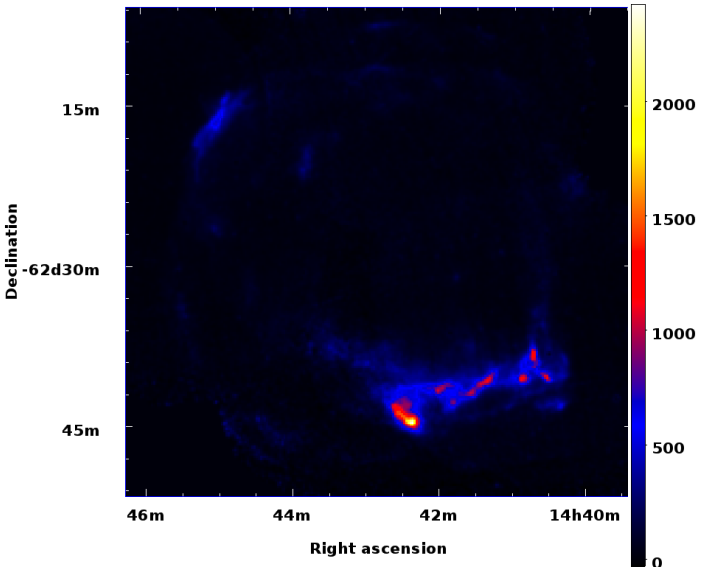

Figure 4.12: XMM-Newton data of RCW 86 taken in the energy range from 2 keV to 4 keV

Fig. 4.13 shows the VHE γ-ray map produced by the Model++ analysis with the Enhanced cut configuration. The map is smoothed with a Gaussian function with a width of $\sigma_{\text{smooth}} = 0.05°$. This width represents the 68% containment radius of the PSF. The PSF is given in the upper right corner of the image. Additionally the XMM-Newton data are overlaid in black. An overall spatial correlation between the X-ray and the VHE γ-ray data can be seen which is studied in more detail in the following.

For the comparison of the azimuthal and radial distribution of the X-rays and the VHE γ-rays the XMM-Newton map is smoothed with the larger PSF of the H.E.S.S. data and their distributions are scaled to a maximum value of 0.5. The azimuthal distribution of the XMM-Newton and H.E.S.S. data of RCW 86 is presented in Fig. 4.14. In the X-rays the South-West part of RCW 86 is significantly brighter than the rest of the source. This is in contrast to the H.E.S.S. data, where the azimuthal brightness is nearly flat. For both data sets the emission is integrated from a radius of 0° to 0.5°.

In Fig. 4.15 the radial distribution for both analyses are displayed. In both cases the shell-like morphology is clearly visible. But in X-rays the radius of the shell is larger and the shell thickness is smaller. Therefore on one side the large-scale structures are similar but on the other side the fine structures differ.

Finally the correlation coefficient of the VHE γ-ray data and the X-ray data convolved with the H.E.S.S. PSF is calculated within the field of view of the X-ray observations. This leads to a value of 0.48 which is pretty low and can be interpreted that the VHE γ-ray and the X-ray emission is produced in different regions of the SNR. Additionally as one can see in the sky map of the X-ray observations, the shell structure covers only a small fraction of the image, therefore it is

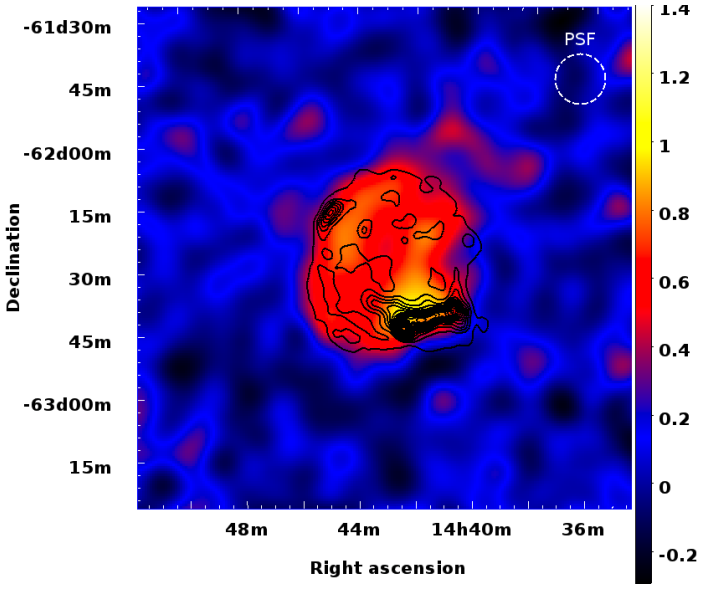

Figure 4.13: The acceptance-corrected excess map of RCW 86 for the Model++ Enhanced analysis overlaid with black contours of the XMM-Newton data. The data are smoothed with a Gaussian function with a width of $\sigma_{\text{smooth}} = 0.05°$. This width is chosen since it represents the 68% containment radius of the PSF for this analysis. The PSF for this analysis and smoothing is shown in the upper right corner.

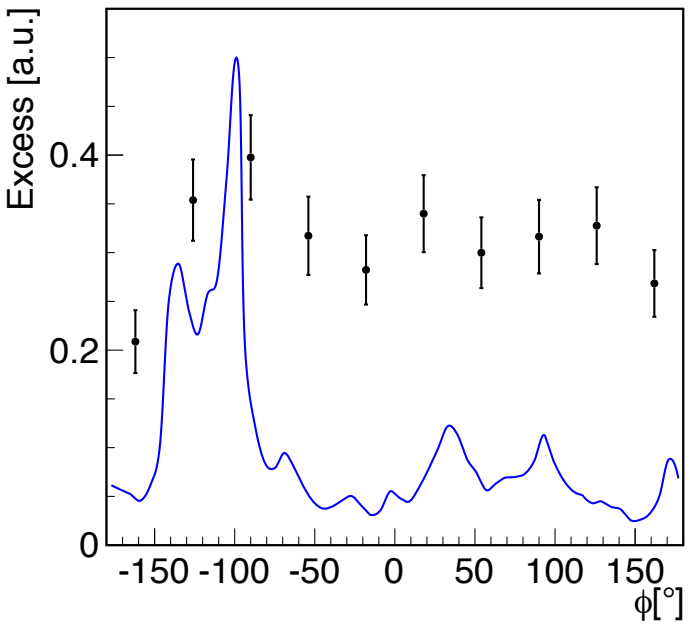

Figure 4.14: Azimuthal distribution of the events of RCW 86: VHE γ-ray data in black points and the X-rays in a blue solid line. The X-ray data are smoothed with the H.ES.S.S. PSF and scaled to a maximum value of 0.5. 0°corresponds to the East and 90°to the North. In the sky maps East is to the right and North at the top.

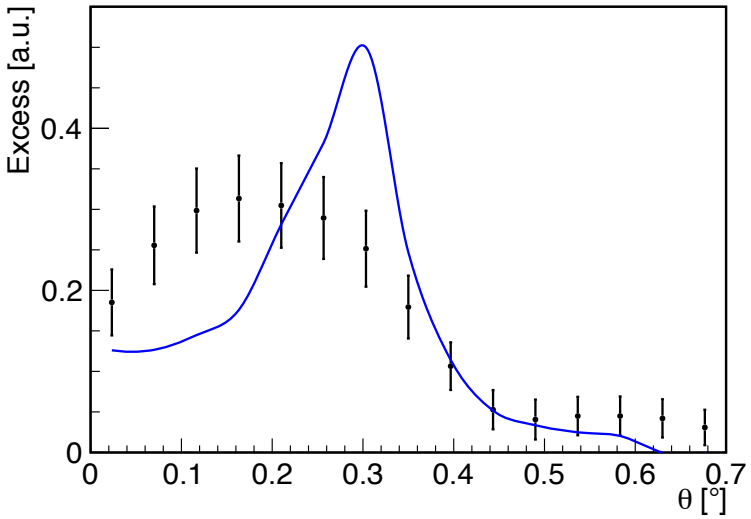

Figure 4.15: Radial distribution of RCW 86: the VHE γ-ray data in black points and the X-rays in a blue solid line. The X-ray data are smoothed with the H.E.S.S. PSF and scaled to a maximum value of 0.5.

also possible, that the coefficient is dominated by regions without measurable signals. For a more detailed study of the morphology an improved angular resolution is mandatory. Therefore in the next chapter deconvolution techniques are studied.

5 Deconvolution Studies and its Application to VHE γ-ray data

After the description of the H.E.S.S. view of RCW 86 in the last chapter, this part of the thesis is focused on deconvolution techniques employed to study the morphology of extended VHE γ-ray sources by improving the angular resolution even beyond the restriction of the point spread function (PSF). The deconvolution technique is newly introduced into the VHE γ-ray astronomy. The method of choice is the Richardson-Lucy algorithm.

This chapter is adopted from the article "Systematic studies of the Richardson-Lucy deconvolution algorithm applied to VHE gamma-ray data" (Heinz et al. 2012), which summarizes the results of the detailed systematic studies performed during my thesis.

5.1 Introduction to the Deconvolution Technique

As already mentioned in the introduction of this dissertation, more than 120 sources and a variety of different source classes are detected in the VHE γ-ray range so far. Most of them are extended and exhibit a detailed structure. For example, shell-like morphologies have been observed in SNRs (see Section 2.4) and especially in RCW 86 (see Section 4.3.1). These SNRs are primary candidates for hadronic cosmic-ray acceleration, but leptonic scenarios cannot be ruled out. By the use of correlation studies between observational data from different wave bands and the detailed knowledge of the source morphology the emission region can be located and the underlying processes responsible for the γ-ray emission can be uncovered. The main problem is that imaging X-ray instruments typically have a better angular resolution than VHE γ-ray detectors. ASCA and XMM-Newton have for example an angular resolution superior by about a factor of 2 and 100, respectively, compared to VHE γ-ray instruments.

To get rid of this problem and to unveil the true morphology of VHE γ-ray sources, the application of the Richardson-Lucy deconvolution algorithm (RLA) (Richardson (1972); Lucy (1974)) to γ-ray images is presented in this Chapter. The Richardson-Lucy algorithm is a maximum likelihood method commonly used in astronomy. On the one hand an advantage of the RLA is the conservation of the global flux but on the other hand there are also disadvantages like noise amplification and unstable solutions. Since in the VHE regime the noise level is usually of the same order as the signal strength (see Section 3.4.4), a detailed understanding of the behavior of the algorithms is necessary in order to be able to extract improved images of VHE γ-ray sources. In this chapter, detailed systematic studies of the deconvolution of VHE γ-ray data based on the RLA are presented. First, the technique is described, followed by detailed simulation studies. Finally, the algorithm is applied to simulated and observational VHE γ-ray data of the strongest extended VHE γ-ray source, the SNR RX J1713.7−3946 and also to simulated and observational VHE γ-ray data of RCW 86.

5.2 The Richardson-Lucy Algorithm

Under the assumption of a perfect experiment a point source would be projected onto a single point in the observed astronomical image $I(x,y)$. In the following the right ascension (RA) is on the x-axis and the declination (Dec) on the y-axis of $I(x,y)$, this is a so-called sky map. In reality due to uncertainties of the experiment the point source image is broadened which is quantified by the PSF (see Section 3.4.4) and an additional background exists (see Section 3.4.4). This is illustrated in Fig. 5.1 and can be mathematically expressed by:

$$I(x,y) = (O \otimes P)(x,y) + B(x,y) \tag{5.1}$$

where $B(x,y)$ is an additive background and $(O \otimes P)(x,y)$ represents the convolution of the true source image $O\left(x_{n_x}, y_{n_y}\right)$ with the PSF $P\left(x - x_{n_x}, y - y_{n_y}\right)$:

$$(O \otimes P)(x,y) = \sum_{n_x,n_y=1}^{N_x,N_y} O\left(x_{n_x}, y_{n_y}\right) \cdot P\left(x - x_{n_x}, y - y_{n_y}\right) \tag{5.2}$$

N_x and N_y are the number of bins of the x- and y-axis, respectively. Deconvolution techniques allow to restore the original image under the assumption, that the PSF is known.

The Richardson-Lucy algorithm is an iterative algorithm based on the Bayes' theorem and was developed for Poisson distributed background (Richardson (1972); Lucy (1974)). Therefore it is suitable for VHE γ-ray data. The iterative formula of the RLA is:

$$O^{n+1}(x,y) = \left[\frac{I(x,y)}{(P \otimes O^n)(x,y)} \otimes P^T(x,y) \right] O^n(x,y) \tag{5.3}$$

In each iteration the probability increases, that the true source image $O(x,y)$ is represented by $O^{n+1}(x,y)$. Using the Bayes's postulate the initial estimation $O^0(x,y)$ is a uniform distribution. The RLA is a maximum likelihood estimator (Lucy 1974).

For images with a low signal-to-noise ratio, the RLA tends to interpret statistical fluctuations as real structures leading to large fluctuations in the deconvolved image. The strength of the fluctuations depends on the significance of the structures and the number of performed iteration steps. From now on these fluctuations are called artifacts.

In the following sections a detailed study of the RLA is presented including the behavior of the artifacts. Therefore Monte Carlo simulations have been performed, which are described in the following Section 5.3.

5.3 Simulation of VHE γ-ray Maps

A Monte Carlo simulation was developed to derive the optimal number of iterations for the RLA and to quantify the improvement of the angular resolution for a given source morphology, background level, and source significance. The optimal number of iteration (N_{opt}) is reached when the relative error RE between model and deconvolved image is minimal (see Eq. 5.5).

The simulation takes into account the analysis steps of a standard Hillas analysis to receive as output a realistic acceptance-corrected excess map (ACEM), which is a sky map filled with excess events which are acceptance-corrected. The region background model is used (see Section 3.4.4)

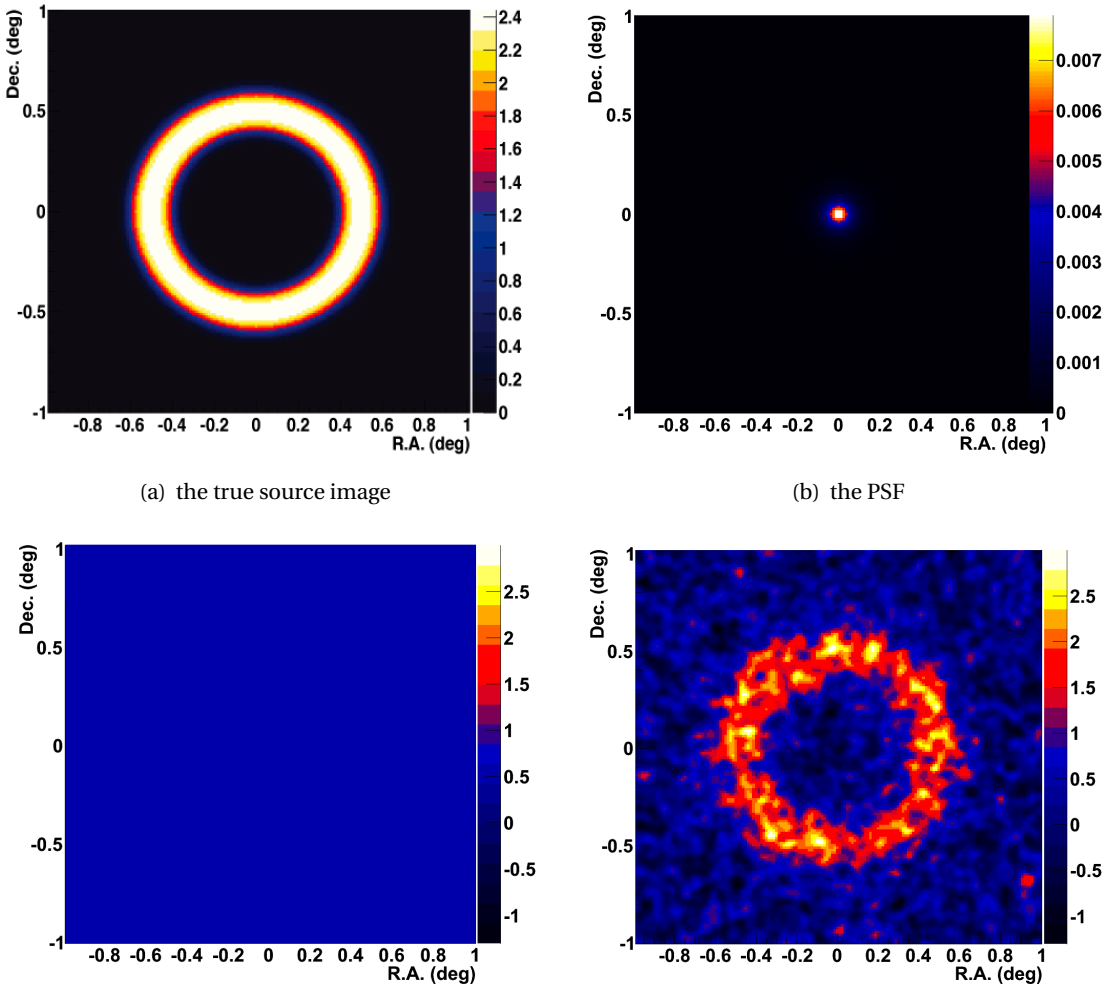

(a) the true source image

(b) the PSF

(c) the model for the additional background

(d) the observed astronomical image

Figure 5.1: Illustration of the convolution: (a) the true source image $O\left(x_{n_x}, y_{n_y}\right)$ is convolved with (b) the PSF $P\left(x - x_{n_x}, y - y_{n_y}\right)$. With (c) the model for the additional background $B(x,y)$, (d) the observed astronomical image $I(x,y)$ can be described.

and the ACEM represents the image $I(x,y)$ for the deconvolution. The number of γ-ray excess events is defined as

$$N_{\text{excess}} = N_{\text{on}} - \alpha N_{\text{off}}, \tag{5.4}$$

where N_{on} is the number of counts in a test region and N_{off} in a background region. Typical values for the normalization parameter α are in the order of about 0.07 and therefore this value is adopted in this Chapter. For the ACEM $I(x,y)$ the excess is calculated at each position of the map and corrected by the acceptance differences over the FoV.

The input parameters of the simulation are the background level and the source significance calculated according to Eq. 3.17. The simulations are performed for different source morphologies: point, ring and ellipse. The used PSF is for 20° zenith angle (see Section 3.4.4) and the noise is assumed to be Poisson distributed.

The course of the simulation is the following:
"First, the source morphology is parametrized (source-model), a constant background is added and then convolved with the system acceptance resulting in a model for the N_{on} on event distribution (On-model). According to the selected background level and the significance, the number of events N_{on} is calculated and distributed randomly according to the On-model while taking the PSF into account. After adding Poisson noise the obtained map represents the distribution of N_{on} of Eq. 5.4.

To derive N_{off}, the calculated background events are divided by the α-factor and are randomly distributed according to the acceptance while taking the PSF into account. Application of Eq. 3.15 with corrections for the acceptance leads to the simulated ACEM." (Heinz et al. 2012)

For each set of simulation parameters 100 simulations were performed to determine the error on the simulation results with good statistics. For the error estimation of a specific parameter related to the deconvolution procedure the RMS value of its parameter distribution is calculated.

Code Implementation

The RLA was implemented by Fabian Schöck and myself in ROOT: an object-oriented data analysis framework (Rademakers & Brun 2011). It uses the Fast Fourier Transformation FFTW3 (Frigo & Johnson 2005) for a good performance of the convolution. The simulation used for the detailed studies is developed by myself in ROOT.

5.4 Systematic Studies

The influences of the number of iterations, the significance and the reconstructed source morphology on the following parameters

- the strength of the artifacts,
- the improvement of the angular resolution,

have been investigated.

The quality of the deconvolved image is quantified by the relative error

$$RE = \sqrt{\frac{\sum_{i,j}^{n_i,n_j} \left(N_{\text{excess}}(x_i,y_j) - N_{\text{model}}(x_i,y_j)\right)^2}{\sum_{i,j}^{n_i,n_j} N^2_{\text{model}}(x_i,y_j)}} \tag{5.5}$$

$N_{\text{model}}(x_i,y_j)$ is the number of events of the source model at the position (x_i,y_i). x_i and y_i stand for the center of the right ascension and declination bin. To limit the RE to the source region, the RE is calculated within a circular region around the source center with a radius r_{comp}, which is given as:

$$r_{\text{comp}} = r_{\text{source}} + 0.15^\circ \tag{5.6}$$

where r_{source} is the source radius. This predefined area allows to measure the improvement due to deconvolution and to reduce the dependence on the behavior of the background.

5.4.1 Study of the Angular Resolution

First of all, the angular resolution as a function of the number of iterations was studied. The 68% containment radius r_{68} of a point source is an appropriate measure for the angular resolution. Fig. 5.2 shows r_{68} as a function of the number of iterations for different source significances of 20σ, 40σ, 60σ, 80σ and 100σ, while the background level was kept constant at 2900 background events in the source region. The number of background events represents the number for a typical galactic source with 10 hours of observations at a zenith angle of 20° with the H.E.S.S. telescope system.

For the RLA the dependence on the source strength is very weak. After the first iteration step, the resolution is worse compared to the initial one which can easily be explained by the fact that $O^0(x,y)$ (see Eq. 5.3) is a uniform distribution and it takes the first iteration step $O^1(x,y)$ to get a raw approximation of the structure. With the third iteration, an improvement of about 20% compared to the initial PSF is achieved and after about 6 iterations an improvement of about 50% can be obtained.

5.4.2 Studies of the Influence of the Artifacts on the Deconvolution

The strength of the artifacts produced by the RLA depends on the number of iterations and on the low signal-to-noise ratio. Fig. 5.3 shows the ACEM of a ring-like morphology with an outer and inner radius of 0.4° and 0.2°, respectively. It is clearly visible in Fig. 5.3(b) that the underlying morphology becomes blurred by the artifacts if too many iterations are performed. Therefore, it is important to determine the optimal number of iterations N_{opt} for which the relative error RE is minimal.

The same simulated morphology is used for Fig. 5.4 which presents RE as a function of the number of iterations for a source with a ring-like morphology. At first RE decreases with increasing number of iterations until it reaches a minimum at 3 iterations and then starts to increase again. This minimum represents the optimal number of iterations N_{opt} yielding the best fit between source-model and deconvolved image or, in other words, the point where the severity of artifacts is minimal.

In a next step the application of the deconvolution on different source morphologies (ring and elliptical) have been investigated dependent on the source strength. Fig. 5.5 and Fig. 5.6 show

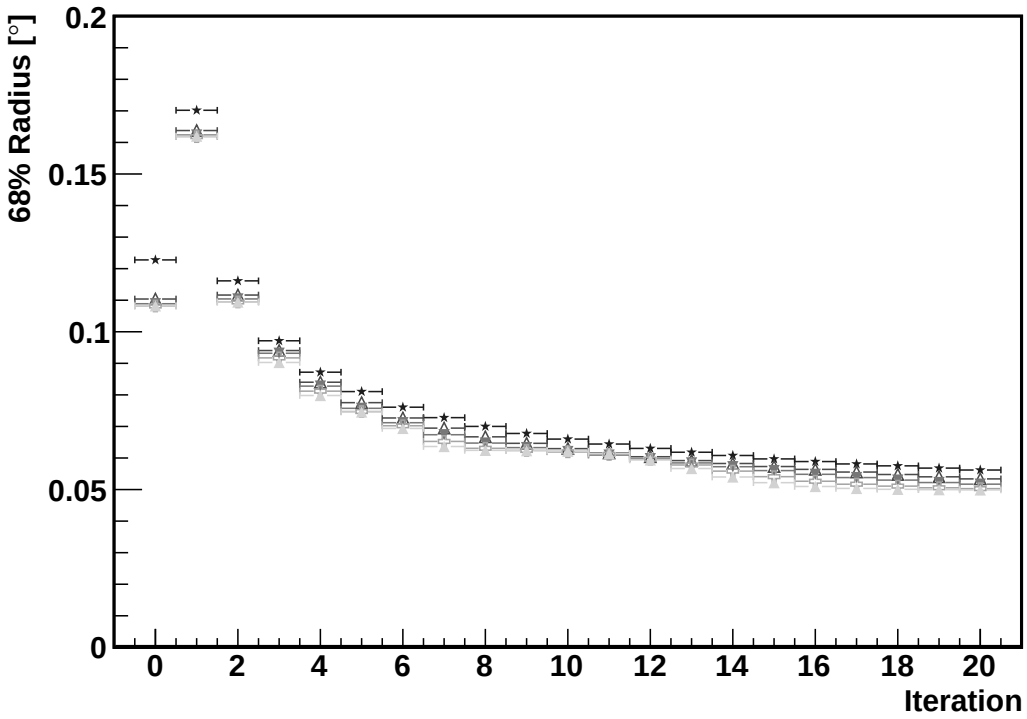

Figure 5.2: The 68% containment radius of the image of a point source is a measure of the angular resolution. Its behavior as a function of iterations for different source significances is shown. The black stars, open triangles, filled triangles pointing downward, open crosses and filled triangles pointing upwards stand for 20σ, 40σ, 60σ, 80σ and 100σ, respectively.

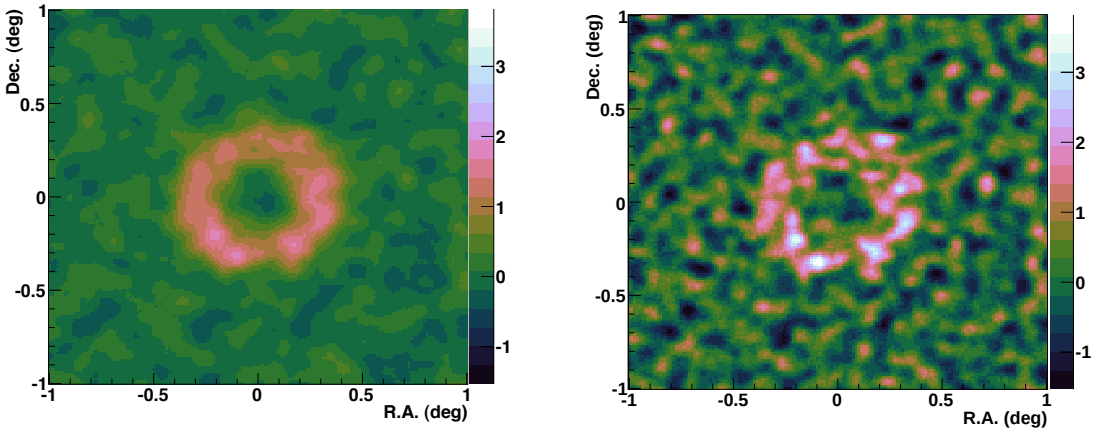

(a) (b)

Figure 5.3: Given are the ACEM deconvolved with optimal number of iteration (a) and with 20 iterations (b). The artifacts can be clearly seen.

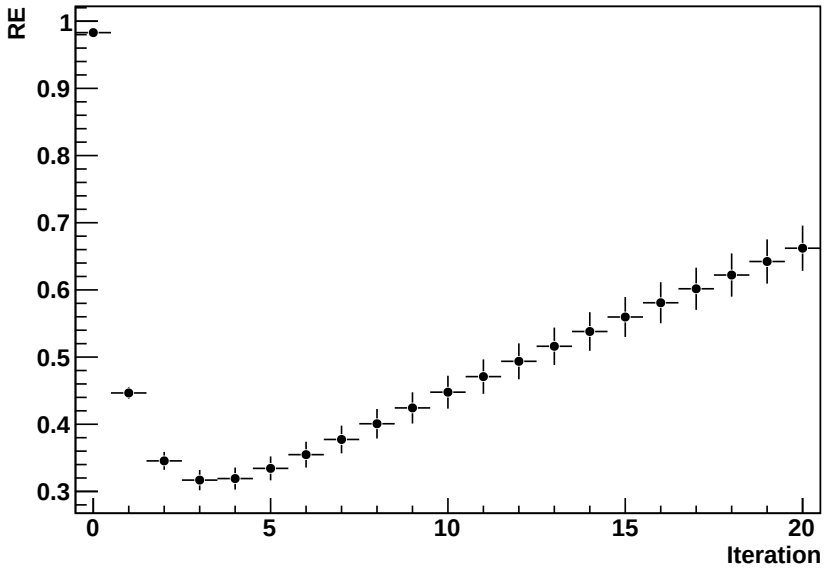

Figure 5.4: RE as a function of iteration number for a source with ring-like morphology. The outer and inner radii are 0.4° and 0.2°, respectively.

the optimal number of iterations N_{opt} as a function of source significance for ring- and elliptical morphologies, respectively. The number of possible iterations increases with increasing significance which can be explained by the fact that statistical fluctuations create only smaller artifacts for stronger sources. Additionally different sources with the same significance but different radii, the optimal number of iterations decreases when the outer source radius increases, since the signal-to-noise ratio worsens with increasing source size. With regard to the applicability of the RLA to VHE γ-ray sources one has to note that only for strong sources an improvement of the angular resolution of better than $\sim$50% can be achieved by using a sufficiently large number of iterations.

Another aspect of the deconvolution is given in Fig. 5.7 for a ring-like morphology and Fig. 5.8 for an elliptical morphology. The RE is plotted as a function of significance before and after deconvolution with the optimal number of iterations N_{opt}. The RE before is flagged with open markers and the RE after deconvolution with filled markers. The improvement is nearly independent of the source morphology and in the order of a factor of 10. This can be explained by two facts: The first one is that the fluctuations of the data are balanced and the second one is that the angular resolution is improved. This allows to reveal the true source structure.

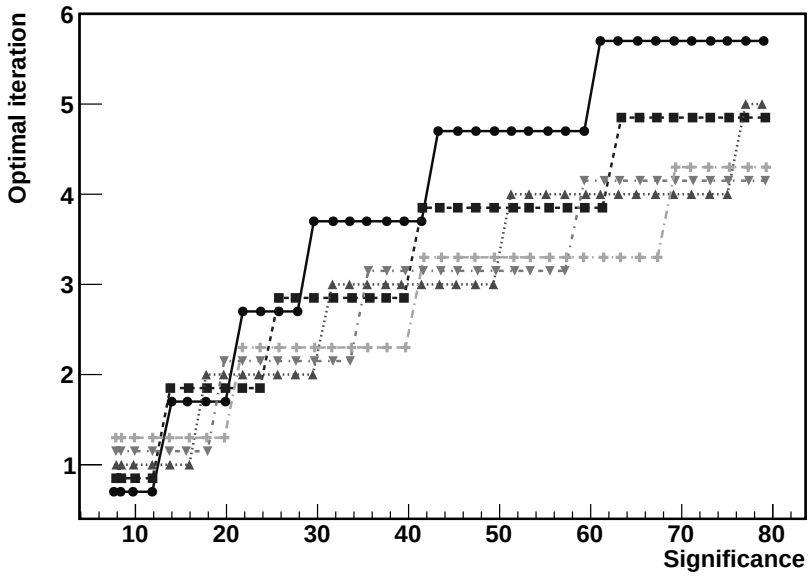

Figure 5.5: The optimal number of iterations N_{opt} as a function of the source significance for a ring-like source morphology. The ring width was kept constant at 0.2° while the radii varied. The outer radii are 0.3° (dots) , 0.4° (squares) , 0.5° (triangles pointing upwards), 0.6° (triangles pointing downwards) and 0.7° (crosses).

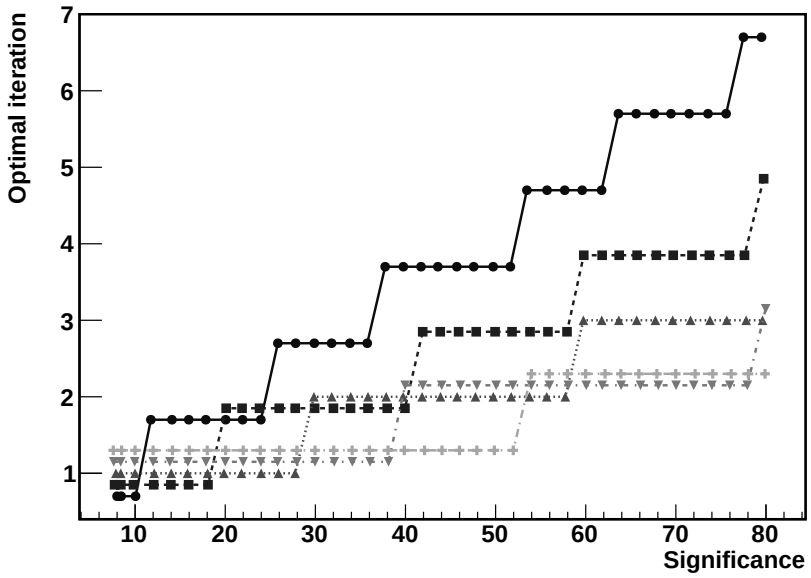

Figure 5.6: The optimal number of iterations N_{opt} as a function of the significance for a elliptical source morphology. The radius was varied. (0.3° (dots) , 0.4° (squares) , 0.5° (triangles pointing upwards), 0.6° (triangles pointing downwards) and 0.7° (crosses).

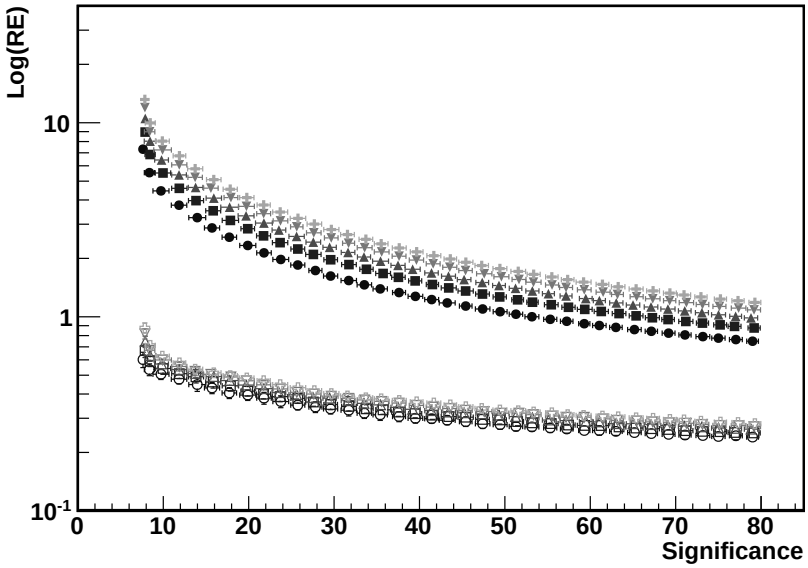

Figure 5.7: RE versus significance before and after deconvolution for a ring-like source morphology. Filled markers label RE before RLA application and open markers after deconvolution. The ring width was kept constant at 0.2° while the radii varied. The outer radii are 0.3° (dots) , 0.4° (squares) , 0.5° (triangles pointing upwards), 0.6° (triangles pointing downwards) and 0.7° (crosses).

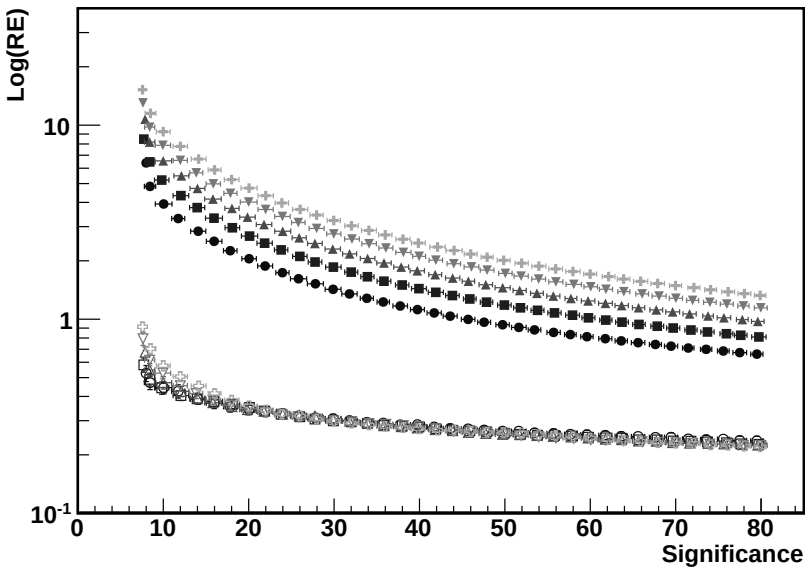

Figure 5.8: RE versus significance before and after deconvolution for an elliptical source morphology. Filled markers label RE before RLA application and open markers after deconvolution. The radius was varied (0.3° (dots) , 0.4° (squares) , 0.5° (triangles pointing upwards), 0.6° (triangles pointing downwards) and 0.7° (crosses)).

5.5 Application of the Richardson-Lucy Algorithm

After the detailed studies of the dependencies of the RLA in the previous Section 5.4, the application of the RLA to correlation studies between different wavebands is evaluated. It is assumed, that two observations of one source in different wavebands is available. One with a better resolution. Normally, this one is smoothed to the angular resolution of the worse one. After this preprocessing correlation studies between the observations are an established method for the determination of the underlying acceleration processes. In the following the deconvolution is used instead of the smoothing to study the correlation on smaller scales. In this section correlations between the morphology of different observations is determined before and after applying the deconvolution. The results of this study allow to apply the RLA to the H.E.S.S. data of the SNRs RX J1713.7−3946 and RCW 86 to determine the correlation with X-ray data.

5.5.1 Correlation Studies between simulated VHE γ-ray and X-ray Data

As already mentioned in the introduction of this chapter X-ray instruments have a better angular resolution compared to the VHE γ-ray instruments. ASCA[1] has for example an angular resolution about a factor of two better than VHE γ-ray instruments.

Therefore two ACEMs are simulated with the same ring-like morphology, but different PSFs to mimic the angular resolution of the H.E.S.S. and the ASCA instruments. The strength of the source is 39σ and the size was chosen to have an outer radius of 0.4°and an inner one of 0.2°corresponding to the one used in Fig. 5.4. A value of 3 was derived for N_{opt} which means that an improvement of the angular resolution of about 20% can be achieved.

In Fig. 5.9 the correlation coefficient between the two simulated ACEMs is plotted dependent on the bin size. The coefficient was determined in a quadratic region around the source center with a border size of 1.1°. Without deconvolution the correlation coefficient increases significantly with increasing bin size.

In contrast to the case without deconvolution the correlation coefficient is now nearly independent of the bin size. This is based on two facts: The first one is that the fluctuations of the data are compensated and the second one is that the angular resolution is improved.

In a second test the influence of the ring thickness on the correlation coefficient is studied. The outer radius is fixed to 0.4° , the same value like above, but the ring thickness is varied from 0.01° to 0.2°. The results are illustrated in Fig. 5.10. The already mentioned behavior for the correlation between the simulated ASCA and H.E.S.S. ACEMs is clearly visible also for the thinnest structure. A slightly higher correlation coefficient is seen for thicker rings, which can be explained by the fact that the ratio of the area of the source is bigger compared to the area of pure background. In the background area the differences are higher than in the signal region.

The results show, that the deconvolution allows to study fine structures of extended VHE γ-ray sources down to a level of 0.01°.

5.5.2 Application to the VHE γ-ray Data of RX J1713.7−3946

The shell-type SNR RX J1713.7−3946 is the strongest extended VHE γ-ray source and therefore the best-studied so far. The source is slightly asymmetric. Former correlation studies performed by

[1] Advanced Satellite for Cosmology and Astrophysics

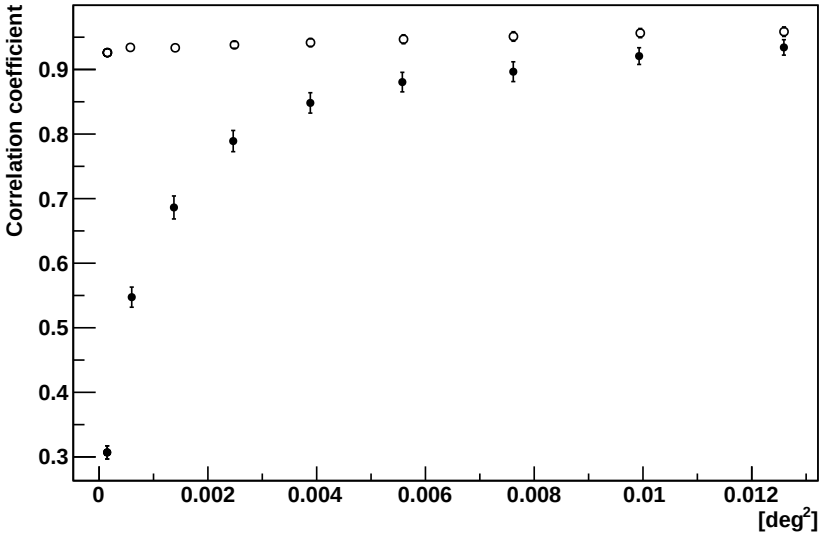

Figure 5.9: Correlation between simulated X-ray and VHE γ-ray data as a function of bin size. The region for the calculation of the coefficient before and after the deconvolution of the H.E.S.S. data is a priori chosen to contain the whole source and to depend mainly on the signal and to avoid regions with only background. In particular for smaller bin sizes, an increase of the correlation coefficient for the deconvolved map (open circles) as compared to the original map (filled circles) is found.

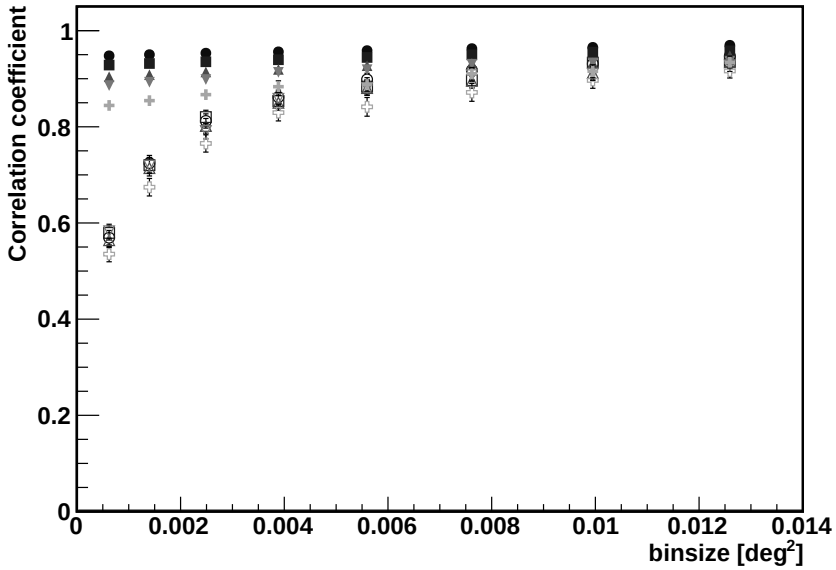

Figure 5.10: Correlation between simulated X-ray and VHE γ-ray data for different ring thickness as a function of bin size. The region for the calculation of the coefficient before and after the deconvolution of the H.E.S.S. data is a priori chosen to contain the whole source and to depend mainly on the signal and to avoid regions with only background. The outer radius is fixed to 0.4. The width of the ring was varied. (0.2° (dots) , 0.15° (squares) , 0.1° (triangles pointing upwards), 0.05° (triangles pointing downwards) and 0.01° (crosses). In particular for smaller bin sizes, an increase of the correlation coefficient for the deconvolved maps (filled markers) as compared to the original maps (open markers) is found.

(Tanaka et al. 2008) found a correlation coefficient of 0.83 between the H.E.S.S. data and 2–5 keV X-rays, while for the 5–10 keV band a correlation coefficient of 0.85 was determined. These correlation were calculated using a square shaped extraction area with a size of $10.8' \times 10.8'$. This area is larger than the PSF of both experiments.

For the application of the RLA an adjusted On-model is necessary because of this non-uniform morphology of RX J1713.7−3946. The new model, presented in Fig. 5.12, describes the shape of the data very well. An value of 3 was derived for N_{opt} which leads again to an improvement of the angular resolution of about 20%.

In Fig. 5.11 the correlation coefficient between the ASCA and the H.E.S.S. data is plotted for different bin sizes. Without deconvolution the correlation coefficient rises with increasing bin size but it is lower than the value found for the simulation. For the simulations exactly the same morphology for the two ACEMs is used. In case of real data the morphology of the X-ray and VHE γ-ray data is not assumed to be identical due to e.g. energy dependent diffusion processes, cross-sections.

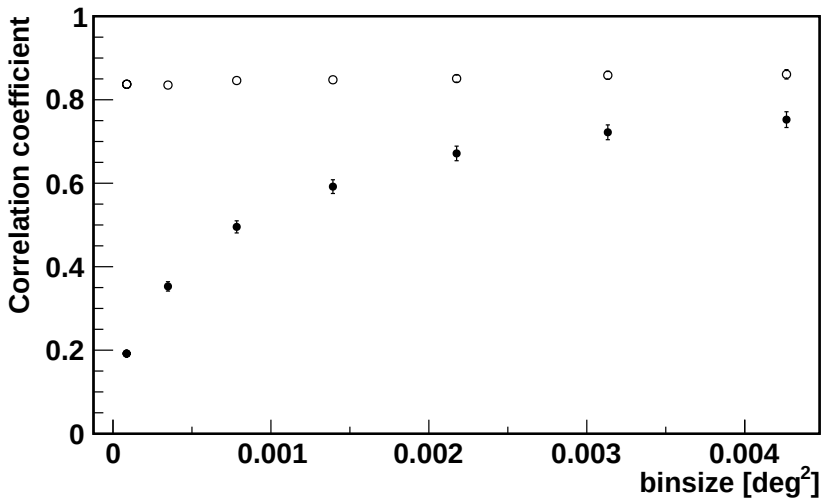

Figure 5.11: Correlation between ASCA and H.E.S.S. data as a function of bin size. The region for the calculation of the coefficient before and after the deconvolution of the H.E.S.S. data is a priori chosen to contain the whole source and to depend mainly on the signal and to avoid regions with only background. In particular for smaller bin sizes, an increase of the correlation coefficient for the deconvolved map (open circles) as compared to the original map (filled circles) is found.

The good agreement of the morphology of the X-ray and VHE γ-ray data is also shown in Fig. 5.13. Here the ACEM of RX J1713.7−3946 is overlaid with black contours of the ASCA data without and with deconvolution.

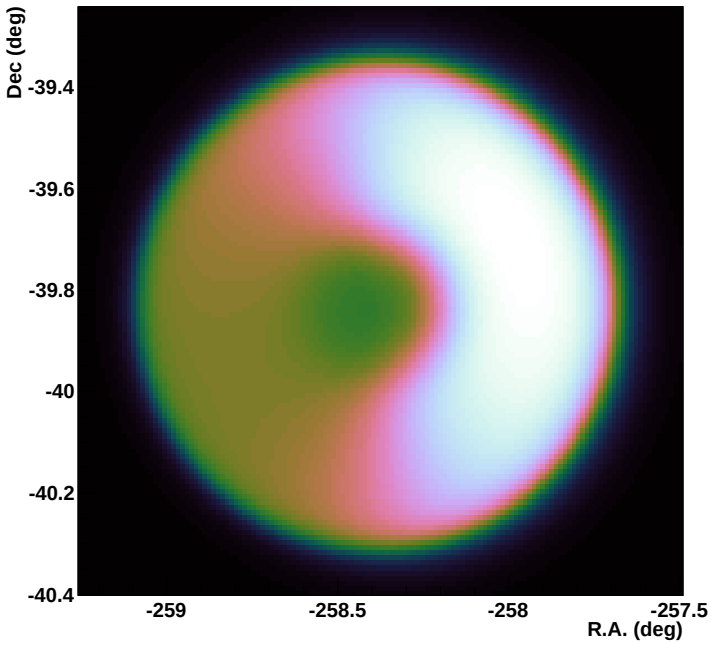

Figure 5.12: On-model of RX J1713.7−3946 used for simulations.

5.5.3 Application to the VHE γ-ray Data of RCW 86

At the end of the previous chapter the correlation between the XMM-Newton data and the H.E.S.S. data of RCW 86 was calculated. The correlation was low and dependent on the chosen bin size. Now the correlation study between the X-rays and the H.E.S.S. data is performed in detail by the use of deconvolution.
In a first step the best possible theoretical correlation between X-rays and VHE γ-ray data is studied. Therefore it is assumed, that the X-ray and the VHE γ-ray data have the same morphology, i.e the X-ray sky map is taken as On-model for the γ-ray data. The VHE γ-ray sky map is simulated with the same statistic (signal-to-noise ratio, significance, background events) as the VHE γ-ray analysis presented in this thesis. Afterward the simulated VHE γ-ray sky map is deconvolved and the spatial correlation with the X-ray sky map is determined. The optimal number of iterations is found to be 2, i.e. no improvement of the angular resolution is present. The deconvolution only smooths the map. Nevertheless the correlation coefficient is given in 5.14. Similar to the case of RX J1713.7−3946 the correlation is nearly independent of the bin size but the possible achievable correlation is lower ($\sim$0.7). The higher value compared to the image without deconvolution can be explained by the fact, that the image is smoothed and background fluctuations are reduced. The lower absolute correlation coefficient is due to the fact, that the angular resolution is not improved.

Finally the H.E.S.S. data of RCW 86 is also deconvolved and the correlation is calculated. The obtained correlation is shown in Fig. 5.15. Compared to the simulated values, the overall correlation is lower. A possible explanation for this is that the VHE γ-ray emission is not produced by exactly the same population as the X-rays. One has to stress, that the deconvolution is not improving the angular resolution, therefore for correlation studies down to finer structures than defined by the H.E.S.S. PSF more data has to be taken.

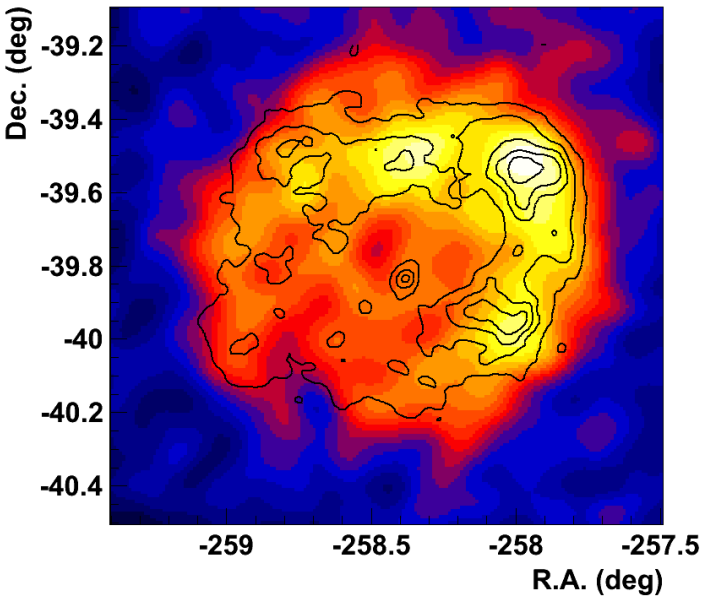

(a) without deconvolution

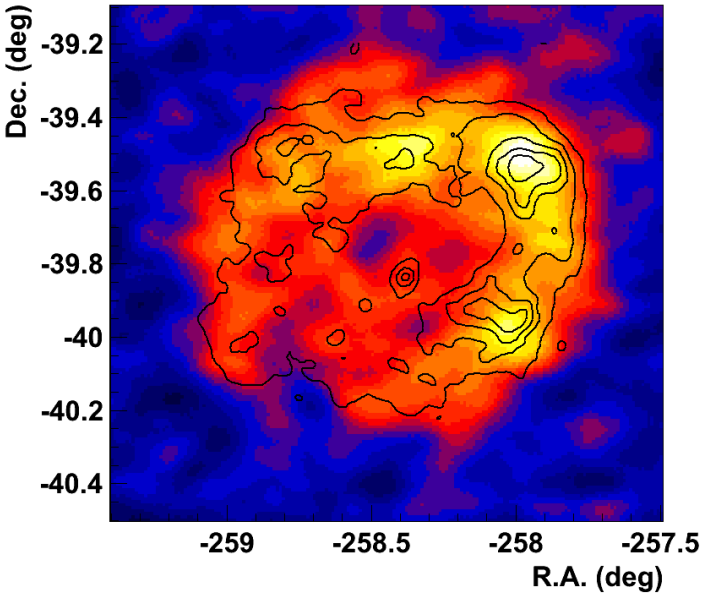

(b) with deconvolution

Figure 5.13: Acceptance-corrected excess map of RX J1713.7−3946 without (a) and with deconvolution (b) overlaid with black contours of the ASCA data. The map without deconvolution is smoothed with a Gaussian function with a width $\sigma = 0.03$.

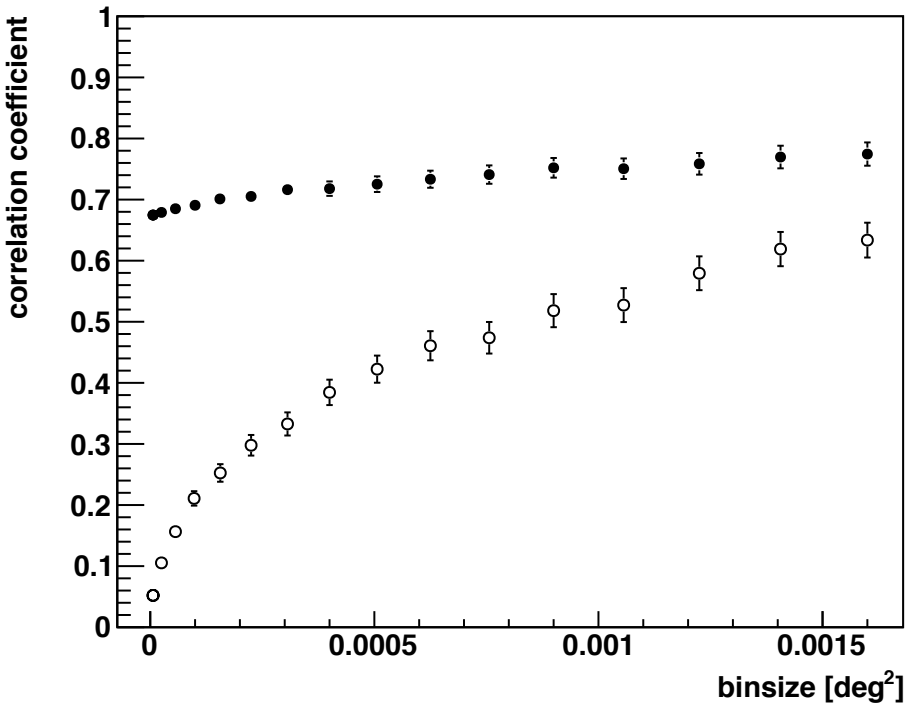

Figure 5.14: Correlation of XMM-Newton and simulated H.E.S.S. data as a function of bin size. The region for the calculation of the coefficient before and after the deconvolution of the H.E.S.S. data is a priori chosen to contain the whole source and to depend mainly on the signal and to avoid regions with only background. In particular for smaller bin sizes, an increase of the correlation coefficient for the deconvolved map (filled circles) as compared to the original map (open circles) is found.

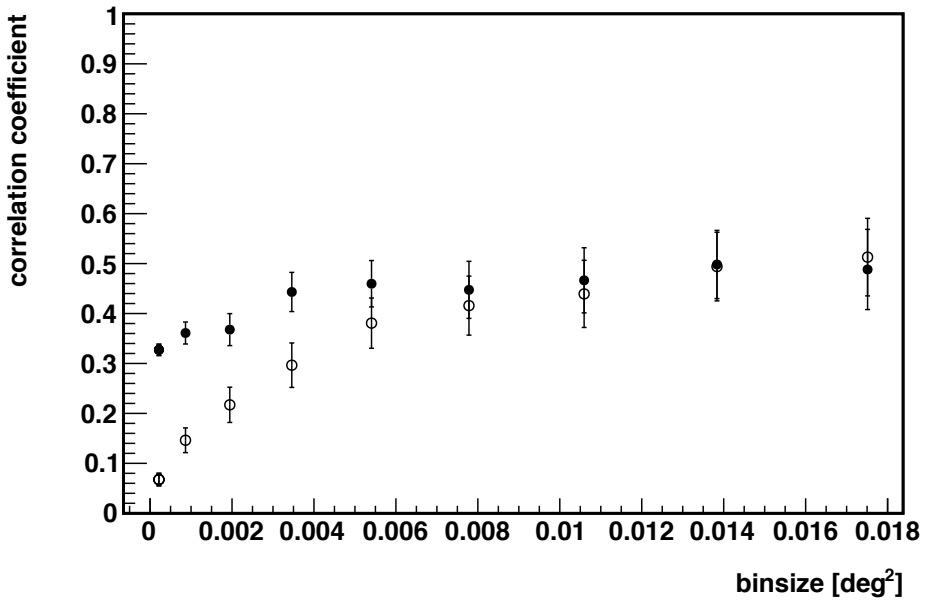

Figure 5.15: Correlation of XMM-Newton and H.E.S.S. data as a function of bin size. The region for the calculation of the coefficient before and after the deconvolution of the H.E.S.S. data is a priori chosen to contain the whole source and to depend mainly on the signal and to avoid regions with only background. In particular for smaller bin sizes, a slightly increase of the correlation coefficient for the deconvolved map (filled circles) as compared to the original map (open circles) is found

5.6 Potential of the Application to shell-like H.E.S.S. Sources

RX J1713.7−3946 is the strongest VHE SNR with a shell-like morphology among a number of extended VHE γ-ray sources detected by H.E.S.S.. All other detected sources have a smaller significance and signal-to-noise ratio. Because of this the performance of the RLA is lower on these sources. Notwithstanding it is interesting how the different sources act under the application of deconvolution. In Table 5.1 the results of extended SNRs are summarized. The following parameters are listed: the source size, the required significance to obtain an optimal number of iterations of at least three and the already observed significance. The significance of SN 1006, RCW 86 and Vela Junior is not high enough to apply the RLA. For HESS J1731−347 it is possible to apply the RLA but unfortunately the source is covered only partial in X-rays and therefore a similar correlation study can not be performed like for RX J1713.7−3946 and RCW 86.

Table 5.1: Given are the source sizes, the already detected significance of the extended SNRs detected by the H.E.S.S. experiment as well as the required significance to obtain at least an optimal iteration of three.

source	source size [°]	observed significance [σ]	required significance [σ]	reference
HESS J1731 − 347	0.33	22	20	H.E.S.S. Collaboration et al. (2011)
SN 1006	0.35	4.9	20	H.E.S.S. Collaboration et al. (2010)
RCW 86	0.41	14.9	30	Aharonian et al. (2009)
RX J1713.7 − 3946	0.65	39	39	Aharonian et al. (2006b)
Vela Junior	1.00	19	68	Aharonian et al. (2007)

6 Summary and Conclusions

The focus of this thesis is the detailed study of the supernova remnant RCW 86. In the introduction the connection between the cosmic rays and the VHE γ-rays is presented and it is studied which role the VHE γ-ray astronomy can play to solve the still open question whether supernova remnants are the main accelerators of cosmic rays or not.
This leads directly to Chapter 2 which starts with the evolution and morphology of SNRs and their acceleration of particles. In the following a list of all supernova remnants, detected with H.E.S.S. so far, is presented. At the end of this chapter the characteristics of RCW 86 in different wavebands (radio, optical, X-rays, VHE γ-ray) are presented to outline the current knowledge of this particular VHE γ-ray source. In 2009 the detection of RCW 86 in VHE γ-rays was published. At that time it was not clear whether the source belongs to the class of supernova remnants with a shell-like morphology or not. The analysis with improved methods allows to finally settle this issue in this thesis.
Chapter 3 is focused the Imaging Atmospheric Cherenkov Technique and the H.E.S.S experiment. It starts with a brief introduction of the physics of air showers which are the detectable traces of VHE γ-rays and the Imaging Atmospheric Cherenkov Technique. In the following the H.E.S.S. experiment is presented. After the experimental setup the different steps of the data analysis are described for the Hillas moment and the more sensitive Model++ analysis. This knowledge is used in Chapter 4 and Chapter 5.
In Chapter 4, the analysis of the new VHE γ-ray data set of RCW 86 is presented. In the spectral analysis a pure power-law fit is disfavored compared to more complex spectral shapes like exponential cut off, curved and broken power law. The best results are obtained with the exponential cut-off power law. It is characterized by an index of 1.50 ± 0.28, a cut off energy of $E_C = (2.69\pm0.99)$ TeV and an integral flux of $(6.51 \pm 2.69)\cdot10^{-12}\mathrm{cm}^{-2}\mathrm{s}^{-1}$. In X-rays the observations show different spectral indices in different parts of RCW 86. Therefore the South-West part has been analyzed separately. The differences seen in the X-rays can not be confirmed in the VHE γ-ray regime.
With the study of the morphology of the new H.E.S.S. data set and a strict data selection it is possible to pin down for the first time the shell-like structure of RCW 86. The performed systematic checks confirm the derived result. The chapter ends with the morphological comparison of the X-ray and VHE γ-ray data of RCW 86. On one side the large-scale structures are similar but on the other side the fine structures differ which can be seen in the radial and azimuthal distributions. The low correlation coefficient of 0.48 between the smoothed X-ray and VHE γ-ray data can be interpreted that the X-ray and VHE γ-ray emission are produced in different regions of the SNR. For a more detailed study of the morphology an improved angular resolution is mandatory. Which leads to the next chapter with the main focus on deconvolution studies.
The deconvolution technique is widely used in astronomy for improvements in the study of the morphology of extended sources. The Richardson-Lucy algorithm (RLA) is especially suited for this purpose. Up to now, the deconvolution technique was not applied in the VHE γ-ray astronomy since the rather low signal-to-noise ratio typical in this field makes deconvolution rather complicated. Therefore a systematic study of the RLA is presented in Chapter 5. At first the deconvolution technique is introduced. This is followed by a systematic study of the algorithm concerning the improvement with respect to the angular resolution of the H.E.S.S. analysis. In the following the

gained knowledge is used for the deconvolution of simulated VHE γ-ray data and the data of the brightest supernova remnant, RX J1713.7 − 3946, and RCW 86. Because of the low signal-to-noise ratio of RCW 86 it is arguable if the deconvolution is applicable. The main result of this Chapter is that the deconvolution technique is applicable to strong VHE γ-ray sources with a good signal-to-noise ratio and that the correlation between X-rays and the VHE γ-ray data becomes independent of the bin size of the used sky maps for these sources. Therefore the comparison of the data of different wavebands can be performed on smaller scales by the use of deconvolution.

In summary, the main result of this thesis is the confirmation of the shell-like structure of RCW 86 for the first time in the VHE γ-ray astronomy. Hopefully the still remaining questions on RCW 86 could be solved in the future by new data and experiments. The deconvolution technique for morphological studies has been introduced into the VHE γ-ray astronomy and first results have already been shown. Because of its good performance it is a further improvement in the analysis of the morphologies. Since the upcoming VHE γ-ray experiment CTA will have a better signal to noise ratio the deconvolution technique should be definitely implemented as a standard procedure for the analysis of morphologies.

7 Zusammenfassung und Ausblick

Das Hauptaugenmerk dieser Dissertation ist auf die detaillierte Studie des Supernovaüberrest RCW 86 gerichtet. In der Einleitung wird die Verbindung zwischen der kosmischen Strahlung und der Gammastrahlung beschrieben und es ist untersucht worden welche Rolle die Gammastrahlungsastronomie bei der Lösung der immer noch offen Frage spielt, ob die Supernovaüberreste die hauptsächlichen Teilchenbeschleuniger für die kosmische Strahlung sind.
Dies führt direkt zu Kapitel 2, welches mit der Entwicklung und Morphologie von Supernovaüberresten und ihrer Beschleunigung von Teilchen beginnt. Im weiteren Verlauf wird eine Liste von allen Supernovaüberresten aufgeführt, die von H.E.S.S. bis jetzt detektiert wurden. Am Ende des Kapitels werden die Eigenschaften von RCW 86 in verschieden Wellenlängenbereichen (Radio, Optisch, Röntgen und Gammastrahlung) dargelegt um das momentane Wissen über diese spezielle Gammastrahlungsquelle zusammenzufassen. In 2009 wurde die Detektion von RCW 86 veröffentlicht. Zu dieser Zeit war es noch nicht klar, ob die Quelle zu der Gruppe der schalen-artigen Supernovaüberresten gehört oder nicht. Die Analyse mit verbesserten Methoden erlaubt es, diese Angelegenheit abschließend in dieser Dissertation zu klären.
Kapitel 3 beschäftigt sich mit der abbildenden atmosphärischen Cherenkov Technik und dem H.E.S.S. Experiment. Es beginnt mit einer kurzen Einführung in die Physik der Luftschauer, die die detektierbaren Spuren der Gammastrahlung sind, und der abbildenden atmosphärischen Cherenkov Technik. Im weiteren Verlauf wird das H.E.S.S. Experiment erläutert. Nach dem experimentellen Aufbau werden die verschiedenen Schritte der Datenanalyse für die Hillas Moment und die sensitivere Model++ Analyse beschrieben. Diese Kenntnis wird in Kapitel 4 und Kapitel 5 verwendet.
In Kapitel 4 wird die Analyse des neuen Gammastrahlungsdatensatzes von RCW 86 dargelegt. In der Spektrumsanalyse wird ein Fit mit einem reinen Potenzgesetz im Vergleich zu komplizierteren spektralen Formen wie Potenzgesetz mit exponentieller Abschwächung, ein gekrümmtes Potenzgesetz oder ein gebrochenes Potenzgesetz abgelehnt. Die besten Ergebnisse werden mit einem Potenzgesetz mit exponentieller Abschwächung erzielt. Es ist durch einen Index von 1.50 ± 0.28, eine Abknickenergie von $E_C = (2.69 \pm 0.99)\,\mathrm{TeV}$ und einem integrierten Fluss von $(6.51 \pm 2.69) \cdot 10^{-12}\,\mathrm{cm}^{-2}\mathrm{s}^{-1}$ bestimmt. Im Bereich der Röntgenstrahlung zeigen die Beobachtungen verschiedene spektrale Indizes in unterschiedlichen Regionen von RCW 86. Daher wurde eine separate spektrale Analyse des süd-westlichen Teils durchgeführt. Die Unterschiede, die im Röntgenbereich gesehen werden, können im Bereich der Gammastrahlung nicht bestätigt werden.
Mit der Untersuchung der Morphologie der neuen H.E.S.S. Daten und einer strikten Datenauswahl ist es erstmalig möglich die Schalenstruktur von RCW 86 fest zuhalten. Die durchgeführten systematischen Kontrollen erhärten das hergeleitete Ergebnisse nochmals. Das Kapitel endet mit dem morphologischen Vergleich der Röntgen- und Gammastrahlungsdaten. Auf der einen Seite sind die großskaligen Strukturen ähnlich, auf der anderen Seite weichen die feineren Strukturen von einander ab, was am radialen und azimuthalen Profil ersichtlich wird. Der geringe Korrelationskoeffizient von 0.48 zwischen den Röntgen- und Gammastrahlungsemission kann so interpretiert werden, dass die Röntgen- und Gammastrahlungsemission in verschiedenen Regionen des Supernovaüberrest erzeugt werden. Für eine weiterführende Studie der Morphologie wird eine verbesserte Winkelauflösung benötigt. Dies führt zum nächsten Kapitel mit dem Hauptaugenmerk

auf die Entfaltungstechnik.
Die Entfaltungtechnik ist in der Astronomie für die Verbesserung in der Untersuchung der Morphologie von ausgedehnten Quellen weit verbreitet. Der Richardson-Lucy Algorithmus (RLA) ist besonders für diese Aufgabe geeignet. Bis jetzt wurde die Entfaltungstechnik jedoch noch nicht in der Gammastrahlungsastronomie angewendet, da wegen dem ziemlich geringen Signal zu Rausch Verhältnis, was typisch in diesem Bereich ist, die Entfaltungstechnik sich als schwierig erweist. Daher wurde eine systematische Untersuchung des RLA in Kapitel 5 dargelegt. Zunächst wird die Entfaltungstechnik eingeführt und anschließend wird die systematische Studie des Algorithmus im Bezug auf die Verbesserung hinsichtlich der Winkelauflösung der H.E.S.S. Analyse gezeigt. Im weiteren Verlauf wird das erworbene Wissen bei der Entfaltung von simulierten Gammastrahlungsdaten, den Daten des hellsten Supernovaüberrests RX J1713.7 − 3946 und RCW 86 angewendet. Wegen dem geringen Signal zu Rausch Verhältnis von RCW 86 ist es diskutierbar, ob die Entfaltungstechnik angewandt werden kann. Das Hauptresultat dieses Kapitel ist, dass die Entfaltungstechnik bei starken Gammastrahlungsquellen angewendet werden kann und die Korrelation zwischen Röntgen- und Gammastrahlungsdaten unabhängig von der Bingröße der verwendeten Himmelskarten dieser Quellen wird. Daher ist es möglich die Daten zwischen unterschiedlichen Wellenlängenbereichen auf kleineren Skalen durch die Anwendung von Entfaltung zu vergleichen.

Zusammenfassend zeigt sich, dass das Hauptergebnis dieser Arbeit die erstmalige Bestätigung der schalen-artigen Struktur von RCW 86 in der Gammastrahlungsastronomie ist. Hoffentlich können die immer noch offenen Fragen bezüglich RCW 86 in der Zukunft durch neue Daten und Experimente gelöst werden. Die Entfaltungstechnik für Untersuchungen der Morphologie wurden in die Gammastrahlungsastronomie eingeführt und es wurden bereits erste Ergebnisse gezeigt. Wegen ihrer guten Leistung ist es eine weitere Verbesserung in der Untersuchung von Morphologien. Da das zukünftige Experiment CTA ein besseres Signal zu Rausch Verhältnis haben wird, sollte man spätestens dann die Entfaltungstechnik als Standardmethode für die Untersuchung von Morphologien einsetzen.

List of Figures

List of Tables

Bibliography

Aharonian, F., Akhperjanian, A., Aye, K.-M., et al. 2004, Astroparticle Physics, 22, 109

Aharonian, F., Akhperjanian, A. G., Barres de Almeida, U., et al. 2008a, A&A, 483, 509

Aharonian, F., Akhperjanian, A. G., Barres de Almeida, U., et al. 2008b, A&A, 490, 685

Aharonian, F., Akhperjanian, A. G., Barres de Almeida, U., et al. 2008c, A&A, 486, 829

Aharonian, F., Akhperjanian, A. G., Bazer-Bachi, A. R., et al. 2008d, A&A, 481, 401

Aharonian, F., Akhperjanian, A. G., Bazer-Bachi, A. R., et al. 2006a, A&A, 457, 899

Aharonian, F., Akhperjanian, A. G., Bazer-Bachi, A. R., et al. 2006b, A&A, 449, 223

Aharonian, F., Akhperjanian, A. G., Bazer-Bachi, A. R., et al. 2007, The Astrophysical Journal, 661, 236

Aharonian, F., Akhperjanian, A. G., de Almeida, U. B., et al. 2009, ApJ, 692, 1500

Aharonian, F. A., Hofmann, W., Konopelko, A. K., & Völk, H. J. 1997, Astroparticle Physics, 6, 369

Bamba, A., Koyama, K., & Tomida, H. 2000, PASJ, 52, 1157

Bell, A. R. 1978, MNRAS, 182, 147

Benbow, W. for the H.E.S.S. Collaboration. 2005, in Proc. Conf. Towards a Network of Atmospheric Cherenkov Detectors VII, Palaiseau (Ecole Polytechnique), 163–171

Berge, D., Funk, S., & Hinton, J. 2007, Astronomy and Astrophysics, 466, 1219

Bernlöhr, K. 2010, Picture and movie from simulated air showers

Bernlöhr, K. et al. 2003, Astroparticle Physics, 20, 111

Bhattacharya, D. 1990, Astronomy and Astrophysics, 11, 125

Blumenthal, G. R. & Gould, R. J. 1970, Rev. Mod. Phys., 42, 237

Bocchino, F., Vink, J., Favata, F., Maggio, A., & Sciortino, S. 2000, A&A, 360, 671

Borkowski, K. J., Rho, J., Reynolds, S. P., & Dyer, K. K. 2001, ApJ, 550, 334

Brun, F., de Naurois, M., Hofmann, W., et al. 2011, ArXiv e-prints

Caswell, J. L., Clark, D. H., Crawford, D. F., & Green, A. J. 1975, Australian Journal of Physics Astrophysical Supplement, 37, 1

Chernoff, H. 1954, The Annals of Mathematical Statistics, 25, pp. 573

de Naurois, M. & Rolland, L. 2009, Astroparticle Physics, 32, 231

de Naurois, M. 2011, Internal documentation

Dermer, C. D. 1986, A&A, 157, 223

Dickel, J. R., Strom, R. G., & Milne, D. K. 2001, The Astrophysical Journal, 546, 447

Fermi, E. 1949, Phys. Rev., 75, 1169

Fermilab. 2011, Particles Matter – Physics at High-Energy

Frigo, M. & Johnson, S. G. 2005, Proceedings of the IEEE, 93, 216, special issue on "Program Generation, Optimization, and Platform Adaptation"

Funk, S. et al. 2004, Astroparticle Physics, 22, 285

Green, D. A. 2002, Highlights of Astronomy, 12, 350

Greisen, K. 1966, Phys. Rev. Lett., 16, 748

Heinz, S., Jung, I., & Stegmann, C. 2012, accepted in Astroparticle Physics

Heitler, W. 1954, Quantum Theory of Radiation (Oxford University Press)

Helder, E. A., Vink, J., Bassa, C. G., et al. 2009, Science, 325, 719

Hess, V. 1912, Über die Beobachtungen der durchdringenden Strahlung bei sieben Freiballonfahrten

H.E.S.S. Collaboration, Abramowski, A., Acero, F., et al. 2011, A&A, 531, A81+

H.E.S.S. Collaboration, Abramowski, A., Acero, F., et al. 2012, in prep.

H.E.S.S. Collaboration, Acero, F., Aharonian, F., et al. 2010, A&A, 516, A62+

Hill, E. R. 1967, Australian Journal of Physics, 20, 297

Hillas, A. M. 1985, in International Cosmic Ray Conference, Vol. 3, International Cosmic Ray Conference, ed. F. C. Jones, 445–448

Hinton, J. A. 2004, New Astronomy Review, 48, 331

Hinton, J. A. & Hofmann, W. 2009, ARA&A, 47, 523

Hofmann, W., Jung, I., Konopelko, A., et al. 1999, Astroparticle Physics, 12, 135

Hofverberg, P., Chaves, R. C. G., Fiasson, A., et al. 2011, ArXiv e-prints

Jung, I. 2003, PhD thesis, Ruprecht Karls Universität, Heidelberg, Germany

Komin, N. 2006, PhD thesis, Humboldt Universität zu Berlin, Germany

Konopelko, A. K. & Plyasheshnikov, A. V. 2000, Nuclear Instruments and Methods in Physics Research Section A:, 450, 419

Kowalski, H. 2011, Einführung in die Astroteilchenphysik

Kraus, J. 2011, A Strange Radiation from Above

Lazendic, J. S., Dickel, J. R., Haynes, R. F., Jones, P. A., & White, G. L. 2000, ApJ, 540, 808

Lemoine-Goumard, M. for the H.E.S.S. Collaboration. 2005, in Proc. Conf. Towards a Network of Atmospheric Cherenkov Detectors VII, Palaiseau, 173–181

Li, T.-P. & Ma, Y.-Q. 1983, The Astrophysical Journal, 272, 317

Longair, M. S. 2011, Particles, photons and their detection, Vol. 1, High Energy Astrophysics (Cambridge University Press)

Lucy, L. B. 1974, Astronomical Journal, 79, 745

Mattox, J. R., Bertsch, D. L., Chiang, J., et al. 1996, ApJ, 461, 396

Mills, B. Y., Slee, O. B., & Hill, E. R. 1961, Australian Journal of Physics, 14, 497

Mori, M. 1997, The Astrophysical Journal, 478, 225

Nakamura, K., e. a. 2010, (Particle Data Group)

Naranan, S., Shulman, S., Yentis, D., Fritz, G., & Friedman, H. 1977, ApJ, 213, L53

Ohm, S., van Eldik, C., & Egberts, K. 2009, Astroparticle Physics, 31, 383

Padmanabhan, T. 2001, Theoretical Astrophysics, Volume II: Stars and Stellar Systems (Cambridge University Press)

Pisarski, R. L., Helfand, D. J., & Kahn, S. M. 1984, ApJ, 277, 710

Ptuskin, V. S., Rogovaya, S. I., Zirakashvili, V. N., et al. 1993, A&A, 268, 726

Rademakers, F. & Brun, R. 2011, ROOT: an object-oriented data analysis framework, http://root.cern.ch/

Richardson, W. H. 1972, Journal of the Optical Society of America (1917-1983), 62, 55

Rosado, M., Ambrocio-Cruz, P., Le Coarer, E., & Marcelin, M. 1996, A&A, 315, 243

Sakhibov, F. K. & Smirnov, M. A. 1982, Soviet Astronomy Letters, 8, 150

Sedov, L. I. 1959, Similarity and Dimensional Methods in Mechanics, ed. Sedov, L. I.

Smith, R. C. 1997, AJ, 114, 2664

Sollerman, J., Ghavamian, P., Lundqvist, P., & Smith, R. C. 2003, A&A, 407, 249

Tanaka, T., Uchiyama, Y., Aharonian, F. A., et al. 2008, The Astrophysical Journal, 685, 988

The Fermi-LAT Collaboration. 2011, ArXiv e-prints

Vink, J., Bleeker, J., van der Heyden, K., et al. 2006, ApJ, 648, L33

Vink, J., Kaastra, J. S., & Bleeker, J. A. M. 1997, A&A, 328, 628

Weekes, T. C., Cawley, M. F., Fegan, D. J., et al. 1989, ApJ, 342, 379

Wilks, S. S. 1938, The Annals of Mathematical Statistics, 9, pp. 60

Williams, B. J., Blair, W. P., Blondin, J. M., et al. 2011, The Astrophysical Journal, 741, 96

Woltjer, L. 1972, ARA&A, 10, 129

Zatsepin, G. T. & Kuz'min, V. A. 1966, Soviet Journal of Experimental and Theoretical Physics Letters, 4, 78

Acknowledgement/Danksagung

An dieser Stelle möchte ich mich bei allen ganz herzlich bedanken, die mir bei der Erstellung und dem Gelingen meiner Dissertation geholfen haben.

Das ECAP stellte das ideale Umfeld für meine Arbeit auf dem Gebiet der Hochenergie Astrophysik dar, durch die sehr gute Arbeitatmosphäre und -bedingungen sowie die Möglichkeit Kontakte mit anderen Doktoranden und Professoren zu pflegen, die auf einem angrenzenden Gebiet arbeiten.

Doktorvater, Prof. Dr. Christian Stegmann. Ohne Ihn wäre meine Disseration in dieser Form nicht möglich gewesen. Durch seine motivierende Art und die gute Betreuung, musste ich nach meiner Diplomarbeit nicht lange überlegt, ob ich auch meine Doktorarbeit bei Ihm anfertigen möchte. Daher hatte ich auch das große Glück die Erlanger H.E.S.S. Gruppe fast von Anfang an mitzuerleben und mitgestalten zu können. Prof. Dr. Christian Stegmann versteht es ausgezeichnet einen zu fordern und zu fördern, sei es durch kritisches Hinterfragen oder durch sehr gute Ratschläge und anregende Diskussionen. Trotzdem ließ er einem immer genügend Freiraum für eigene Ideen und dessen Umsetzung bei meiner wissenschaftliche Arbeit.

Nun möchte ich mich bei Ira Jung bedanken, für ihre ständige Bereitschaft über Ideen zu diskutieren und meine Arbeit Korrektur zu lesen.

Mit Kathrin Valerius als Zimmerkollegin habe ich ein sehr angenehmes Zimmer bezogen. Ich danke Ihr für das Korrektur lesen meiner Arbeit, wobei sie auch noch jeden kleinsten Rechtschreibfehler gefunden hat.

Als nächstes möchte ich mich bei der Erlanger H.E.S.S. Gruppe und der neuen Desy Zeuthen H.E.S.S. Gruppe bedanken. Auch wenn ein Teil von uns nach Zeuthen gegangen ist, schaffen wir es trotzdem den Kontakt zu halten und gemeinsam zu forschen. Ich möchte mich für die schöne Zeit bei allen bedanken: Zunächst bei den beiden Ehemaligen Bernhard und Fabian, dann bei den noch nicht genannten Mitglieder der aktuellen Erlanger Gruppe, Anton, Constanze, Daniel, Julia, Peter, Philipp, Susanne, Stephanie, Luisa und Fidi. Den Mitglieder der Desy Zeuthen Gruppe gilt genauso mein Dank: Anneli, Arnim, Christian, Kora, Markus und Michi.

Neben all den Personen an der Universität danke ich besonders meiner Frau. Auch wenn die Zeit der Promotion nicht immer einfach gewesen ist, hat sie mich unterstützt und dadurch wesentlich zum Gelingen dieser Arbeit beigetragen.